

PROCESSING OXIDE THIN FILMS WITH LIGHT:
A PATH TO HIGH-THROUGHPUT SOLUTION-PROCESSED
OXIDE ELECTRONICS

by

Trey Benjamin Daunis



APPROVED BY SUPERVISORY COMMITTEE:

Julia W. P. Hsu, Chair

Manuel A. Quevedo-Lopez

William G. Vandenberghe

Walter E. Voit

Chadwin D. Young

Copyright 2019

Trey Benjamin Daunis

All Rights Reserved

To my family

PROCESSING OXIDE THIN FILMS WITH LIGHT:
A PATH TO HIGH-THROUGHPUT SOLUTION-PROCESSED
OXIDE ELECTRONICS

by

TREY BENJAMIN DAUNIS, BS, MS

DISSERTATION

Presented to the Faculty of
The University of Texas at Dallas
in Partial Fulfillment
of the Requirements
for the Degree of

DOCTOR OF PHILOSOPHY IN
MATERIALS SCIENCE AND ENGINEERING

THE UNIVERSITY OF TEXAS AT DALLAS

December 2019

ACKNOWLEDGMENTS

I would like to extend my gratitude to Prof. Julia W. P. Hsu for her support and guidance during my PhD education. I appreciate her help with this doctoral dissertation as well as with my overall academic and professional development. I am also happy to extend many thanks to each member of my supervising committee – Prof. Manuel A. Quevedo-Lopez, Prof. William G.

Vandenberghe, Prof. Walter E. Voit, and Prof. Chadwin D. Young.

I would like to thank each of my lab partners, past and present, for all their contributions during my time as a graduate student – Dr. Yun-Ju (Alex) Lee, Dr. Jian Wang, Dr. Liang Xu, Dr. Diego Barrera, Dr. Sampreetha Thampy, Michael Womble, Lakshmi Murthy, Boya Zhang, Weijie Xu, and Robert Piper.

Finally, I would like to thank my family – my parents who have supported and encouraged me throughout my life and education, and my wife, Ana, who has given me the endless support and inspiration that I needed to complete my PhD.

I would also like to acknowledge the sources of funding for my research. This work is funded in part by the U.S. Department of Energy Solar Energy Technologies Office, under Award Number DE-EE0008544, and is partially supported by the National Science Foundation (NSF DMR-1305893) and by the Center for Engineering Innovation and by SPARC.

October 2019

PROCESSING OXIDE THIN FILMS WITH LIGHT:
A PATH TO HIGH-THROUGHPUT SOLUTION-PROCESSED
OXIDE ELECTRONICS

Trey Benjamin Daunis, PhD
The University of Texas at Dallas, 2019

Supervising Professor: Julia W. P. Hsu

High-throughput roll-to-roll manufacturing of solution-deposited metal oxide electronics has the potential to enable the widespread and low-cost availability of thin film electronic devices including solar panels, large-area displays and lighting, and flexible medical devices and sensors. However, several challenges have prevented the realization of this potential: (1) The processing speed of solution-deposited oxides is severely limited by the length of the annealing process, usually greater than 20 minutes, which is typically necessary to convert solution-deposited precursor films into metal oxides, (2) the quality of the resultant metal oxide films is limited by the low upper operating temperatures of low-cost, roll-to-roll compatible, plastic substrates, typically much less than 250 °C, and (3) equilibrium heating of devices to these temperatures often results in mechanical failure of the thin films due to the different thermal responses of the films and substrates.

In this dissertation, we address these challenges by using light, rather than heat, as a source of energy for curing solution-deposited metal oxide thin films. We use this method to develop

solution-deposited oxide thin film transistors (TFTs) on shape memory polymer (SMP) substrates. We demonstrate the direct patterning of Al_2O_3 and In_2O_3 precursor films on SMP by exposure to UV light through a shadow mask as a method to overcome the mechanical failure of blanket-coverage films during thermal annealing. The patterned precursors are then converted to oxides for the gate dielectric and the channel semiconductor of the TFTs by thermal annealing without causing damage to the films. The unexpectedly high mobility displayed by these TFTs is studied and the absorption of water from the atmosphere by the gate dielectric is identified as the cause.

Finally, we demonstrate the high-speed photonic curing of ZrO_2 dielectric films on polyethylene naphthalate substrates. Using intense pulsed light to both heat and cure the oxide film in as little as 100 milliseconds without significantly heating the substrate, we achieve a process for fabricating metal oxide electronic devices that is compatible with roll-to-roll processing speeds exceeding 30 m/min.

TABLE OF CONTENTS

ACKNOWLEDGMENTS	v
ABSTRACT	vi
LIST OF FIGURES	xi
LIST OF TABLES	xvi
LIST OF ABBREVIATIONS AND SYMBOLS	xvii
CHAPTER 1 INTRODUCTION	1
1.1 Materials and Processing for Solution-Deposited Thin Film Electronics	2
1.1.1 Sol-Gel Process	3
1.1.2 Lowering the Sol-Gel Processing Temperature	4
1.1.3 Photonic Curing.....	5
1.2 Flexible Substrates	6
1.3 Thin Film Electronic Devices	8
1.3.1 Thin Film Transistors	8
1.3.2 Metal – Insulator – Metal Capacitors.....	9
1.4 Outline of Dissertation.....	9
1.5 References.....	10
CHAPTER 2 SOLUTION-DEPOSITED AL ₂ O ₃ DIELECTRIC TOWARDS FULLY- PATTERNED THIN FILM TRANSISTORS ON SHAPE MEMORY POLYMER.....	13
2.1 Preface.....	14
2.2 Abstract.....	15
2.3 Introduction.....	15
2.4 Experimental Details.....	18
2.4.1 Device Structure.....	18
2.4.2 Metal Oxide Precursor Solutions	18
2.4.3 Metal Oxide Film Deposition.....	19
2.4.4 Film and Device Characterization.....	20
2.5 Results and Discussion	21

2.6	Conclusions.....	27
2.7	References.....	28
CHAPTER 3 SOLUTION-PROCESSED OXIDE THIN FILM TRANSISTORS ON SHAPE MEMORY POLYMER ENABLED BY PHOTOCHEMICAL SELF-PATTERNING		
3.1	Preface.....	31
3.2	Abstract.....	31
3.3	Introduction.....	32
3.4	Experimental Details.....	35
	3.4.1 SMP Substrate Fabrication and Characterization.....	35
	3.4.2 TFT Fabrication.....	36
	3.4.3 Materials and Device Characterization	38
3.5	Results and Discussion	39
	3.5.1 Chemical Studies of Photochemical Processing	39
	3.5.2 Device Characteristics.....	44
3.6	Conclusions.....	48
3.7	Acknowledgments.....	48
3.8	References.....	49
CHAPTER 4 EFFECTS OF ENVIRONMENTAL WATER ABSORPTION BY SOLUTION-DEPOSITED AL ₂ O ₃ GATE DIELECTRICS ON THIN FILM TRANSISTOR PERFORMANCE AND MOBILITY.....		
4.1	Preface.....	54
4.2	Abstract.....	54
4.3	Introduction.....	55
4.4	Experimental Details.....	57
	4.4.1 Film and Device Fabrication.....	57
	4.4.2 Materials and Device Characterization	58
4.5	Results and Discussion	59
	4.5.1 Capacitance-Frequency Dispersion in the Dielectric	59
	4.5.2 Transistor Hysteresis and High Mobility	64
	4.5.3 Charge Transfer from Dielectric to Gate.....	66
	4.5.4 Effect of Materials Processing	69

4.5.5	Corrections for Channel Width and Gate Dielectric Frequency Dispersion	70
4.6	Conclusions.....	74
4.7	Acknowledgments.....	74
4.8	References.....	74
CHAPTER 5 PHOTONIC CURING OF SOLUTION-DEPOSITED ZRO ₂ DIELECTRIC ON POLYETHYLENE NAPHTHALATE: HIGH-THROUGHPUT PROCESSING OF OXIDE ELECTRONICS		78
5.1	Preface.....	79
5.2	Abstract.....	79
5.3	Introduction.....	80
5.4	Experimental Details.....	84
5.4.1	Film Deposition.....	84
5.4.2	Photonic Curing.....	84
5.4.3	SimPulse [®] Simulation	85
5.4.4	Capacitor Fabrication and Measurements	85
5.5	Results and Discussion	86
5.5.1	Photonic Curing and Patterning of ZrO ₂ Films on PEN	86
5.5.2	Dielectric Properties of PC-ZrO ₂ on PEN.....	91
5.6	Conclusions.....	96
5.6.1	Path to High-Throughput Processing of Oxide Electronics	96
5.7	Acknowledgments.....	97
5.8	References.....	98
CHAPTER 6 CONCLUSIONS AND FUTURE WORK.....		103
6.1	Conclusions.....	103
6.2	Future Work: Photonic Curing of Conducting Oxide Films.....	104
BIOGRAPHICAL SKETCH		106
CURRICULUM VITAE		

LIST OF FIGURES

<p>Figure 1.1: Temperature response of film and substrate during photonic curing. (a) Film temperature vs. time for a representative film on PET (blue), PI (red), and PEN (black) substrates from 0 to 3 ms seconds after the onset of a 0.5 ms photonic curing pulse (shaded in yellow). (b) Substrate temperatures for the devices in (a) from 0 to 200 ms after the onset of the pulse.</p>	6
<p>Figure 1.2: Basic TFT structure with a substrate, bottom gate, gate dielectric, semiconductor channel, and top source and drain contacts.</p>	9
<p>Figure 2.1: HfO₂ deposited by ALD at 150 °C. Two of the four capacitors shown (no top contacts in picture) are compromised by cracks that develop during processing.</p>	21
<p>Figure 2.2: Rigid In₂O₃ TFT performance on (a) 105- nm Al₂O₃ deposited by 7 coats of 0.2 M acac-containing solution and (b) 71- nm Al₂O₃ deposited by 2 coats of 0.4 M acac-free solution. Both samples were annealed at 250 °C.</p>	24
<p>Figure 2.3: SMP with Au gate electrode and 4 coats of 0.2 M Al₂O₃ from acac-containing solution annealed at 250 °C. Extensive cracking of the Al₂O₃ film is clear.</p>	25
<p>Figure 2.4: SMP with Ag/Al gate electrode (a) 1 coat 0.2 M Al₂O₃ from acac-free solution annealed at 150 °C and (b) 2 coats of Al₂O₃ prior to final UV-ozone exposure.</p>	27
<p>Figure 3.1: Transmission spectrum of a 50 μm SMP substrate on a glass slide. Transmission is 97% from 400 to 800 nm. Inset: Photographs of blank glass slide (top) and glass slide with SMP (bottom).</p>	36
<p>Figure 3.2: Photochemical self-patterning of oxide films from sol-gel precursors. Blanket deposition (step 1), photopatterning (steps 2 and 3), and annealing (step 4) of sol-gel precursor films. (a) Schematic of the process for forming patterned oxide films. (b) Optical images of the film after corresponding processing step in (a). Thin dashed lines are drawn to show boundaries of patterned oxide feature.</p>	38
<p>Figure 3.3: XPS and ellipsometry of In₂O₃ films during processing. (a) O1s spectra with deconvoluted metal oxide lattice (M-O-M) peaks and hydroxide (-OH) peaks for the dried In₂O₃ precursor film, In₂O₃ precursor film exposed to UVO for 10 min, and UVO-exposed In₂O₃ film then annealed at 175 and 250 °C. (b) Bar graphs showing the (M-O-M) peak contribution and (c) thickness from ellipsometry at specified processing stage.</p>	41
<p>Figure 3.4: (a) XPS O1s spectra of the dried Al₂O₃ precursor, Al₂O₃ film exposed to UVO for 40 min, and exposed Al₂O₃ film annealed at 250 °C showing deconvoluted M-O-M and -OH peaks. (b) Percentage of XPS O1s signal from M-O-M peak. (c) Ellipsometry thickness of the film at each processing stage.</p>	41

Figure 3.5: (a) Tapping mode AFM images of In₂O₃ (left) and Al₂O₃ (right) films from the transistor device annealed at 250 °C showing low surface roughness: rms roughness for In₂O₃ is 0.40 nm and for Al₂O₃ is 0.42 nm. The scale bars represent 250 nm and the full color scale represents 10 nm height variation. (b) Grazing angle XRD spectra for In₂O₃ (top) and Al₂O₃ (bottom) films annealed at 250 °C showing an amorphous film structure.42

Figure 3.6: (a) XPS map of N1s signal intensity surrounding a single 600 μm diameter UVO exposed circle on an In₂O₃ film. Scale bar is 200 μm. Top: N1s spectra for the unexposed precursor area (blue, top) and UVO exposed area (black, bottom). (b) N–O vibration region of FTIR spectra before and after UVO annealing for (top) an In₂O₃ film and (bottom) an Al₂O₃ film. The loss of absorbance from 1250 to 1550 cm⁻¹ in the differential spectrum indicates the removal of nitrates from the film. (c) UV-vis of In₂O₃ (blue) and Al₂O₃ (red) precursor solutions. Vertical bars represent the normalized output of the Hg vapor UV lamp.....43

Figure 3.7: TFT on SMP device structure and performance. (a) Schematic and optical image (false color added for emphasis) of device structure with SMP substrate, aluminum gate, Al₂O₃ gate dielectric, In₂O₃ semiconductor, and Al source and drain. (b) Transfer curve with drain current (I_D, red), gate current, (I_G, black), and I_D^{1/2} (blue) vs. gate voltage (V_G) for a TFT with In₂O₃ annealed at 250 °C and V_D = 3 V. Green dashed line shows I_D^{1/2} vs. V_G fit used for mobility extraction. (c) Output curves showing drain current (I_D) vs. drain voltage (V_D) for a device with In₂O₃ annealed at 175 °C. Inset: Photograph of transistors and capacitors on SMP delaminated from the carrier substrate.....45

Figure 3.8: Device performance for varying annealing temperatures of In₂O₃. (a) I_D vs. V_G curves for representative devices annealed from 175 to 250 °C taken at V_D = 3 V. (b) Areal capacitance vs. frequency measurements from 20 Hz to 300 MHz of Al / Al₂O₃ / Al MIMs for different In₂O₃ annealing temperatures.46

Figure 4.1: C-f response, dissipation factor, and FTIR spectra of solution-processed dielectric films before and after prolonged exposure to air. C-f: (a) Al₂O₃, and (d) ZrO₂. Dissipation factor: (b) Al₂O₃ and (e) ZrO₂. Open symbols represent results on as-made films and closed symbols represent data taken after 12 days stored in air with RH = 30% - 35%. In (d) and (e), the before and after results for ZrO₂ overlap. FTIR spectra: (c) Al₂O₃ and (f) ZrO₂. Dashed colored lines represent as-made films and solid colored lines represent films after 14 days in air, with the difference shown in black lines. Small IR signals between 2900 and 2800 cm⁻¹ are due to adventitious hydrocarbon from environmental exposure.60

Figure 4.2: Effect of re-annealing Al₂O₃ film after exposure to air. (a) Capacitance of air exposed Al₂O₃ film before (closed circles) and immediately after (open circles) re-annealing at 150 °C for 20 minutes. (b) FTIR spectra for an Al₂O₃ film as-made (dashed red line), after 2 weeks in air (solid red line), after re-annealing at 250 °C for 20 minutes (dashed black line), and after an additional 1 week in air (solid black line).61

- Figure 4.3: C-f response, dissipation factor, and FTIR spectra of solution-processed dielectric films before and after soaking in DI water. (a) C-f and (b) dissipation factor for Al₂O₃ (red circles) and ZrO₂ (blue squares) before (open symbols) and after (closed symbols) soaking in DI water overnight. The before and after results for ZrO₂ overlap. (c) FTIR difference spectra for Al₂O₃ (red) and ZrO₂ (blue) showing the change in FTIR absorbance after the DI water soak.61
- Figure 4.4: Removal of nitrates during annealing. FTIR spectra of (a) Al₂O₃ and (b) ZrO₂ dielectric films in the nitrate region from 2000 to 600 cm⁻¹ for precursor films (dashed colored lines), films annealed at 250 °C (solid colored lines), and the difference spectrum (solid black lines). XPS spectra of nitrogen N 1s region for 250 °C annealed (c) Al₂O₃ and (d) ZrO₂ films.62
- Figure 4.5: C-f response, dissipation factor, and FTIR spectra of bilayer solution-processed dielectric films before and after soaking in DI water. (a) C-f and (b) dissipation factor for Al₂O₃ on ZrO₂ (orange triangles) and ZrO₂ on Al₂O₃ (purple diamonds) before (open symbols) and after (closed symbols) soaking in DI water overnight. The before and after results for ZrO₂ on Al₂O₃ overlap. (c) FTIR difference spectra for Al₂O₃ on ZrO₂ (orange) and ZrO₂ on Al₂O₃ (purple) showing the change in FTIR absorbance after the DI water soak.63
- Figure 4.6: Location and orientation of adsorbed water on oxide films. (a) Kelvin probe work function measurement of Al₂O₃ (red circles) and ZrO₂ (blue squares) films stored in air over 12 days. Inset shows schematics of an Al₂O₃ film with a surface water layer and a surface dipole pointing away from the surface, and a ZrO₂ film with no water or surface dipole. (b) FTIR spectra of thick (44 nm, solid red line) and thin (14 nm, dashed light red line) Al₂O₃ films. Dashed black lines show background and solid black lines show height of water peak above background at 3395 cm⁻¹.64
- Figure 4.7: Transfer curves for In₂O₃ TFTs with (a) Al₂O₃, (b) ZrO₂, (c) bilayer Al₂O₃ on ZrO₂, and (d) bilayer ZrO₂ on Al₂O₃ as the gate dielectric. Solid colored lines show drain current (I_D, left axis), dashed colored lines show I_D^{1/2} (right axis), grey lines show gate current (I_G), and solid black straight lines show fits used for mobility calculation using C measured at 100 Hz. Black arrows show the direction of the gate voltage scan.65
- Figure 4.8: Time dependence of I_D due to charge transfer from dielectric to gate. (a) Band diagram showing electron transfer from defect states in Al₂O₃ to the gate contact under positive gate bias and with time. (b) I_D vs. time measurement with V_D = 3V for an In₂O₃ transistor on Al₂O₃ in the off-state (V_G = -3V, black triangles), in the on-state with no positive gate bias (V_G = 0V, black squares) and in the on-state with positive gate bias (V_G = 5V, red circles), which shows I_D^{1/2} increases linearly with log(time).67
- Figure 4.9: FTIR spectra of an In₂O₃ film as made (red), after 48 days in air (dark blue), and the difference (light blue).69

- Figure 4.10: Effect of processing conditions on Al₂O₃ dielectric films. (a) FTIR spectra of an Al₂O₃ film annealed at 500 °C as made (dashed red line) and after 2 days in air (solid red line). The difference spectrum is shown as a solid black line. (b) Transfer curve for In₂O₃ transistor with dielectric film composed of solution processed Al₂O₃ annealed at 250 °C on top of 20 nm of atomic layer deposited Al₂O₃ (250 °C). Drain current (I_D) (solid magenta line, left axis), gate current (solid grey line, left axis), sqrt(I_D) (dashed magenta line, right axis), and fit used for mobility calculation (solid black line).....70
- Figure 4.11: Corrections for channel width and gate dielectric frequency dispersion in mobility calculation. (a) Schematic of the S / D contact (grey) and semiconductor (green) pattern for a channel with width defined by S / D contacts. The channel current is depicted by thin black lines with fringe current outside of the defined channel depicted by curved black lines. (b) Schematic of the S / D contact and semiconductor pattern for a channel with width defined by the semiconductor and no fringe current. Areal capacitance (solid lines) and dissipation factor (dashed lines) vs. frequency for (c) Al₂O₃ (red) and bilayer Al₂O₃ on ZrO₂ (orange) and (e) ZrO₂ MIM capacitors measured by VLF (10⁻² – 10¹ Hz, left x-axis) and LCR (10² – 3x10⁵ Hz, right x-axis) techniques. Mobility of TFTs (In₂O₃ semiconductor with (d) Al₂O₃ (red) and bilayer Al₂O₃ on ZrO₂ (orange) and (f) ZrO₂ gate dielectric) with the channel defined by the semiconductor, as in (b), calculated using the areal capacitance data in (c) and (e).....72
- Figure 4.12: I_D vs. V_D curves for transistor with bilayer Al₂O₃ on ZrO₂ gate dielectric and In₂O₃ channel. V_G is measured from 0V to 5V with 1V step and V_D is swept from 0V to 5V.....73
- Figure 5.1: Photonic curing process with three patterning modes. (a) Schematic of three photonic curing processes for forming ZrO₂ on PEN: blanket photonic curing (b-PC, top), shadow mask photonic curing (sm-PC, middle), and self-aligned photonic curing (sa-PC, bottom). The rightmost column shows optical images of each PC ZrO₂ film on PEN with patterned Al bottom contacts. The borders of the patterned ZrO₂ films are marked with orange dashed lines. Scale bars represent 500 μm. (b) Simulated film (orange) and substrate (grey) temperatures vs. time for a 20 ms light pulse on a ZrO₂ film deposited on top of Al contacts (PEN / Al / ZrO₂, solid lines) and directly on PEN (PEN / ZrO₂, dashed lines). Inset shows the temperature response of the sample on Al contacts over an extended (5 seconds) time frame. (c) Summary of photonic curing outcomes as a function of radiant exposure and pulse length. Conditions resulting in under-converted films (green), sa-PC (yellow), b-PC / sm-PC (blue), and substrate damage (red) are marked with circles for measured conditions and shaded regions are extrapolated.87
- Figure 5.2: Energy output of photonic curing system. Simulated (SimPulse[®], open circles) and measured (using a calibrated bolometer, closed circles) radiant exposure vs. pulse length per pulse for a constant lamp driver voltage of 280 V.....90

- Figure 5.3: Dielectric properties of photonicallly cured ZrO₂ films as a function of the number of pulses. (a) Areal capacitance vs. frequency of MIM capacitors made from the dried ZrO₂ precursor and from photonicallly cured films (5.23 J/cm² per pulse, 20 ms pulse length, 0.2 Hz repetition rate) using 1 to 20 pulses. (b) Bar graph showing the low frequency (10³ Hz, hashed bars) and high frequency (10⁶ Hz, solid bars) areal capacitance for each condition in (a) with a photo of a completed device as the inset. (c) Dissipation factor vs. frequency for each of the capacitance measurements in (a).92
- Figure 5.4: Dielectric properties of photonicallly cured ZrO₂ films as a function of pulse length. (a) Areal capacitance vs. frequency of MIM capacitors made from the dried ZrO₂ precursor and from photonicallly cured films with pulse length varied from 0.5 ms to 20 ms and radiant exposure from 0.33 J/cm² to 5.23 J/cm² (0.2 Hz repetition rate, 20 pulses). (b) Bar graph showing the low frequency (10³ Hz, hashed bars) and high frequency (10⁶ Hz, solid bars) areal capacitance for each condition in (a). (c) Dissipation factor vs. frequency for each of the capacitance measurements in (a).92
- Figure 5.5: Areal capacitance and dissipation factor for the three different processing modes. Areal capacitance (left axis) and dissipation factor (right axis) for b-PC (red), sm-PC (orange), and sa-PC (black) ZrO₂ films on PEN.....93
- Figure 5.6: Different thickness of ZrO₂ dielectric films. (a) Optical images of a single thin layer of sm-PC ZrO₂ on a patterned bottom Al contact on PEN showing a smooth film and good adhesion to Al (left), a single thick sm-PC ZrO₂ layer showing poor adhesion between the oxide and substrate (middle), and two thin sm-PC ZrO₂ layers with good adhesion and a smooth surface (right). The two areas in the right image are due to misalignment of masks in the two-step process. Scale bars represent 50 μm. (b) Areal capacitance (left axis, solid lines) and dissipation factor (right axis, dashed lines) for a single-layer (blue) and two-layer (red) ZrO₂ capacitor. (c) Leakage current density vs. applied electric field for the single layer (blue) and two-layer (red) ZrO₂ capacitors.....94
- Figure 5.7: Atomic force microscopy (AFM) thickness determination of two-layer b-PC ZrO₂ film. (a) AFM image of Al contact (left), one ZrO₂ layer (middle), and two ZrO₂ layers (right) on PEN. (b) Histogram of heights in (a) with the lowest peak (Al contact) normalized to height = 0 nm, the second peak (one layer of ZrO₂) at 19 nm, and the third peak (two layers of ZrO₂) at 35 nm.95
- Figure 5.8: Areal capacitance and dissipation for ZrO₂ dielectric cured using a single photonic curing pulse on an upgraded tool. Areal capacitance (left axis) and dissipation factor (right axis) for ZrO₂ exposed to a single 100 ms photonic curing pulse.97

LIST OF TABLES

Table 2.1: Capacitive, current-voltage, and In ₂ O ₃ transistor properties for different dielectrics on Si substrates. Capacitance is measured at 10 kHz, and leakage current density is measured at a field of 2 MV/cm. The number of coats for each dielectric is shown in parentheses next to the thickness.	22
Table 3.1: The average channel mobility for TFTs with In ₂ O ₃ annealed at different temperatures. Mobility is calculated using gate capacitance measured at both 10 kHz and 20 Hz.	47
Table 4.1: Literature survey of high-mobility (> 30 cm ² ·V ⁻¹ ·s ⁻¹) oxide TFTs on solution-processed Al ₂ O ₃ gate dielectrics.	56

LIST OF ABBREVIATIONS AND SYMBOLS

acac	Acetylacetonate
AFM	Atomic Force Microscopy
ALD	Atomic Layer Deposition
b-PC	Blanket Photonic Curing
C-f	Capacitance-Frequency
CTE	Coefficient of Thermal Expansion
CVD	Chemical Vapor Deposition
DI	Deionized
DMPA	2,2-dimethoxy-2-phenyl Acetophenone
e-beam	Electron Beam
FTIR	Fourier-Transform Infrared Spectroscopy
I_D	Drain Current
I_G	Gate Current
IGZO	Indium Gallium Zinc Oxide
$I_{on/off}$	Current On/Off ratio
ITO	Indium Tin Oxide
IZO	Indium Zinc Oxide
MIM	Metal-Insulator-Metal
MOE	2-methoxyethanol
M-O-M	Metal-Oxygen-Metal Bond
PECVD	Plasma-Enhanced Chemical Vapor Deposition
PEN	Polyethylene Naphthalate
PET	Polyethylene Terephthalate
PI	Polyimide
PSC	Perovskite Solar Cell
PVD	Physical Vapor Deposition
RH	Relative Humidity

S / D	Source / Drain
sa-PC	Self-Aligned Photonic Curing
SMP	Shape Memory Polymer
sm-PC	Shadow Mask Photonic Curing
SS	Subthreshold Swing
TATATO	1,3,5-triallyl-1,3,5-triazine-2,4,6(1H,3H,5H)-trione
TCMDA	Tricyclodecane Dimethanol Diacrylate
TFT	Thin Film Transistor
TMICN	Tris[2-(3-ercaptopropionyloxy)ethyl] Isocyanurate
UVO	UV-Ozone
V_D	Drain Voltage
V_G	Gate Voltage
VLF	Very Low Frequency
XPS	X-ray Photoelectron Spectroscopy
XRD	X-ray Diffraction
ϵ_0	Permittivity of Free Space
ϵ_r	Relative Permittivity
μ	Mobility

CHAPTER 1

INTRODUCTION

Thin film electronics are electronic devices in which the functional materials, e.g. semiconductors, conductors, and dielectrics, are deposited on top of a substrate which acts primarily as a mechanical support. This differs from traditional electronic devices where the substrate, such as a silicon wafer, acts as both the mechanical support and the active semiconductor material. A major advantage of thin film electronics is that by decoupling the physical support of the device from the active material, the substrate choice is no longer constrained by the substrate's electrical properties. With this constraint lifted, the choice of potential substrate properties – transparency, biocompatibility, cost, flexibility, etc. – that can be selected to complement and enhance the performance and manufacturing of devices broadens immensely. For example, thin film solar cells are built on transparent substrates that allow light to reach the devices, LED and LCD screens utilize large area transparent substrates on which thin film transistors and/or organic LEDs are deposited, implantable biosensors and nerve stimulation devices are made on biocompatible polymer substrates that are stiff for fabrication and implantation, yet nearly as soft as human tissue once implanted,¹ and curved screens and sensor or antenna arrays can achieve their shapes through the use of flexible substrates.

The active materials that make up thin film electronics are traditionally deposited by vacuum-based techniques (e.g. evaporation, sputtering, chemical vapor deposition, and atomic layer deposition), the same techniques used extensively for conventional wafer-based electronics. However, these materials can also be deposited by solution-based processes in which inks are coated (by blade coating, slot die coating, or spray coating, etc.) or printed (by ink jet printing,

gravure printing, screen printing, or flexographic printing, etc.) to create the films. This compatibility with solution-deposition is the second major advantage of thin film electronics. By combining their compatibility with flexible substrates and their ability to be solution-deposited, thin film electronics can be manufactured by roll-to-roll processing. Roll-to-roll processing, in which films are deposited on large rolls of flexible substrates at up to hundreds of m/min, is already an established manufacturing technique for thin film coatings and RFID antennas,^{2,3} but is not yet viable for large scale production of active electronic device and integrated circuits. However, just as the worldwide spread of the printing press, due to its ability to produce printed materials much faster and at much lower cost than previously possible, enabled the mass availability of printed books, roll-to-roll processing offers the promise of the widespread availability of low-cost printed electronics. The challenges of accomplishing this goal, as they relate to materials' properties and processing, are the subject of this dissertation.

1.1 Materials and Processing for Solution-Deposited Thin Film Electronics

In the field of thin film electronics, organic electronic materials are widely studied, particularly for solar cell or light emitting diode applications, due to their low-temperature and solution processability. However, organic semiconductors suffer from low electron mobility, poor environmental instability,⁴ and high cost, and organic dielectrics have low dielectric constants. Metal oxides, which can act as insulators, conductors, or semiconductors, show better stability and higher mobility than organic films, and have the benefit of a wide band gap which allows for use in transparent applications. Solution processable metal oxides are promising for high-throughput, low-cost, roll-to-roll processing on flexible substrates.⁵ To realize roll-to-roll processing, however, the processing conditions for metal oxide films must be compatible with

the thermal limits of the flexible substrates. Furthermore, to take advantage of the potential throughput of roll-to-roll manufacturing, the annealing time for metal oxide films must be made short enough to match the high web speeds possible with printing and coating methods, and high-speed patterning methods must be developed.

1.1.1 Sol-Gel Process

Sol-gel chemistry has been used to synthesize a wide variety of metal oxide materials.⁶ In the sol-gel process, metal oxide precursors in a solution form a 'sol' through hydrolysis and partial condensation. This sol can be spin coated or otherwise deposited to form a thin film. Subsequent drying in air promotes polycondensation into a 'gel'. This 'gel' can be further dried at an elevated temperature to remove residual solvent and densify the film, and is finally annealed at a high temperature to complete the metal-oxygen bonding network and remove all organic and hydroxyl moieties.⁷ The temperatures required to achieve good film properties (high density, low leakage current, and high permittivity for dielectrics, as well as high mobility for semiconductors) are typically greater (~400-800 °C) than the degradation temperature of flexible, transparent plastic substrates (typically < 250 °C). The annealing time for this thermal process is also typically longer than 20 minutes and up to several hours.

Coating methods can achieve good uniformity and large area coverage, but subtractive patterning (typically photolithography) is not possible on precursor films as they are not resistant to any chemical solvents or etchants. Annealing an un-patterned film on a flexible polymer substrate can result in cracking of the metal oxide due to a large coefficient of thermal expansion (CTE) mismatch with the flexible substrate. Patterned sol-gel precursor films can be directly formed by printing techniques, but they increase the complexity of the roll-to-roll process

compared to coating,² and their implementation does not otherwise address the problems associated with thermal annealing. Solutions to these roadblocks are discussed in the following sections.

1.1.2 Lowering the Sol-Gel Processing Temperature

There are several approaches to lowering the required processing temperature for sol-gel derived metal oxide thin films. Very reactive precursor solutions, such as those derived from metal chlorides, may be used as precursors, but these lead to hydrolysis reactions which are difficult to control. Electromagnetic energy (photons) may be provided to the precursor films in the form of microwaves,⁸ excimer lasers,⁹ or incoherent UV radiation.¹⁰⁻¹² Exposure to UV radiation is studied in this work due to its potential to also solve the patterning problem. UV can be absorbed by the precursors and converted to thermal energy while promoting the creation of reactive oxygen species within the film.¹³ By exposing the precursor film to UV light through a shadow mask, polycondensation can be promoted in the exposed areas leaving them resistant to a solvent used to remove unexposed portions of the film.¹⁴ This greatly simplifies the traditional photolithography process while also allowing for final annealing to occur on a pre-patterned precursor film. By allowing for the release of stress around the patterned features during annealing, a crack-free metal oxide film can be formed.

Another approach to lowering the annealing temperature is solution combustion synthesis.¹⁵⁻¹⁷ When an oxidizer (e.g. nitrate ions from a metal nitrate precursor) and a fuel (e.g. acetylacetone (acac), urea, glycine, or even the organic solvent itself) are present in a precursor film, additional thermal energy can be released as the result of a redox reaction. This can raise the local film temperature much higher than the temperature of the substrate which is

determined by the external heating source. This approach can be combined with the UV method and is especially useful when the organic fuel molecules also act as UV absorbers.

1.1.3 Photonic Curing

Both solution combustion and UV curing still require equilibrium heating of the film and substrate to at least 150 °C,^{11,18} which is time consuming and can lead to failure of the film due to the CTE mismatch between film and substrate. Photonic curing addresses both issues by using intense pulses of broad spectrum (200 – 1500 nm) light from a xenon flash lamp to briefly heat the film without significant heating of the substrate.¹⁹ The short duration of the pulses, from 20 μs to 100 ms means that despite the high power delivery (up to 50 kW/cm²), only a small amount of energy is delivered (< 100 J/cm²). This is an equivalent energy exposure to that of sitting in the afternoon sun for about 15 minutes or less; however, photonic curing can deliver this exposure in just 2 ms at an intensity that is 500,000 times that of the afternoon sun. Figure 1.1a shows the simulated temperature response of a thin aluminum film on three flexible plastic substrates – polyethylene terephthalate (PET), polyimide (PI), and polyethylene naphthalate (PEN). During the 0.5 ms light pulse, the light is absorbed by the thin film and the temperature at the surface rises significantly. The high power of the light pulse and low thermal mass of the film are responsible for the rapid heating. However, the temperature of the film also depends on the thermal conductivity of the substrates, which determines the rate of heat transfer from the film to the substrate by conduction during the light pulse. The higher the thermal conductivity of the substrate, the lower the peak temperature reached by the film. When the light pulse ends after 0.5 ms, the temperature of the film falls quickly as heat is conducted to the substrate. Figure 1.1b shows the temperature at the bottom of each of the three substrates over an extended time frame

(200 ms). As the heat generated in the film is transferred through the substrate, the entire sample eventually reaches thermal equilibrium after approximately 100 ms. Since the amount of energy delivered to the three substrates is the same, the final temperature of each substrate depends on its heat capacity. The result is that the films, in this example, are heated briefly to 400 – 800 °C, while the substrates are maintained at a temperature below 80 °C. This process can achieve film conversion in very short time frames, enabling high throughput curing films, and since the substrate is not significantly heated, its high CTE is less problematic than in equilibrium heating.

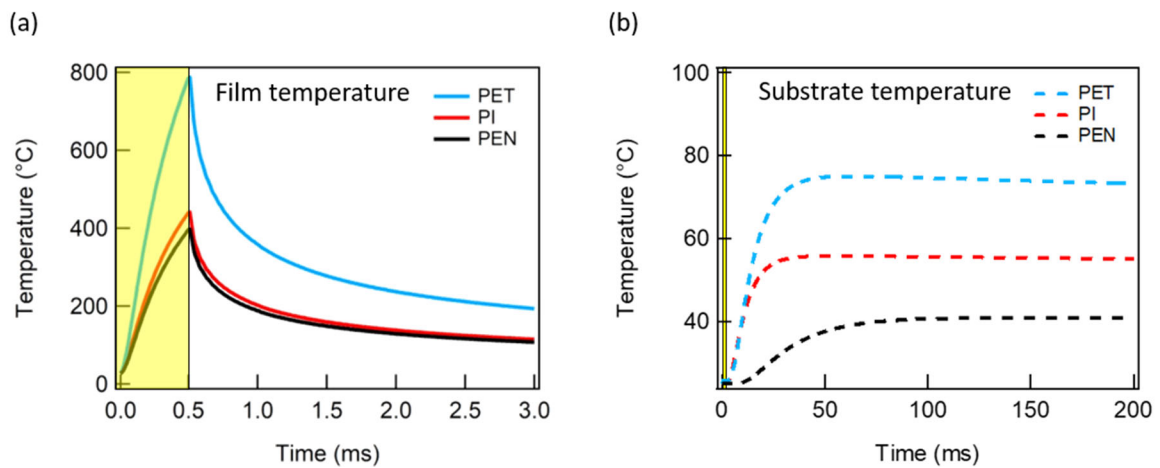


Figure 1.1: Temperature response of film and substrate during photonic curing. (a) Film temperature vs. time for a representative film on PET (blue), PI (red), and PEN (black) substrates from 0 to 3 ms seconds after the onset of a 0.5 ms photonic curing pulse (shaded in yellow). (b) Substrate temperatures for the devices in (a) from 0 to 200 ms after the onset of the pulse.

1.2 Flexible Substrates

Quality metal oxide films can be formed on rigid substrates by the sol-gel method by annealing at high temperatures. Even by using the above methods to greatly reduce the annealing temperature to below 250 °C, many transparent, flexible substrates remain incompatible with metal oxide sol-gel processing. Some amorphous polymer substrates, such as polyimide (PI),

have very high heat stability (350 °C), but are less transparent with a yellow color.

Semicrystalline polymers such as polyethylene terephthalate (PET) and polyethylene naphthalate (PEN) have low glass transition temperatures (T_g , 78 °C and 120 °C, respectively). Above their T_g , large dimensional changes occur which may result in film cracking. Some residual strain persists after cooling which results in patterning mismatch over large distances when subsequent films are deposited. These polymers can be heat stabilized to minimize the dimensional effects of heating, but still have low upper operating temperatures of 150 °C and 220 °C respectively.^{20–22} In Chapter 5, we demonstrate photonic curing as a viable method for high-speed curing of ZrO₂ dielectric films on PEN.

Shape memory polymer (SMP) substrates, whose shape can be modified by heating while applying a stress and recovered by heating without applied stress, can be useful for non-planar applications and those requiring a change in shape upon an applied stimulus during use.²³ These materials offer the additional benefit of returning to their original dimensions upon heating,²⁴ allowing the potential for precise alignment of patterned features over large distances during manufacturing. The SMP substrate used in this work has a maximum processing temperature above 250 °C,²⁵ but like the semicrystalline polymers, it suffers from large dimensional changes above its T_g at 80 °C. In Chapter 3, we demonstrate the successful fabrication of high mobility In₂O₃ thin film transistors by solution processing on these SMP substrates using the UV patterning method.

1.3 Thin Film Electronic Devices

1.3.1 Thin Film Transistors

Thin film transistors (TFTs) (Figure 1.2) are a three-terminal electronic device in which the current in the channel between a source and drain contact is modulated by applying a voltage bias to the electrically isolated gate contact. Band bending in the semiconductor channel near the semiconductor/dielectric interface results in an accumulation of majority-type carriers whose increase in concentration depends on the capacitance of the gate dielectric and the applied gate voltage. The amount of source-drain current in this ‘on’ state depends on the field-effect mobility, μ_{FE} , which relates the change in the channel current to the change in gate bias as follows:

$$\mu_{FE} = \left(\frac{d\sqrt{I_D}}{dV_G} \right)^2 2 \frac{L}{WC} \quad (1.1)$$

I_D is the drain-source channel current, V_G is the applied gate voltage, L is the channel length, W is the channel width, and C is the areal gate capacitance. The threshold voltage, V_{th} , is extracted from the $\sqrt{I_D}$ vs. V_G plot and is defined as the intercept of a linear fit with the x-axis. Another important TFT device performance parameter is the subthreshold swing (SS), a measure of how quickly the channel current increases with respect to gate voltage at the onset of the ‘on’ condition below the threshold voltage calculated by:

$$SS = \frac{dV_G}{d\log_{10}(I_D)} \quad (1.2)$$

The final TFT parameter used here is $I_{on/off}$, the ratio of the current in the on-state above V_G to that in the off-state. Large $I_{on/off}$ allows for high gain, high signal to noise, and low power losses in devices using TFTs.

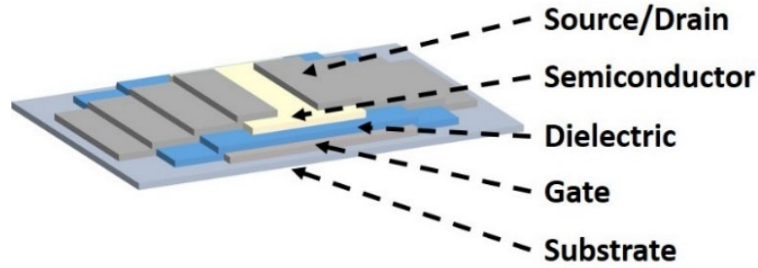


Figure 1.2: Basic TFT structure with a substrate, bottom gate, gate dielectric, semiconductor channel, and top source and drain contacts.

1.3.2 Metal – Insulator – Metal Capacitors

Metal – insulator – metal (MIM) capacitors consist of a thin film dielectric layer sandwiched between two thin film electrodes. The capacitance, C , of the MIM is determined by:

$$C = \epsilon_0 \epsilon_r \frac{A}{t} \quad (1.3)$$

ϵ_0 is the permittivity of free space, ϵ_r is the relative permittivity of the dielectric, A is the area defined by the overlap of the two electrodes, and t is the thickness of the dielectric. This basic device structure serves as the gate for TFTs. The important characteristics of the MIM capacitor for TFT performance are areal capacitance (capacitance per unit area), leakage current density, and breakdown field. High areal capacitance results in large on current (Equation 1.1) and low leakage current density provides low off current; together, they contribute to a high $I_{on/off}$ ratio. A high breakdown field allows for stable operation over a large voltage range.

1.4 Outline of Dissertation

Chapters 2 and 3 of this dissertation focus on solving the challenge of fabricating solution-deposited metal oxide capacitors and transistors on SMP substrates. We describe how the materials and deposition methods are selected and examine the effects of the processing

conditions on the properties of the materials and performance of the devices. In Chapter 4, we further investigate the behavior of films and devices fabricated by the method developed in the previous chapters. We identify moisture in the air as being responsible for undesirable device behaviors and look at how different materials and processing conditions affect this outcome. Finally, in Chapter 5 we develop a process for high speed deposition and curing of oxide dielectrics on flexible PEN substrates, which reveals a path towards high-throughput and low-cost roll-to-roll manufacturing of flexible oxide electronics.

1.5 References

- (1) Simon, D.; Ware, T.; Marcotte, R.; Lund, B. R.; Smith, D. W.; Prima, M.; Rennaker, R. L.; Voit, W. A Comparison of Polymer Substrates for Photolithographic Processing of Flexible Bioelectronics. *Biomed Microdevices* **2013**, *15* (6), 925–939.
- (2) Abbel, R.; Galagan, Y.; Groen, P. Roll-to-Roll Fabrication of Solution Processed Electronics. *Adv Eng Mater* **2018**, *20* (8), 1701190.
- (3) Palavesam, N.; Marin, S.; Hemmetzberger, D.; Landesberger, C.; Bock, K.; Kutter, C. Roll-to-Roll Processing of Film Substrates for Hybrid Integrated Flexible Electronics. *Flexible Print Electron* **2018**, *3* (1), 014002.
- (4) Sun, Y.; Rogers, J. Inorganic Semiconductors for Flexible Electronics. **2007**, *19*, 1897–1916.
- (5) Lorenz, M.; Rao, R.; Venkatesan, T.; Fortunato, E.; Barquinha, P.; Branquinho, R.; Salgueiro, D.; Martins, R.; Carlos, E.; Liu, A.; et al. The 2016 Oxide Electronic Materials and Oxide Interfaces Roadmap. *J Phys D Appl Phys* **2016**, *49* (43), 433001.
- (6) Brinker, C.; Scherer, G. Sol–Gel Science: The Physics and Chemistry of Sol–Gel Processing. **1990**.
- (7) Danks, A.; Hall, S.; Schnepf, Z. The Evolution of ‘Sol–Gel’ Chemistry as a Technique for Materials Synthesis. *Mater Horizons* **2015**, *3* (2), 91–112.
- (8) Jun, T.; Song, K.; Jeong, Y.; Woo, K.; Kim, D.; Bae, C.; Moon, J. High-Performance Low-Temperature Solution-Processable ZnO Thin Film Transistors by Microwave-Assisted Annealing. *J Mater Chem* **2010**, *21* (4), 1102–1108.

- (9) Dellis, S.; Isakov, I.; Kalfagiannis, N.; Tetzner, K.; Anthopoulos, T. D.; Koutsogeorgis, D. C. Rapid Laser-Induced Photochemical Conversion of Sol–Gel Precursors to In₂O₃ Layers and Their Application in Thin-Film Transistors. *J Mater Chem C* **2017**, *5* (15), 3673–3677.
- (10) Tetzner, K.; Lin, Y.-H.; Regoutz, A.; Seitkhan, A.; Payne, D. J.; Anthopoulos, T. D. Sub-Second Photonic Processing of Solution-Deposited Single Layer and Heterojunction Metal Oxide Thin-Film Transistors Using a High-Power Xenon Flash Lamp. *J Mater Chem C* **2017**, *5* (45), 11724–11732.
- (11) Kim, Y.-H.; Heo, J.-S.; Kim, T.-H.; Park, S.; Yoon, M.-H.; Kim, J.; Oh, M.; Yi, G.-R.; Noh, Y.-Y.; Park, S. Flexible Metal-Oxide Devices Made by Room-Temperature Photochemical Activation of Sol–Gel Films. *Nature* **2012**, *489* (7414), 128.
- (12) Hwang, Y.; Seo, S.-J.; Jeon, J.-H.; Bae, B.-S. Ultraviolet Photo-Annealing Process for Low Temperature Processed Sol-Gel Zinc Tin Oxide Thin Film Transistors. *Electrochem Solid-state Lett* **2012**, *15* (4), H91.
- (13) Hwang, J.; Lee, K.; Jeong, Y.; Lee, Y.; Pearson, C.; Petty, M. C.; Kim, H. UV-Assisted Low Temperature Oxide Dielectric Films for TFT Applications. *Adv Mater Interfaces* **2014**, *1* (8), 1400206.
- (14) Rim, Y.; Chen, H.; Liu, Y.; Bae, S.-H.; Kim, H.; Yang, Y. Direct Light Pattern Integration of Low-Temperature Solution-Processed All-Oxide Flexible Electronics. *ACS Nano* **2014**, *8* (9), 9680–9686.
- (15) Liu, A.; Zhu, H.; Guo, Z.; Meng, Y.; Liu, G.; Fortunato, E.; Martins, R.; Shan, F. Solution Combustion Synthesis: Low-Temperature Processing for P-Type Cu:NiO Thin Films for Transparent Electronics. *Adv Mater* **2017**, *29* (34), 1701599.
- (16) Kim, M.-G.; Kanatzidis, M. G.; Facchetti, A.; Marks, T. J. Low-Temperature Fabrication of High-Performance Metal Oxide Thin-Film Electronics via Combustion Processing. *Nat Mater* **2011**, *10* (5), 382–388.
- (17) Wang, B.; Yu, X.; Guo, P.; Huang, W.; Zeng, L.; Zhou, N.; Chi, L.; Bedzyk, M. J.; Chang, R. P.; Marks, T. J.; et al. Solution-Processed All-Oxide Transparent High-Performance Transistors Fabricated by Spray-Combustion Synthesis. *Adv Electron Mater* **2016**, *2* (4), 1500427.
- (18) Park, Y.; Desai, A.; Salleo, A.; Jimison, L. Solution-Processable Zirconium Oxide Gate Dielectrics for Flexible Organic Field Effect Transistors Operated at Low Voltages. *Chem Mater* **2013**, *25* (13), 2571–2579.

- (19) Schroder, K. A. Mechanisms of Photonic CuringTM: Processing High Temperature Films on Low Temperature Substrates. *Technical Proceedings of the 2011 NSTI Nanotechnology Conference and Expo, NSTI-Nanotech 2011* **2011**, 2, 220–223.
- (20) Choi, M.-C.; Kim, Y.; Ha, C.-S. Polymers for Flexible Displays: From Material Selection to Device Applications. *Prog Polym Sci* **2008**, 33 (6), 581–630.
- (21) MacDonald, W. A. Engineered Films for Display Technologies. *J Mater Chem* **2003**, 14 (1), 4–10.
- (22) MacDonald, W.; Looney, M.; MacKerron, D.; Eveson, R.; Adam, R.; Hashimoto, K.; Rakos, K. Latest Advances in Substrates for Flexible Electronics. *J Soc Inf Display* **2007**, 15 (12), 1075–1083.
- (23) Zhao, Q.; Qi, J. H.; Xie, T. Recent Progress in Shape Memory Polymer: New Behavior, Enabling Materials, and Mechanistic Understanding. *Prog Polym Sci* **2015**, 49, 79–120.
- (24) Voit, W.; Ware, T.; Dasari, R. R.; Smith, P.; Danz, L.; Simon, D.; Barlow, S.; Marder, S. R.; Gall, K. High-Strain Shape-Memory Polymers. *Adv Funct Mater* **2010**, 20 (1), 162–171.
- (25) Gutierrez-Heredia, G.; Rodriguez-Lopez, O.; Garcia-Sandoval, A.; Voit, W. E. Highly Stable Indium-Gallium-Zinc-Oxide Thin-Film Transistors on Deformable Softening Polymer Substrates. *Adv Electron Mater* **2017**, 3 (10), 1700221.

CHAPTER 2

**SOLUTION-DEPOSITED Al_2O_3 DIELECTRIC TOWARDS FULLY-PATTERNED
THIN FILM TRANSISTORS ON SHAPE MEMORY POLYMER**

Authors – Trey B. Daunis,^a Gerardo Gutierrez-Heredia,^b Ovidio Rodriguez-Lopez,^{b,c} Jian Wang,^a
Walter E. Voit,^{a,b,c} and Julia W. P. Hsu^a

^aDepartment of Materials Science and Engineering, RL 10

^bDepartment of Electrical and Computer Engineering, EC 33

^cDepartment of Bioengineering, BSB 11

The University of Texas at Dallas

800 West Campbell Road

Richardson, Texas 75080-3021

Reprinted with permission from Trey B. Daunis, Gerardo Gutierrez-Heredia, Ovidio Rodriguez-Lopez, Jian Wang, Walter E. Voit, Julia W. P. Hsu, "Solution-Deposited Al_2O_3 Dielectric Towards Fully-Patterned Thin Film Transistors on Shape Memory Polymer," *Proc. SPIE 10105, Oxide-based Materials and Devices VIII*, 101051Z (February 24, 2017). DOI: 10.1117/12.2250393. Copyright 2017 Society of Photo-Optical Instrumentation Engineers (SPIE).

2.1 Preface

This chapter presents the results of the initial phase of my first research project. This project was a collaboration between the groups of Prof. Julia W. P. Hsu and Prof. Walter E. Voit. A shape memory polymer (SMP) substrate had previously been developed by Prof. Voit's research group, who had demonstrated its use as a substrate for vacuum-processed metal oxide thin film transistors (TFTs). The goal of this project was to combine the knowledge and expertise of Prof. Voit's group on the SMP substrate and TFT device fabrication and analysis with that of Prof. Hsu's group on sol-gel metal oxide thin film fabrication and characterization in order to fabricate solution-processed metal oxide TFTs on SMP. This chapter details the identification of the unique challenges of fabricating sol-gel oxide TFTs on SMP. TFTs are fabricated on Si substrates by a method designed to be compatible with SMP substrates, and Al₂O₃ films are demonstrated on SMP. These devices serve as the foundation for the TFTs in the second half of this project, described in Chapter 3.

My contributions to this work were identifying the issues involved in annealing solution-deposited oxide thin films on SMP and developing the process to overcome them, fabricating devices, characterizing film properties, measuring and analyzing the devices, and preparing the manuscript. Dr. Gerardo Gutierrez-Heredia provided training on fabricating vacuum-processed oxide films and devices on SMP as well as guidance on electrical characterization and analysis. Ovidio Rodriguez-Lopez assisted with device fabrication. Dr. Jian Wang helped with metal oxide sol-gel technique and thin film analysis. Prof. Walter E. Voit provided expertise on the SMP substrate. Prof. Julia W. P. Hsu provided valuable guidance on all aspects of the project and assistance with manuscript preparation.

2.2 Abstract

Solution deposition has potential for highly cost-effective fabrication of thin film transistors (TFTs) on flexible substrates. Shape memory polymer (SMP), with improved thermal mechanical response, may enable large-area flexible devices, as well as add control to the product shape and modulus. To date, TFTs made on SMP substrates have been limited to vacuum-deposition methods. While TFTs processed through more economical solution-based techniques achieve device performance close to their vacuum-processed counterparts, they have not yet been demonstrated on SMP substrates due to the required high calcination temperatures ($> 500\text{ }^{\circ}\text{C}$). To take full advantages of SMP, low temperature ($< 200\text{ }^{\circ}\text{C}$) solution-based processing is highly desirable. Compatibility of the deposition process with the substrate and previously deposited films is essential. Here, we develop a process that incorporates direct UV patterning which will allow for fabrication of oxide TFTs on SMP using a reduced number of processing steps. Rigid In_2O_3 TFTs, deposited from solution-combustion synthesis, are fabricated on Si substrates with different solution-deposited dielectrics to evaluate their potential for transferring to SMP.

2.3 Introduction

Thin film transistors (TFTs) fabricated on flexible substrates are targeted for applications in medical devices, displays, photovoltaics, sensors, and radio-frequency ID tags. Recently developed shape memory polymer (SMP) substrates display exceptional characteristics such as low surface roughness,¹ which eliminates the need for a planarization layer,² and highly recoverable thermal expansion,³ which may allow for large-area patterning even when thermal

cycling is required between deposition of multiple layers. Among materials used in flexible TFT applications, metal oxides offer superior time, thermal, and environmental stability and a wide variety of functions, e.g. dielectrics (Al_2O_3 , Y_2O_3 , ZrO_2), semiconductors (IGZO, In_2O_3 , ZnO , IZO), and transparent contacts (ITO).^{4,5}

Fabrication of metal oxide thin film devices is commonly carried out by conventional vacuum-deposition methods such as plasma enhanced chemical vapor deposition (PECVD), physical vapor deposition (PVD), and atomic layer deposition (ALD). The processing temperatures are usually above 250 °C, because the quality of dielectrics for TFTs suffers when they are deposited at lower temperatures.⁶ For example, PECVD and ALD dielectric films deposited at low temperatures are less dense, leading to higher leakage current densities, and have a higher hydrogen content, degrading TFT performance, compared to those deposited at high temperatures.⁶⁻⁹ In our study, we have also investigated electron-beam (e-beam) evaporated SiO_2 and Al_2O_3 , which exhibit leakage current densities too large and breakdown fields too small for TFT operation. Additionally, vacuum deposition processes are capital-intensive and time-consuming for large-scale manufacturing.

Solution deposition shows potential as an inexpensive, high-throughput alternative to the vacuum-deposition methods. However, traditional sol-gel techniques require annealing temperatures that are too high for many flexible substrates, including SMP, and therefore have not been demonstrated. There is additional difficulty in patterning multiple layers of solution-deposited metal oxide films in a device: sequential solution deposition and patterning of metal oxide films by traditional photolithography processes can result in damage to the underlying layer without etch stops. Recent developments towards solving these issues include metal oxide

precursor solutions containing a fuel, e.g. acetylacetonone (acac), and an oxidizer, e.g. a nitrate salt (also the metal source), which have been shown to produce metal oxide films by solution combustion at lower temperatures than traditional sol-gel films.¹⁰ Patterning of precursor films containing acac by exposure to UV radiation through a shadow mask prior to thermally annealing has also been demonstrated.¹¹ This allows for patterning of precursor films prior to metal oxide formation, removing the need for photoresist deposition and residual organic removal, aggressive etchants, etch-stop layers, and multi-mask processing steps.

In this work, we investigate solution-based deposition of metal oxide dielectric films for fabricating fully patterned spin-coated TFTs on SMP. Al_2O_3 is chosen as the dielectric for solution deposition due to its high bulk dielectric constant (above 9.0) and demonstration of TFTs with high performance.^{12,13} We find that using acac-containing precursor solutions to deposit Al_2O_3 dielectric results in In_2O_3 TFTs with improved transfer characteristics – field effect mobility (μ) and subthreshold swing (SS) – compared to those using thermally grown SiO_2 as the dielectric. However, higher leakage current densities in these Al_2O_3 films require many coats to be deposited, because a thick single coat increases film porosity and reduces performance due to gas release during combustion and metal oxide formation.¹⁴ Therefore, we further develop an acac-free method to increase the thickness of Al_2O_3 per coat while also reducing the leakage current density. TFTs on rigid substrates with Al_2O_3 dielectric fabricated at 250 °C from the acac-free method demonstrate improved performance over those with Al_2O_3 dielectric made from acac-containing solutions. Even with only two coats processed at a reduced annealing temperature (150 °C), which greatly reduces the risk of film cracking during annealing of devices on SMP substrates, the leakage current density of these films is comparable to that of

films from acac-containing solutions processed 250 °C. While many challenges remain, results on rigid Si substrates suggest that Al₂O₃ films made from acac-free precursor solution are a promising gate dielectric for solution-deposition of TFTs on SMP substrates.

2.4 Experimental Details

2.4.1 Device Structure

Rigid transistors and capacitors were fabricated on degenerately doped p⁺⁺ Si substrates (University Wafer, resistivity = 0.001 – 0.005 Ω*cm), which also functioned as the bottom contact (gate contact for transistors). The Si substrates were cleaned by sonication in a detergent solution for 10 minutes, followed by 10 minutes each in acetone and isopropyl alcohol. SMP substrates on glass were fabricated according to published procedures¹ and cleaned by rinsing in DI water and isopropyl alcohol. All substrates were dried with an air gun and exposed to UV-ozone for 20 minutes prior to deposition of the first film. 100-nm thick patterned bottom metal contacts (Al or Au) were deposited on SMP and glass substrates by e-beam or thermal evaporation through an invar shadow mask held in place by a magnet. Dielectric and semiconductor films were deposited as described in the following subsections, and 100-nm Al top contacts (source and drain for transistors) were deposited by thermal evaporation through another invar shadow mask.

2.4.2 Metal Oxide Precursor Solutions

All chemicals were purchased from Alfa Aesar unless otherwise noted. Acac-containing precursor solutions were prepared by first dissolving Al(NO₃)₃·9H₂O or In(NO₃)₃·3H₂O in

2-methoxyethanol (MOE) to obtain 0.1 – 0.4 M solutions for Al₂O₃ films or 0.1 M solutions for In₂O₃ films. For Al₂O₃ recipes containing acac, 0.1 M acac and 0.1 M ammonium hydroxide (from 14.8 M aqueous NH₃) were added. In₂O₃ precursor solutions were prepared using 0.1 M – 0.2 M acac and 0.1 M – 0.2 M ammonium hydroxide. All acac-containing solutions were stirred overnight at room temperature and filtered through 0.22 µm filters prior to spin coating.

Acac-free Al₂O₃ precursor solutions consisting of 0.13 – 0.4 M Al(NO₃)₃·9H₂O in MOE were stirred overnight uncapped on a hotplate at 90 °C to allow evaporation of water introduced with the Al(NO₃)₃·9H₂O; this step was found to improve film formation. The evaporated solvent volume of the acac-free solutions was compensated with fresh MOE, and the solutions were stirred uncapped at 90 °C for an additional 20 minutes. Prior to spin coating, acac-free solutions were cooled to room temperature and were filtered through 0.22 µm filters.

2.4.3 Metal Oxide Film Deposition

All metal oxide films on Si substrates were spin coated from precursor solutions at 3000 rpm for 30 seconds, followed by an immediate 1 minute of drying on an 80 °C hotplate. An invar shadow mask was positioned on top of the sample and held in place by a magnet behind the substrate. Both Al₂O₃ and In₂O₃ films made from acac-containing solutions (Al₂O₃ thickness 32 nm – 105 nm, In₂O₃ thickness ~20 nm) were exposed to UV-ozone (Bioforce Nanosciences Procleaner Plus) for 10 minutes, followed by a 10 second rinse in a developing solution consisting of a 1:20 acetic acid to methanol volume ratio to remove the unexposed portions of the film. Samples were thoroughly rinsed in DI water and dried with an air gun. For each material deposited, this process was repeated 3-8 times (Table 2.1) to achieve the desired

thickness before the film was annealed on a hotplate at the final temperature (150 °C or 250 °C) for 30 minutes in air.

Al₂O₃ films made from acac-free solutions (20 nm – 86 nm thick) were exposed to UV-ozone through the shadow mask for 45 minutes to 1 hour. After developing using the same developing solution, the samples were exposed to UV-ozone without a shadow mask for an additional 1 hour and then heated to and held at the final annealing temperature (150 or 250 °C) on a hotplate in air for 10 minutes. Only two coats were deposited for films made from acac-free solutions. The films were annealed on a hotplate at 150 °C or 250 °C for 30 minutes in air, and then placed in UV-ozone overnight.

On SMP substrates, the initial 80 °C annealing time after spin coating was increased to 3 minutes for all films to allow for heat transfer through the thick (1 mm) glass substrate. All high-temperature annealing processes on SMP were performed by placing the sample on an 80 °C hotplate for 3 minutes, and then increasing the temperature at a rate of 10 °C/min to the desired temperature, at which the SMP samples were held for 30 minutes. Samples were cooled on the hotplate until below 80 °C before removing.

Evaporated SiO₂ and Al₂O₃ films (243 nm) were deposited by e-beam evaporation at a rate of 5 - 10 Å/sec at room temperature. 168 nm SiO₂ was grown at 1050 °C for 132 minutes in an O₂ environment, and 312 nm SiO₂ was grown at 1000 °C for 42 minutes in an H₂O environment.

2.4.4 Film and Device Characterization

Electrical measurements were performed in air in a Cascade Microtech probe station. Capacitance was measured at 0 V DC bias with a 50 mV AC bias at 10 kHz (Agilent 4284A Precision LCR Meter). Capacitor area was 0.0016 cm². Current-voltage measurements for

breakdown field, leakage current measurements, and transistor measurements were performed using a Keithley 4200-SCS Semiconductor Characterization System. Transistor channel length was 100 μm and channel width was 1000 μm , as defined by shadow masks. Film thicknesses were determined by spectroscopic ellipsometry (J. A. Woollam M-2000DI) with measurements taken from 280 to 1690 nm at 55°, 65°, and 75° incident angle. Data for dielectric films were fitted using a Cauchy model.

2.5 Results and Discussion

TFTs made using HfO_2 deposited by ALD demonstrate the incompatibility of conventional vacuum-deposited dielectrics with the SMP substrate. Rigid devices using HfO_2 deposited at 200 °C on Si (and post-annealed at 250 °C after In_2O_3 deposition) show excellent transistor parameters ($\mu = 7.2 \text{ cm}^2/\text{V}\cdot\text{s}$, $\text{SS} = 350 \text{ mV/dec}$). However, HfO_2 deposited as low as 150 °C on SMP, shown in Figure 2.1, develops cracks during processing, leading to low device yield. SiO_2 and Al_2O_3 thermally evaporated through an invar shadow mask are also tested, but the resulting films have leakage current densities too high and breakdown fields too low for transistor operation (Table 2.1).

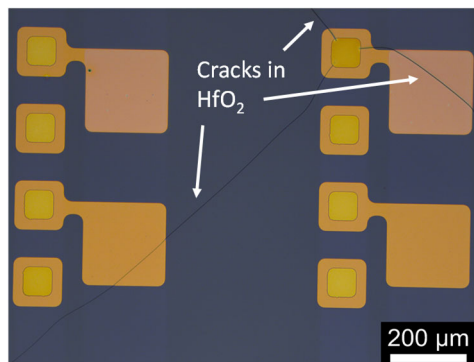


Figure 2.1: HfO_2 deposited by ALD at 150 °C. Two of the four capacitors shown (no top contacts in picture) are compromised by cracks that develop during processing.

Table 2.1: Capacitive, current-voltage, and In₂O₃ transistor properties for different dielectrics on Si substrates. Capacitance is measured at 10 kHz, and leakage current density is measured at a field of 2 MV/cm. The number of coats for each dielectric is shown in parentheses next to the thickness.

Material	Thickness (nm)	Areal Capacitance (F/cm ²)	ϵ_r	Breakdown Field (MV/cm)	Leakage Current Density (A/cm ²)	Mobility (cm ² /V*s)	Threshold Voltage (V)	Sub-threshold Swing (mV/dec)
Thermally Grown								
SiO ₂	312 (1)	1.1 x 10 ⁻⁸	3.9	>7	3.7 x 10 ⁻¹¹	0.4	1.0	810
SiO ₂	168 (1)	2.0 x 10 ⁻⁸	3.8	7.5	2.1 x 10 ⁻¹⁰	0.3	3.8	1020
Evaporated								
SiO ₂	243 (1)	3.9 x 10 ⁻⁸	10.6 ^a	0.16	N/A	--- ^b	--- ^b	--- ^b
Al ₂ O ₃	243 (1)	3.3 x 10 ⁻⁸	8.9	1.0	N/A	--- ^b	--- ^b	--- ^b
Al ₂ O ₃ Solution with acac 250 °C								
0.2M	45 (3)	1.1 x 10 ⁻⁷	5.8	6.6	1.7 x 10 ⁻⁵	2.5	0.5	360
0.2M	105 (7)	5.5 x 10 ⁻⁸	6.5	4.1	2.4 x 10 ⁻⁵	12.0	0.6	160
0.1M	32 (4)	3.5 x 10 ⁻⁷	12.6 ^a	5.8	5.7 x 10 ⁻³	--- ^b	--- ^b	--- ^b
0.1M	65 (8)	1.9 x 10 ⁻⁷	13.7 ^a	5.0	2.0 x 10 ⁻⁶	4.8	0.2	300
Al ₂ O ₃ Solution acac-free 250 °C								
0.4M	71 (2)	7.5 x 10 ⁻⁸	6.0	4.6	7.9 x 10 ⁻¹⁰	0.95	0.4	170
0.27M	42 (2)	1.3 x 10 ⁻⁷	6.2	4.5	1.3 x 10 ⁻⁸	1.1	0.2	130
0.13M	20 (2)	2.4 x 10 ⁻⁷	5.4	3.6	4.8 x 10 ⁻⁷	0.32	0.2	180
Al ₂ O ₃ Solution acac-free 150 °C								
0.4M	86 (2)	1.2 x 10 ⁻⁷	11.3 ^a	3.5	7.8 x 10 ⁻⁶	--- ^c	--- ^c	--- ^c

^a capacitance is not trustworthy because dissipation factor > 0.1

^b dielectric not suitable for TFT operation

^c TFTs not yet fabricated on this dielectric

Since vapor deposition methods do not yield satisfactory dielectrics for TFTs, we investigate solution-processed dielectrics. Solution-deposited Al₂O₃ dielectric properties and transistor parameters of In₂O₃ semiconductor deposited by solution-combustion on Si substrates are summarized in Table 2.1. Fabricating devices on Si allows for efficient screening of different metal oxide recipes and the corresponding film properties, without the added processing of gate and dielectric patterning as well as thermal cycling on the SMP substrate. Suitable candidates are then tested on SMP. The table shows major performance criteria relevant in guiding the selection of a dielectric for TFT fabrication on SMP. Other important criteria are processing temperature and the compatibility of the materials' thermal expansion properties with the SMP substrate.

Performance of capacitors and TFTs fabricated on thermally grown SiO₂ served as a baseline for comparing other candidate dielectric materials and processes. As expected, these devices show low leakage current densities ($\sim 10^{-11}$ to $\sim 10^{-10}$ A/cm² at 2 MV/cm bias) and high breakdown fields (> 7 MV/cm), but also have relatively low areal capacitance due to the thickness of the films (168 – 312 nm) and the low relative permittivity of SiO₂ ($\epsilon_r = 3.9$). Field effect mobility (μ) is calculated from the slope of drain current vs. gate voltage (I_D vs. V_G) in the saturation regime using Equation 1.1. The mobility of the In₂O₃ TFTs made on thermally grown SiO₂ ranges from 0.3 – 0.4 cm²/V*s and SS ranges from 820 – 1020 mV/dec, depending on the dielectric thickness. These results are comparable to previously reported values for solution-processed metal oxide semiconductors on thermally grown SiO₂.¹⁰

Solution-based Al₂O₃ from acac-containing precursor results in films with greater areal capacitance than that of thermally grown SiO₂ because ϵ_r of Al₂O₃ (bulk value 9-11) is higher than that of SiO₂ (bulk value 3.9). However, leakage current density is greatly increased.

The 32-nm film, for example, is too leaky for transistor operation. To increase the dielectric thickness and reduce the leakage, we need to deposit many layers. Transistors on thick Al₂O₃ films deposited in this manner, such as the 105-nm film, exhibit leakage current densities low enough for TFT operation ($\sim 10^{-5}$ A/cm² at 2 MV/cm), although they are 5 orders of magnitude greater than 168-nm thermally grown SiO₂ ($\sim 10^{-10}$ A/cm²). However, TFTs on this dielectric show a greatly improved mobility of 12 cm²/V*s and SS of 160 mV/dec. Transfer characteristics of a TFT fabricated on the 105-nm Al₂O₃ dielectric made from acac-containing solution are shown in Figure 2.2a. Fabricating these films on SMP, however, presents a challenge as they require extra thermal cycling with the large number of coats, which results in cracking in the dielectric film, as shown in Figure 2.3. Achieving a thicker film with fewer coats by using a more concentrated precursor solution also results in cracking in the dielectric, as well as more porous films.¹⁴

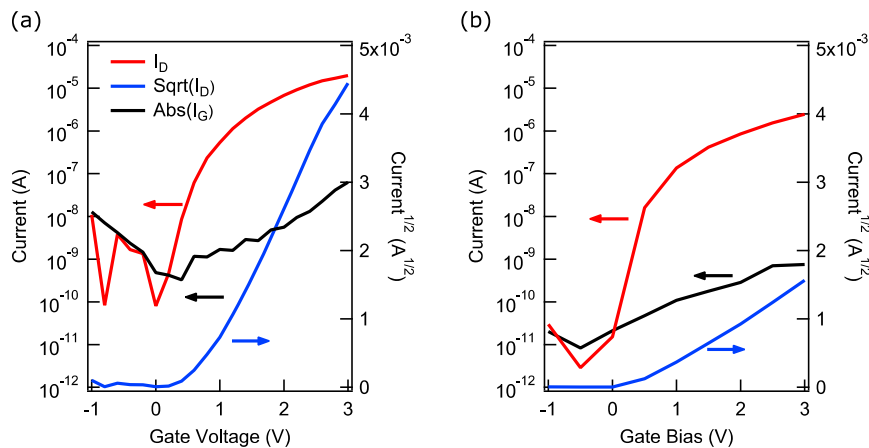


Figure 2.2: Rigid In₂O₃ TFT performance on (a) 105- nm Al₂O₃ deposited by 7 coats of 0.2 M acac-containing solution and (b) 71- nm Al₂O₃ deposited by 2 coats of 0.4 M acac-free solution. Both samples were annealed at 250 °C.

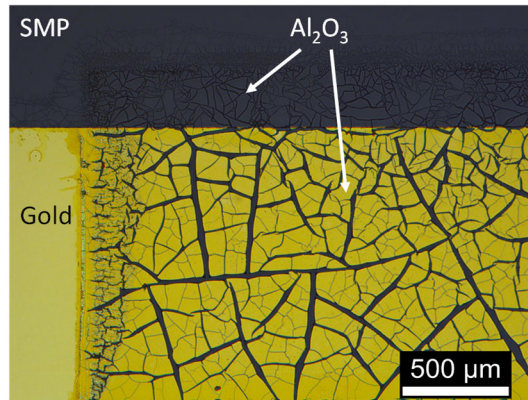


Figure 2.3: SMP with Au gate electrode and 4 coats of 0.2 M Al_2O_3 from acac-containing solution annealed at 250 °C. Extensive cracking of the Al_2O_3 film is clear.

To increase the thickness of Al_2O_3 per coat while also reducing the leakage current density and decreasing the processing temperature to avoid cracking, fabrication of Al_2O_3 films from acac-free solutions is investigated. Hwang et al. have shown that acac-free precursor solutions, which do not involve combustion reactions and do not have organic additives, can produce high-quality (low leakage current) dielectric films. By combining thermal and UV annealing, they demonstrate feasibility at as low as 150 °C.¹⁵ However, we observe that non-uniform film formation after the initial 80 °C anneal frequently occurs with acac-free solutions, possibly due to the multiple boiling points of the solvent (MOE and water) and the lack of the stabilizing effect of acac. By heating the uncapped vial on a hotplate to remove water from the precursor solution, consistent precursor film formation is achieved, resulting in a final metal oxide film free of visible defects. Using this recipe, only two coats of dielectric are necessary to achieve 20 - 71 nm thickness depending on the precursor concentration. It is also found that the initial UV-ozone exposure needs to be increased from 10 min to 45 min to ensure resistance to the developing solution for the exposed parts of the film. Combined with an overnight UV-ozone exposure after thermally annealing, this process produces Al_2O_3 films with greatly improved

leakage current densities. Noteworthy, 71-nm Al₂O₃ films annealed at 250 °C exhibit leakage current densities approaching 10⁻¹⁰ A/cm² at 2 MV/cm, rivaling that of 168 nm thermally grown SiO₂. TFTs on this film exhibit a mobility of 0.95 cm²/V*s and SS of 170 mV/dec. Transfer characteristics of this device are shown in Figure 2.2b. Reducing Al₂O₃ dielectric thickness to 42 nm, mobility increases to 1.1 cm²/V*s and SS decreases to 130 mV/dec, while leakage current density only increases to 10⁻⁸ A/cm². Even the thinnest film (20 nm) made from the acac-free solution has a leakage current density of 10⁻⁷ A/cm², lower than the thickest film from acac-containing precursor (105 nm, 10⁻⁵ A/cm²). Additionally, when the annealing temperature is reduced to 150 °C for these films, leakage current densities are comparable to those on films fabricated from acac-containing solutions annealed at 250 °C (~10⁻⁵ A/cm² for both). However, we note that the index of refraction values obtained from spectroscopic ellipsometry for the acac-free Al₂O₃ films are 1.44 – 1.47, lower than those of the acac-containing films (1.53 – 1.55), and while SS is improved, μ on acac-free films is reduced; more work is needed to understand these differences.

Figure 2.4 shows Al₂O₃ from a 0.2 M acac-free solution on SMP annealed at 150 °C; it is evident that this film is free of cracks. However, these devices resulted in leakage current densities too high for TFT operation, possibly due to degradation of the gate electrode (100 nm Ag / 20 nm Al) by the UV-ozone exposure and diffusion of the gate metal into the dielectric forming shunting pathways. Additionally, extended UV-ozone exposure and elevated temperature results in discoloration (yellowing) of the SMP. Current research efforts are focused on more inert gate metals (Au/Al or Au/Ti) and on determining a lower limit on the UV-ozone

exposure necessary to achieve sufficient dielectric properties for TFT operation. Al or Ti is deposited as a diffusion barrier layer between the Au gate contact and the Al_2O_3 .¹⁶

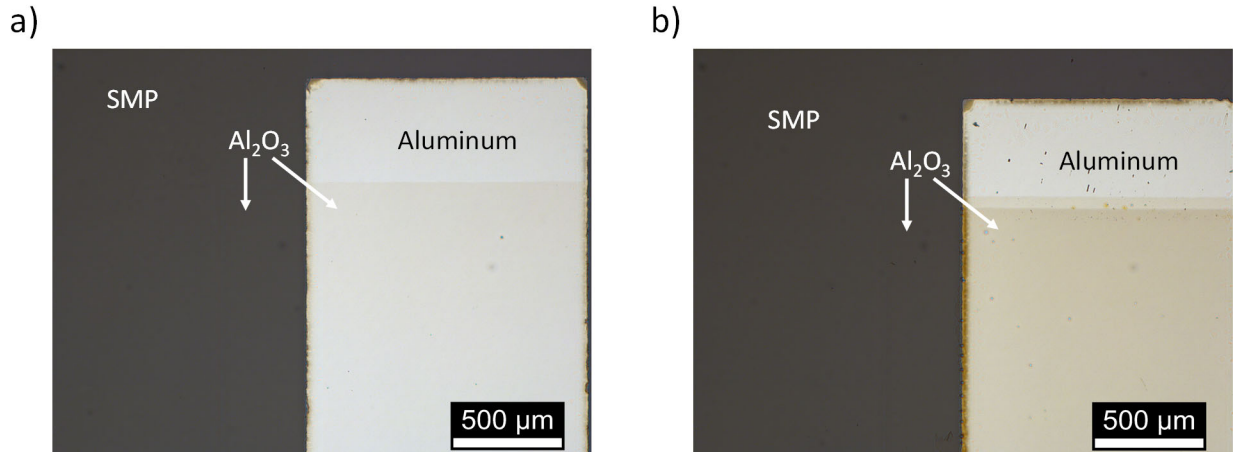


Figure 2.4: SMP with Ag/Al gate electrode (a) 1 coat 0.2 M Al_2O_3 from acac-free solution annealed at 150 °C and (b) 2 coats of Al_2O_3 prior to final UV-ozone exposure.

2.6 Conclusions

By using precursor solutions without a fuel and compensating with extended UV-ozone exposure, Al_2O_3 films spin-coated on Si substrates at 250 °C demonstrate leakage current densities comparable to thermally grown SiO_2 of twice the thickness. These dielectrics, by virtue of their multi-step UV and thermal annealing, can be easily deposited and patterned in conjunction with solution-combustion processed In_2O_3 , and are shown to produce TFTs with μ of $1.1 \text{ cm}^2/\text{V}\cdot\text{s}$, SS as low as 130 mV/dec, and threshold voltages near 0 V. Even when annealed at only 150 °C, the leakage current densities on these films match those on films from acac-containing precursors annealed at 250 °C. Ongoing research efforts are focused on transferring this process to fabricate fully-patterned TFTs on SMP substrates. Further extension of the process beyond the dielectric may lead to a simple method for completely solution-deposited, all-oxide, fully-patterned flexible TFTs.

2.7 References

- (1) Reeder, J.; Kaltenbrunner, M.; Ware, T.; Arreaga-Salas, D.; Avendano-Bolivar, A.; Yokota, T.; Inoue, Y.; Sekino, M.; Voit, W.; Sekitani, T.; et al. Mechanically Adaptive Organic Transistors for Implantable Electronics. *Adv Mater* **2014**, *26* (29), 4967–4973.
- (2) O'Rourke, S.; Loy, D.; Moyer, C.; Bawolek, E.; Ageno, S.; O'Brien, B.; Marrs, M.; Bottesch, D.; Dailey, J.; Naujokaitas, R.; et al. Direct Fabrication of A-Si:H Thin Film Transistor Arrays on Flexible Plastic Film and Metal Foil Substrates: Critical Challenges and Enabling Solutions. *Ecs Transactions* **2008**, *16* (9), 49–54.
- (3) Voit, W.; Ware, T.; Dasari, R. R.; Smith, P.; Danz, L.; Simon, D.; Barlow, S.; Marder, S. R.; Gall, K. High-Strain Shape-Memory Polymers. *Adv Funct Mater* **2010**, *20* (1), 162–171.
- (4) Yu, X.; Marks, T. J.; Facchetti, A. Metal Oxides for Optoelectronic Applications. *Nat Mater* **2016**, *15* (4), 383–396.
- (5) Lorenz, M.; Rao, R.; Venkatesan, T.; Fortunato, E.; Barquinha, P.; Branquinho, R.; Salgueiro, D.; Martins, R.; Carlos, E.; Liu, A.; et al. The 2016 Oxide Electronic Materials and Oxide Interfaces Roadmap. *J Phys D Appl Phys* **2016**, *49* (43), 433001.
- (6) Nag, M.; Bhoolakam, A.; Steudel, S.; Genoe, J.; Groeseneken, G.; Heremans, P. Impact of the Low Temperature Gate Dielectrics on Device Performance and Bias-Stress Stabilities of a-IGZO Thin-Film Transistors. *Ecs J Solid State Sc* **2015**, *4* (8), N99–N102.
- (7) Sazonov, A.; Stryahilev, D.; Nathan, A.; Bogomolova, L. D. Dielectric Performance of Low Temperature Silicon Nitride Films in A-Si:H TFTs. *J Non-cryst Solids* **2002**, *299*, 1360–1364.
- (8) Joshi, P.; Voutsas, A.; Hartzell, J. High Performance Gate Dielectric for Low Temperature TFTs. *Ecs Transactions* **2009**, *19* (9), 35–43.
- (9) Herth, E.; Desré, H.; Algré, E.; Legrand, C.; Lasri, T. Investigation of Optical and Chemical Bond Properties of Hydrogenated Amorphous Silicon Nitride for Optoelectronics Applications. *Microelectron Reliab* **2012**, *52* (1), 141–146.
- (10) Kim, M.-G.; Kanatzidis, M. G.; Facchetti, A.; Marks, T. J. Low-Temperature Fabrication of High-Performance Metal Oxide Thin-Film Electronics via Combustion Processing. *Nat Mater* **2011**, *10* (5), 382.
- (11) Rim, Y.; Chen, H.; Liu, Y.; Bae, S.-H.; Kim, H.; Yang, Y. Direct Light Pattern Integration of Low-Temperature Solution-Processed All-Oxide Flexible Electronics. *Acs Nano* **2014**, *8* (9), 9680–9686.

- (12) Nayak, P. K.; Hedhili, M.; Cha, D.; Alshareef, H. High Performance In 2 O 3 Thin Film Transistors Using Chemically Derived Aluminum Oxide Dielectric. *Appl Phys Lett* **2013**, *103* (3), 033518.
- (13) Branquinho, R.; Salgueiro, D.; Santos, L.; Barquinha, P.; Pereira, L.; Martins, R.; Fortunato, E. Aqueous Combustion Synthesis of Aluminum Oxide Thin Films and Application as Gate Dielectric in GZTO Solution-Based TFTs. *Acs Appl Mater Inter* **2014**, *6* (22), 19592–19599.
- (14) Yu, X.; Smith, J.; Zhou, N.; Zeng, L.; Guo, P.; Xia, Y.; Alvarez, A.; Aghion, S.; Lin, H.; Yu, J.; et al. Spray-Combustion Synthesis: Efficient Solution Route to High-Performance Oxide Transistors. *Proc National Acad Sci* **2015**, *112* (11), 3217–3222.
- (15) Hwang, J.; Lee, K.; Jeong, Y.; Lee, Y.; Pearson, C.; Petty, M. C.; Kim, H. UV-Assisted Low Temperature Oxide Dielectric Films for TFT Applications. *Adv Mater Interfaces* **2014**, *1* (8), 1400206.
- (16) Yip, G.; Qiu, J.; Ng, W.; Lu, Z. Effect of Metal Contacts on the Electrical Characteristics of Al₂O₃ Dielectric Thin Films. *Appl Phys Lett* **2008**, *92* (12), 122911.

CHAPTER 3

SOLUTION-PROCESSED OXIDE THIN FILM TRANSISTORS ON SHAPE MEMORY POLYMER ENABLED BY PHOTOCHEMICAL SELF-PATTERNING

Authors – Trey B. Daunis,^a Diego Barrera,^a Gerardo Gutierrez-Heredia,^{a,d} Ovidio Rodriguez-Lopez,^{b,c} Jian Wang,^a Walter E. Voit,^{a,b,c} and Julia W. P. Hsu^a

^aDepartment of Materials Science and Engineering, RL 10

^bDepartment of Electrical and Computer Engineering, EC 33

^cDepartment of Bioengineering, BSB 11

The University of Texas at Dallas

800 West Campbell Road

Richardson, Texas 75080-3021

^dCentro de Investigaciones en Optica

Lomas del Bosque 115, Lomas del Campestre

37150 León, Gto., México

Reprinted with permission from Daunis, T. B.; Barrera, D.; Gutierrez-Heredia, G.; Rodriguez-Lopez, O.; Wang, J.; Voit, W. E.; Hsu, J. W. P. Solution-Processed Oxide Thin Film Transistors on Shape Memory Polymer Enabled by Photochemical Self-Patterning. *J. Mater. Res.* **2018**, *33* (17), 2454-2462. Copyright 2018 Materials Research Society.

3.1 Preface

This chapter presents the conclusion of my first research project – the solution-deposition of oxide thin film transistors (TFTs) on shape memory polymer (SMP) substrates. The processes developed in Chapter 2 for UV-assisted curing and patterning of In_2O_3 on Si for rigid TFTs and of Al_2O_3 on SMP for flexible capacitors were combined to fabricate oxide TFTs on SMP with an Al_2O_3 gate dielectric and an In_2O_3 semiconductor channel. The effect of UV exposure on the curing and patterning processes was examined in detail, and the properties of the oxide films and devices were characterized extensively. The identification of certain features of the oxide dielectric and how they affect the TFT performance served as motivation for the next project, described in Chapter 4.

My contributions were fabricating devices, characterizing film properties, measuring and analyzing the devices, and preparing the manuscript. Dr. Diego Barrera contributed XPS measurements and analysis. Dr. Gerardo Gutierrez-Heredia assisted with electrical characterization and analysis. Ovidio Rodriguez-Lopez assisted with SMP device fabrication. Dr. Jian Wang helped with metal oxide sol-gel technique and thin film analysis. Prof. Walter E. Voit provided expertise on the SMP substrate. Prof. Julia W. P. Hsu provided valuable guidance on all aspects of the project and assistance with manuscript preparation.

3.2 Abstract

Solution-processed metal oxide electronics on flexible substrates can enable applications from military to health care. Due to limited thermal budgets and mismatched coefficients of thermal expansion between oxides and substrates, achieving good performance in solution-

processed oxide films remains a challenge. Additionally, the use of traditional photolithographic processes is incompatible with low-cost, high-throughput roll-to-roll processing. Here we demonstrate solution-deposited oxide thin film transistors (TFTs) on a shape memory polymer substrate, which offers unique control of final device shape and modulus. The key enabling step is the exposure of the precursor film to UV-ozone through a shadow mask to perform patterning and photochemical conversion simultaneously. These TFTs have mobility up to $160 \text{ cm}^2 \cdot \text{V}^{-1} \cdot \text{s}^{-1}$, subthreshold swing as low as 110 mV dec^{-1} , and threshold voltage between -2 V and 0 V , while maintaining compatibility with a flexible form factor at processing temperatures below $250 \text{ }^\circ\text{C}$.

3.3 Introduction

Flexible substrates for electronic devices enable applications that require large area or non-planar form factors, for example wearable medical devices,¹ curved displays,² sensors molded in automobile bodies, or imagers on missiles' nosecones. When used as a flexible substrate, not only do shape memory polymers (SMPs) provide mechanical flexibility to an electronic device, they have the unique capability to return to their original as-fabricated shape upon the application of an external thermal stimulus.³ These properties allow for the fabrication of implantable medical devices, such as neural interfaces,⁴ that are rigid and planar during room-temperature processing, yet can conform to body tissue's three-dimensional shape and mechanical softness upon implantation.⁵ Thermoset thiol-ene/acrylate SMPs can withstand higher processing temperatures, above $250 \text{ }^\circ\text{C}$,⁶ than many conventional polymer substrates such as polyethylene terephthalate (PET, maximum of $150 \text{ }^\circ\text{C}$),⁷ yet have better transparency than high temperature polyimide substrates.² Their low residual strain upon thermal cycling allows thermoset SMP substrates to retain their original dimensions after each thermal cycle,⁸ which is beneficial for

processing of large-area circuitry where precise alignment of patterned features across large lateral distances is required. Vacuum deposited metal oxide thin film transistors (TFTs) patterned and annealed by traditional methods have been demonstrated on these substrates.⁶ To take full advantage of low cost, large area, and high throughput manufacturing on these substrates, it is necessary to further develop non-vacuum, solution-based oxide thin films that are compatible with roll-to-roll processing. These films must also demonstrate electronic properties comparable to those achieved by conventional vacuum-based processes. This work demonstrates the first example of low-temperature solution-processing of oxide TFTs on SMP substrates, which achieve excellent performance.

The first challenge to overcome is the incompatibility of traditional thermal processing of solution-deposited oxide films with the thermal budget of the polymer substrates. Conventional solution deposition methods such as sol-gel processing typically require high calcination temperatures (~ 400 °C for amorphous alumina)^{9–12} to complete the conversion of precursor films to metal oxides. These temperatures are much higher than the degradation temperatures even for the most temperature-tolerant polymers such as polyarylate (325 °C) and polyimide (350 °C).² Recent research efforts aiming to reduce the required annealing temperature generally fall into two categories: (1) Solution combustion synthesis incorporates a fuel (such as urea or acetylacetone) and an oxidizer (NO_3^-) into the precursor solution, providing chemical energy to the precursor film and lowering the external temperature required for oxide formation;^{12–14} or (2) Exposure to a UV lamp^{15–17} or laser,¹⁸ or annealing in the presence of a microwave field¹⁹ provides energy from electromagnetic waves, rather than thermal energy, to help overcome the

oxide formation barrier. With these methods, oxide electronic devices have been successfully made on polymer substrates.^{16,20,21}

Even with oxide processing temperatures below the degradation temperature of the polymer substrate, the mechanical property mismatch between oxides and polymers presents an additional challenge. When unpatterned sol-gel films are annealed on polymer substrates, the difference between the large coefficient of thermal expansion (CTE) of the substrate²² and that of the oxide results in extensive cracking of the oxide film.²³ Common polymer substrates, such as PET, have a CTE of 15 ppm/°C.⁷ Using a CTE value of 5 ppm/°C for oxides, the strain mismatch upon heating from 25 °C to 250 °C is 0.2%. The strain mismatch added to the brittle nature of oxide materials leads to extensive cracking when annealing large-area solution-deposited oxide films on polymer substrates. This issue does not occur in vacuum deposition of films because the films are deposited at room or low temperature and patterned by conventional photolithography—depositing photoresist, soft baking, UV patterning, developing, etching, and removing photoresist—to small areas before post-annealing (activating) at higher temperature. Because stress is released at the edges of the patterned features, cracks are not observed in patterned vacuum-deposited oxide films on SMP.⁶ Thus, it is desirable to pattern the sol-gel precursor films prior to annealing to form oxides. This becomes an issue for solution-deposited films since precursor films are readily soluble in many common solvents and are easily attacked by acidic and basic solutions, making it impossible to pattern these films by conventional photolithographic techniques. Additive printing techniques such as ink-jet printing can accomplish patterned precursor film deposition,²⁴ but suffer from throughput limitations due to the serial nature of the deposition. The ability to pattern combustion precursor oxide films by

exposure to a UV light source through a shadow mask has been previously demonstrated.²⁵ By modifying this method, we successfully overcome the challenges of fabricating TFTs using a solution process on SMP substrates for the first time by patterning different metal oxide precursor films at room temperature and subsequently annealing at higher temperatures to form oxide dielectric and semiconductor films.

3.4 Experimental Details

3.4.1 SMP Substrate Fabrication and Characterization

To make 50 μm thick thermoset thiol-ene/acrylate SMP films, tricyclodecane dimethanol diacrylate (TCMDA), 1,3,5-triallyl-1,3,5-triazine-2,4,6(1H,3H,5H)-trione (TATATO), and 2,2-dimethoxy-2-phenyl acetophenone (DMPA) are purchased from Sigma-Aldrich and Tris[2-(3-mercaptopropionyloxy)ethyl] isocyanurate (TMICN) is purchased from Wako Chemicals. 0.015 g of DMPA is first mixed with 3.58 g of TATATO, followed by the sequential addition and mixing of 3.92 g TCMDA and 7.53 g TMICN. The solution is spin coated onto a substrate at 700 rpm for 60 seconds. The film is then cured under 254 nm UV illumination for 2 minutes followed by 365 nm UV for 60 minutes. The substrate is ready to use after being placed in a vacuum oven at 70 $^{\circ}\text{C}$ overnight. The optical transmission spectrum of SMP is shown in Figure 3.1 for a 50 μm film deposited on glass. The photograph inset in Figure 3.1 shows that SMP is colorless and has > 97% transmission between 400 nm and 800 nm. For fabricating TFTs, SMP films are deposited on Si substrates, which provide good thermal conduction to the oxide layers when annealing on a hotplate. A SiO_2/SiN (20 nm SiO_2 , 800 nm SiN) layer is deposited on SMP substrates by plasma-enhanced chemical vapor deposition at 225 $^{\circ}\text{C}$ prior to device fabrication.

This layer serves to promote adhesion of the solution-deposited metal oxides to the substrates, as well as to act as a buffer layer to absorb the thermal stress due to CTE mismatch between oxide films and polymer substrates. A 0.005” thick invar mask is placed on top of the sample to define the bottom contacts. A magnet beneath the sample holds the mask in place and 100 nm of Al are deposited by thermal evaporation.

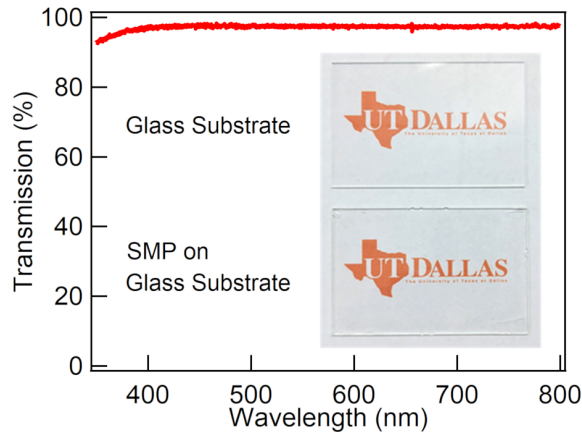


Figure 3.1: Transmission spectrum of a 50 μm SMP substrate on a glass slide. Transmission is 97% from 400 to 800 nm. Inset: Photographs of blank glass slide (top) and glass slide with SMP (bottom).

3.4.2 TFT Fabrication

To make oxide films, all chemicals are purchased from Alfa Aesar, and used as received. Al_2O_3 precursor solution is prepared by dissolving $\text{Al}(\text{NO}_3)_3 \cdot 9(\text{H}_2\text{O})$ in 2-methoxyethanol (MOE) to form a 0.4 M solution. The solution is stirred in an uncapped vial on a hotplate at 110 °C overnight to evaporate most of the excess water introduced with the metal nitrate. Fresh MOE is added to the solution to make up the lost volume, and the solution is stirred for another 20 minutes before being filtered through a 0.2 μm filter. To form a patterned film, the precursor solution is first spin coated onto the SMP substrate with a patterned Al gate at 3,000 rpm for

30 seconds as shown in step 1 of Figure 3.2a. The sample is then placed on a hotplate at 80 °C for 2 minutes to dry the film. In step 2, an invar mask is held in place by a magnet to define the gate dielectric pattern, and the film is exposed to UV-ozone (UVO, Bioforce Nanosciences Procleaner Plus) through the mask at room temperature for 40 minutes. To remove the undeveloped portions, the film is rinsed in a developing solution of acetic acid (1 mL) and DI water (5 mL) in methanol (15 mL) for 10 seconds and immediately rinsed in DI water and dried by a N₂ stream (step 3). Steps 1-3 are then repeated to ensure a pinhole free film of the desired thickness (80 nm). In step 4, the sample is placed on a hotplate at 80 °C and the hotplate temperature is increased at a rate of 10 °C min⁻¹ until the surface of the sample reaches 250 °C as measured by a thermocouple. This temperature is held for 20 minutes and the hotplate is turned off and the sample allowed to cool to room temperature. Figure 3.2b shows optical images after each of the steps during the deposition of two coats of Al₂O₃ gate dielectric on top of an Al gate, resulting in a crack-free patterned oxide film on an SMP substrate.

In₂O₃ is deposited by a similar procedure (Figure 3.2a) using a 0.1 M concentration of In(NO₃)₃ · 3(H₂O) in MOE and the addition of 0.1 M acetylacetone (acac) and 0.1 M ammonium. The solution is stirred overnight at room temperature before use. Since the In₂O₃ precursor contains combustion fuel, we found that a UVO exposure of 10 minutes is sufficient to form a pattern that can withstand the developing solution. The final annealing temperature is varied between 150 °C and 250 °C. The total In₂O₃ film thickness is 13-15 nm depending on the final annealing temperature.

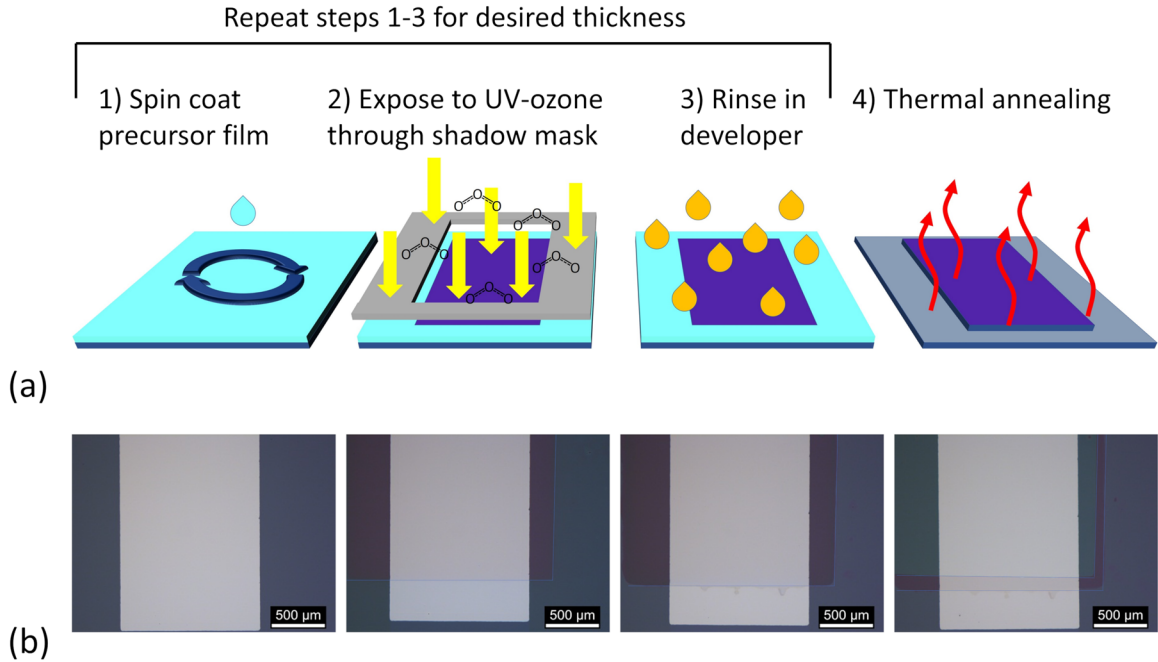


Figure 3.2: Photochemical self-patterning of oxide films from sol-gel precursors. Blanket deposition (step 1), photopatterning (steps 2 and 3), and annealing (step 4) of sol-gel precursor films. (a) Schematic of the process for forming patterned oxide films. (b) Optical images of the film after corresponding processing step in (a). Thin dashed lines are drawn to show boundaries of patterned oxide feature.

After deposition and annealing of Al_2O_3 and In_2O_3 , metal-insulator-metal (MIM) capacitors and TFT devices are completed by defining a $400 \times 400 \mu\text{m}$ top contact or source-drain contacts with a $100 \times 1000 \mu\text{m}$ channel, respectively, by thermal evaporation of 100 nm Al through a shadow mask.

3.4.3 Materials and Device Characterization

Oxide layer thicknesses are determined by ellipsometry of films deposited on Si measured from 280 to 1690 nm at 55° , 65° , and 75° (J. A. Woollam M2000DI) and fit using a B-spline model. X-ray diffraction (XRD) spectra are taken at grazing incident angle (0.5°) using a Rigaku Ultima III diffractometer with Cu K α radiation ($\lambda = 1.5418 \text{ \AA}$) at an operating voltage/current of

40 kV/44 mA. Atomic force microscopy (AFM) is performed in tapping mode (Asylum Research MFP-3D). UV-vis spectrometry (Ocean Optics USB 4000) is measured from 178 nm to 890 nm. SMP absorption is referenced to the bare glass substrates. Metal-oxide precursor solutions are diluted by 1000x and the absorption is referenced to pure 2-MOE in a quartz cuvette with a 1 cm path length. X-ray photoelectron spectroscopy (XPS) are performed on Ulvac-PHI VersaProbe2 with a monochromated Al Ka source (1486.8 eV) at an angle of 45° to the sample surface with an energy step of 0.2 eV and a pass energy of 23.5 eV. XPS data are analyzed using a commercial software (MultiPak, Ulvac-PHI). Fourier transformed infrared (FTIR) spectra are measured using a Nicolet iS50 FT-IR from 450 cm⁻¹ to 6000 cm⁻¹ under N₂ purge.

Electrical measurements are performed in air in a Cascade Microtech probestation. Capacitance vs. frequency is measured at a DC bias of 0V and AC bias of 50 mV from 20 Hz to 300 kHz on an Agilent 4284A Precision LCR Meter. The capacitor area is defined by the top contact at 0.0016 cm². Transfer and output curves of the TFTs are measured on a Keithley 4200 Semiconductor Characterization System.

3.5 Results and Discussion

3.5.1 Chemical Studies of Photochemical Processing

To better understand the photochemical patterning and thermal annealing in the oxide conversion, film thickness and XPS spectra of the O1s binding energy for In₂O₃ (Figure 3.3) and Al₂O₃ (Figure 3.4) are measured at several stages during the film formation process. The O1s signal in the XPS spectrum can be deconvoluted into two peaks, one at 530.0 eV which is

attributed to oxygen in the metal oxide lattice (M-O-M) and one at 531.6 eV which is attributed to oxygen in hydroxide species (-OH).^{15,20,26} The M-O-M peak in Figure 3.3a is minimal for a dried In₂O₃ precursor film, 2% of the total O1s signal (Figure 3.3b). For dried Al₂O₃ precursor film, the M-O-M component is 1% of the total O1s signal (Figures 3.4a and 3.4b). Nearly all the oxygen signal at this stage of processing is from the -OH species. After UVO exposure, the M-O-M peak dramatically increases by 8-fold to 16% of the O1s signal for In₂O₃ and by 12-fold to 12% for Al₂O₃. Due to the M-O-M network formation, a decrease in solubility of the film in a weakly acidic solution ensues, allowing for development of the film pattern (ellipsometry shows no thickness change with rinsing in developing solution). UVO exposure also reduces the thickness of the films by about 50%, from 28 nm for the In₂O₃ precursor film to 13 nm after UVO (Figure 3.3c), and from 142 nm for the Al₂O₃ precursor film to 78 nm after UVO (Figure 3.4c). The thickness reduction is attributed to both the decomposition of metal nitrates and removal of residual solvent, leading to the densification of the film with increasing M-O-M bonding. Subsequent thermal annealing of UVO exposed regions further increases the M-O-M peak as the metal-oxygen network continues to form. The M-O-M signal increases to 41% of the total O1s signal for In₂O₃ films annealed at 175 °C, to 44% for those annealed at 250 °C (Figure 3.3b), and to 48% for Al₂O₃ films annealed at 250 °C (Figure 3.4b). Correspondingly, the oxide film thickness decreases to 7.3 nm at 175 °C and to 6.6 nm at 250 °C for In₂O₃ (Figure 3.3c), and to 44 nm for Al₂O₃ films annealed at 250 °C (Figure 3.4c), as the films densify at the higher annealing temperatures. Note that the XPS and ellipsometry studies used one coat of sol-gel films; hence the thicknesses are half of the films used in the devices below. AFM (Figure 3.5a)

and XRD (Figure 3.5b) measurements of films annealed at 250 °C show that the oxide films remain amorphous with a smooth surface.

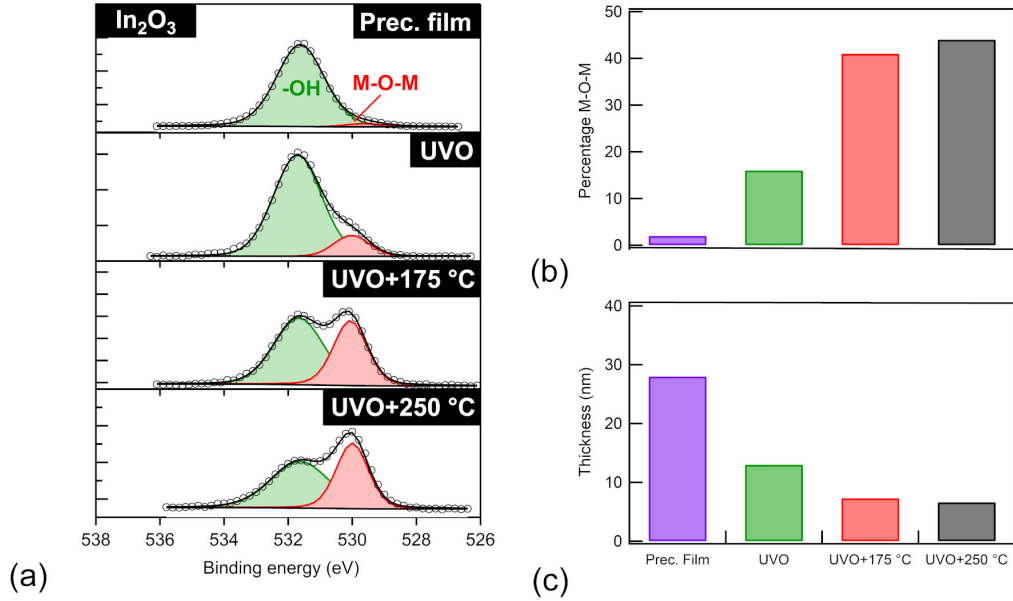


Figure 3.3: XPS and ellipsometry of In₂O₃ films during processing. (a) O1s spectra with deconvoluted metal oxide lattice (M-O-M) peaks and hydroxide (-OH) peaks for the dried In₂O₃ precursor film, In₂O₃ precursor film exposed to UVO for 10 min, and UVO-exposed In₂O₃ film then annealed at 175 and 250 °C. (b) Bar graphs showing the (M-O-M) peak contribution and (c) thickness from ellipsometry at specified processing stage.

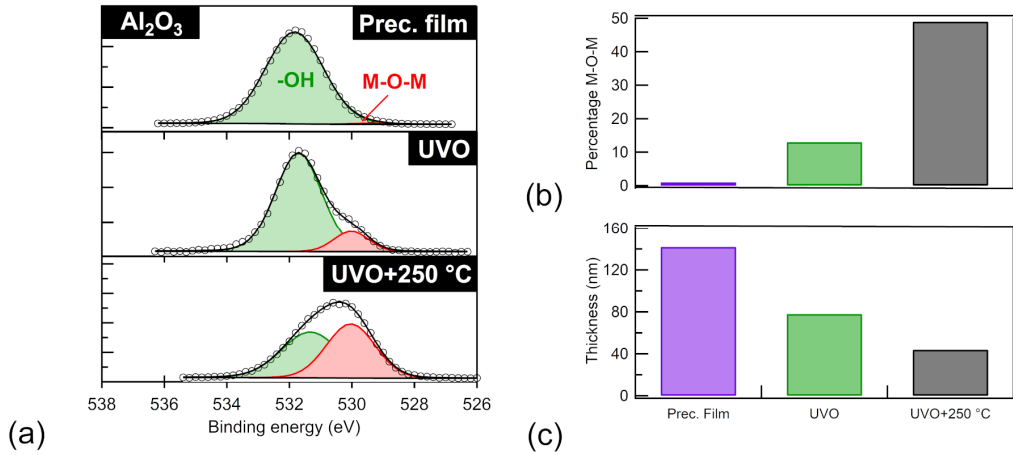


Figure 3.4: (a) XPS O1s spectra of the dried Al₂O₃ precursor, Al₂O₃ film exposed to UVO for 40 min, and exposed Al₂O₃ film annealed at 250 °C showing deconvoluted M-O-M and -OH peaks. (b) Percentage of XPS O1s signal from M-O-M peak. (c) Ellipsometry thickness of the film at each processing stage.

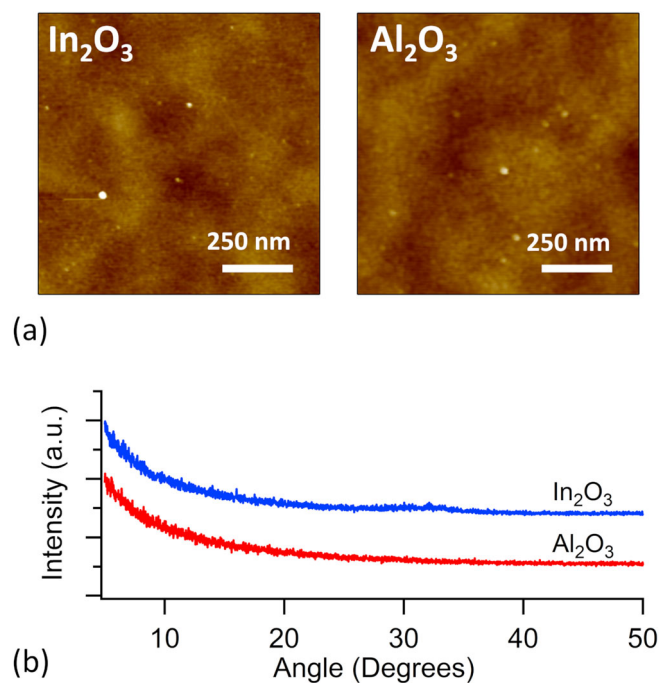


Figure 3.5: (a) Tapping mode AFM images of In_2O_3 (left) and Al_2O_3 (right) films from the transistor device annealed at 250°C showing low surface roughness: rms roughness for In_2O_3 is 0.40 nm and for Al_2O_3 is 0.42 nm . The scale bars represent 250 nm and the full color scale represents 10 nm height variation. (b) Grazing angle XRD spectra for In_2O_3 (top) and Al_2O_3 (bottom) films annealed at 250°C showing an amorphous film structure.

During the UVO exposure, in addition to the conversion of M-O-M network and densification of the film, nitrates from the metal precursors are removed. Figure 3.6a shows a map of the N1s signal intensity at 406.5 eV (NO_3^-)^{27,28} performed on an In_2O_3 precursor film exposed to UVO through a shadow mask. Nitrates remain in the unexposed portion of the film outside of the circular pattern (top spectrum) and are removed from the exposed portion (bottom spectrum). The loss of nitrates observed in XPS is also corroborated by FTIR spectroscopy in the N-O vibration region before and after UVO exposure (Figure 3.6b). It is evident that nitrate is decomposed in both In_2O_3 and Al_2O_3 precursor films and the oxide conversion has begun. This is consistent with a reaction mechanism where nitrate ions absorb UV light, decompose, and produce oxygen and nitrogen dioxide radicals that assist in the M-O-M bond formation.²⁹

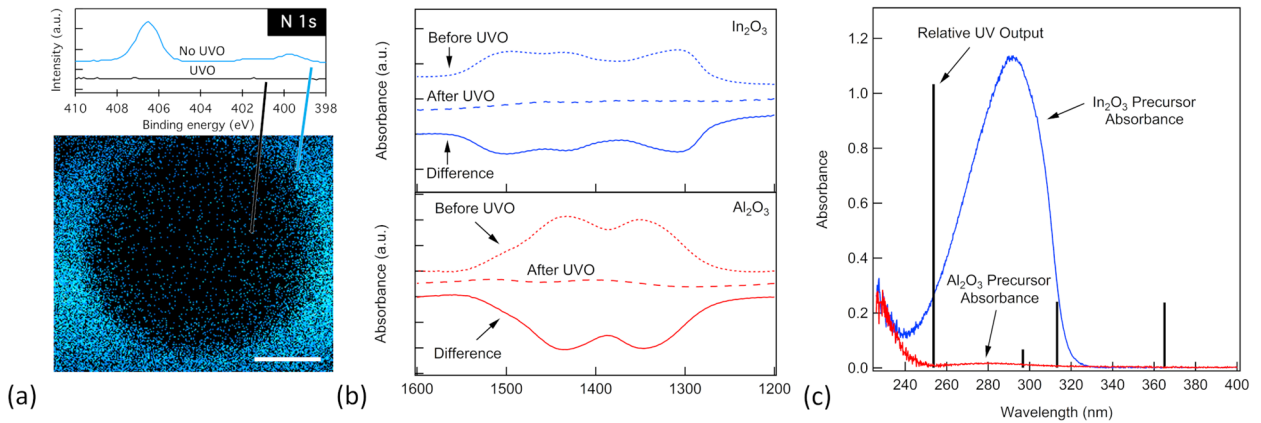


Figure 3.6: (a) XPS map of N1s signal intensity surrounding a single 600 μm diameter UVO exposed circle on an In_2O_3 film. Scale bar is 200 μm . Top: N1s spectra for the unexposed precursor area (blue, top) and UVO exposed area (black, bottom). (b) N–O vibration region of FTIR spectra before and after UVO annealing for (top) an In_2O_3 film and (bottom) an Al_2O_3 film. The loss of absorbance from 1250 to 1550 cm^{-1} in the differential spectrum indicates the removal of nitrates from the film. (c) UV-vis of In_2O_3 (blue) and Al_2O_3 (red) precursor solutions. Vertical bars represent the normalized output of the Hg vapor UV lamp.

As stated in section 3.4.2, In_2O_3 precursor includes a fuel (acac) but Al_2O_3 precursor does not. This is because of the larger thickness required for the Al_2O_3 dielectrics. Using the combustion synthesis precursor formulation, thin (< 20 nm) In_2O_3 semiconductor films can be formed with high quality by depositing and patterning two coats of precursors (Figure 3.2a) followed by a single thermal annealing step (175-250 $^\circ\text{C}$). However, for thicker films, the inclusion of a fuel results in high porosity due to the release of gaseous combustion byproducts during annealing.³⁰ For the Al_2O_3 dielectric layer, which needs to be thick (~ 80 nm) to ensure low gate leakage current for TFT operation, it would be necessary to deposit as many as 8 or more coats and to anneal after every 1 to 2 coats if a combustion precursor formulation were used.²⁵ To minimize the laborious processing, acac is not added to the precursor for the Al_2O_3 dielectric, allowing for thicker films of ~ 40 nm per coat to be deposited twice, followed by a single annealing step at 250 $^\circ\text{C}$.²³ From XPS and FTIR results shown above, a similar extent of

M-O-M bond formation and nitrate removal can be achieved, except that the Al₂O₃ films not containing acac require four times longer UVO exposure than that required for In₂O₃ films with acac. The absorption spectra of the precursor solutions (Figure 3.6c) show that while both nitrate and acac absorb in the UV, the latter increases the absorption at 253.7 nm, the dominant wavelength of the mercury-vapor lamp, by a factor of 26. Additionally, the strong absorption peak seen at shorter wavelengths in Figure 3.6c (< 240 nm) for both In₂O₃ and Al₂O₃ precursors is attributed to nitrate ions and likely continues to increase at wavelengths below the detection capabilities of the UV-vis measurement. The additional output by the Hg lamp at 184 nm (not shown) is expected to be absorbed by nitrates in both precursors.²⁹ Hence, acac is not necessary for M-O-M bond formation (Figures 3.3 and 3.4), although it accelerates the conversion reaction by increasing UV absorption.²⁵ Very recently, similar UV patterning of sol-gel precursor films was demonstrated on rigid substrates using specially synthesized compounds as both metal oxide precursors and UV absorbers.³¹ Here we show that direct photochemical patterning on flexible substrates can be effectively performed using commercially available chemicals.

3.5.2 Device Characteristics

MIM capacitors and TFTs are fabricated using the above method to form patterned Al₂O₃ dielectric and In₂O₃ semiconductor films. TFT device structure is shown in Figure 3.7a. Field effect mobility, μ_{FE} , is extracted from transfer curves (drain current (I_D) vs. gate voltage (V_G)) (Figure 3.7b) in the saturation regime with drain voltage (V_D) = 3V (Figure 3.7c) using Equation 1.1. The derivative $d\sqrt{I_D}/dV_G$ is taken as the slope of the linear portion of the $I_D^{1/2}$ vs. V_G curve (shown as a dashed green line in Figure 3.7b), channel length and width are defined by the top

contacts as 100 μm and 1000 μm , respectively, and C is the areal capacitance of the dielectric measured on an MIM structure (Figure 3.8b). From the transfer curve of a single device annealed at 250 $^{\circ}\text{C}$ shown in Figure 3.7b, we find $\mu_{\text{FE}} = 138 \text{ cm}^2 \cdot \text{V}^{-1} \cdot \text{s}^{-1}$ (using C measured at 10 kHz) with an on/off current ratio ($I_{\text{on/off}}$) above 10^4 and subthreshold swing (SS) of 240 mV dec^{-1} . This mobility value is high, but it is comparable to previously reported metal oxide semiconductors (including In_2O_3 and In-Ga-Zn oxide) on solution processed Al_2O_3 gate dielectrics.^{25,32–35} Below, we consider two factors that could over-estimate the saturation mobility using Equation 1.1 and a full discussion of the origin of the high mobility is presented in Chapter 4.

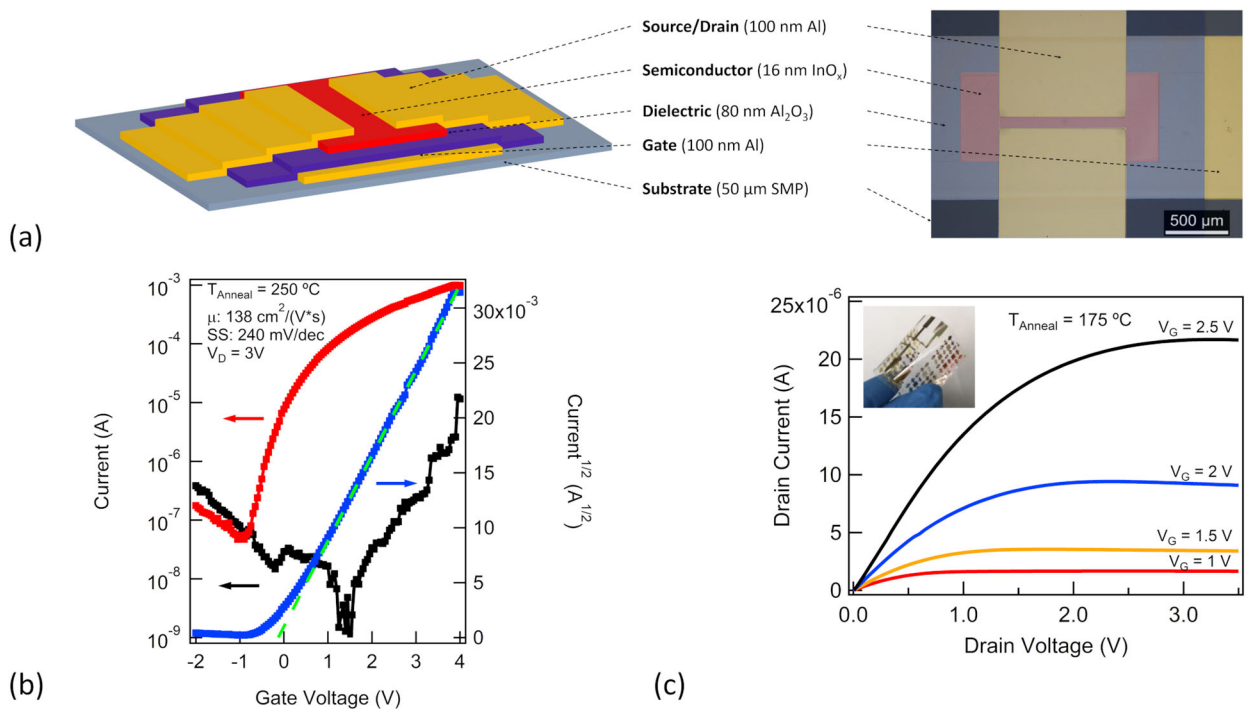


Figure 3.7: TFT on SMP device structure and performance. (a) Schematic and optical image (false color added for emphasis) of device structure with SMP substrate, aluminum gate, Al_2O_3 gate dielectric, In_2O_3 semiconductor, and Al source and drain. (b) Transfer curve with drain current (I_D , red), gate current, (I_G , black), and $I_D^{1/2}$ (blue) vs. gate voltage (V_G) for a TFT with In_2O_3 annealed at 250 $^{\circ}\text{C}$ and $V_D = 3 \text{ V}$. Green dashed line shows $I_D^{1/2}$ vs. V_G fit used for mobility extraction. (c) Output curves showing drain current (I_D) vs. drain voltage (V_D) for a device with In_2O_3 annealed at 175 $^{\circ}\text{C}$. Inset: Photograph of transistors and capacitors on SMP delaminated from the carrier substrate.

The effect of In_2O_3 processing temperature on TFT operation (Figure 3.8a) and on MIM ($\text{Al}/\text{Al}_2\text{O}_3/\text{Al}$) capacitance-frequency (C-f) behavior (Figure 3.8b) is examined. While transistors with In_2O_3 annealed at 150°C do not present channel modulation, those annealed at 175°C show an average mobility of $4\text{ cm}^2\cdot\text{V}^{-1}\cdot\text{s}^{-1}$ increasing to an average of $160\text{ cm}^2\cdot\text{V}^{-1}\cdot\text{s}^{-1}$ for those annealed at 250°C . These mobility values are calculated using C measured at 10 kHz (Table 3.1). $I_{\text{on/off}}$ ranges from $\sim 10^4$ to $\sim 10^5$. It is important to note that there is significant frequency dispersion evident in the capacitance measurements indicating polarizable defects (such as $-\text{OH}$) or mobile ions in the dielectric. Because these defects only respond to lower frequency electric fields, the apparent capacitance of the dielectric is higher at low frequency.

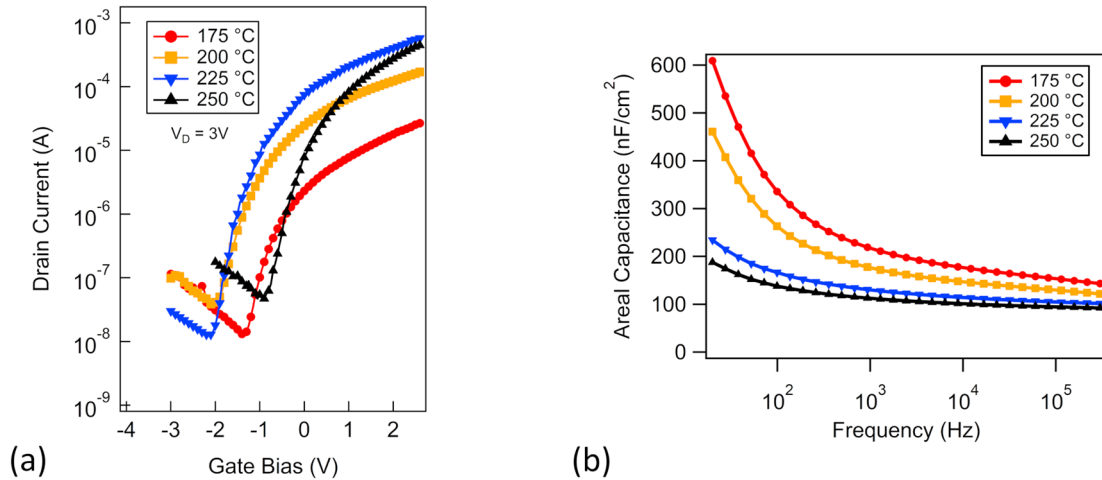


Figure 3.8: Device performance for varying annealing temperatures of In_2O_3 . (a) I_D vs. V_G curves for representative devices annealed from 175 to 250°C taken at $V_D = 3\text{ V}$. (b) Areal capacitance vs. frequency measurements from 20 Hz to 300 MHz of $\text{Al} / \text{Al}_2\text{O}_3 / \text{Al}$ MIMs for different In_2O_3 annealing temperatures.

As TFT measurements are taken under quasi-static conditions, this results in an over estimation of the channel mobility by under estimation of the gate capacitance. For this reason, mobility values using the capacitance measured at 20 Hz are also shown in Table 3.1. Although all gate dielectrics are annealed at 250°C prior to semiconductor deposition, the frequency

dispersion in the capacitance is still less in devices with a higher final semiconductor annealing temperature. Furthermore, the capacitance values at 10 kHz correspond to relative permittivity $\epsilon_r = 9.1$ to 15.7 as In_2O_3 processing temperature decreases. The higher-than-bulk permittivity values are attributed to the $-\text{OH}$ content of the dielectric.³⁴ Since the capacitors are constructed on the same devices as the TFTs and undergo all the same processing conditions, the dielectric annealed at a lower temperature contains a larger amount of $-\text{OH}$, hence higher ϵ_r and larger capacitance-frequency dispersion. Note that when Nayak et. al. reported a mobility value of $127 \text{ cm}^2 \cdot \text{V}^{-1} \cdot \text{s}^{-1}$ for a solution processed In_2O_3 TFT on Al_2O_3 dielectric, they used a capacitance value measured at 1 MHz to calculate the mobility. They also observed $-\text{OH}$ in the XPS O1s spectra of Al_2O_3 similar to Figure 3.4a.³²

Table 3.1: The average channel mobility for TFTs with In_2O_3 annealed at different temperatures. Mobility is calculated using gate capacitance measured at both 10 kHz and 20 Hz.

T_{Anneal} (°C)	C/A at 10 kHz (nF/cm ²)	Mobility [cm ² (V·s)]	C/A at 20 Hz (nF/cm ²)	Mobility [cm ² (V·s)]
175	178	4.2 ± 2.3	609	1.2 ± 0.6
200	147	24 ± 1	461	7.7 ± 0.4
225	114	69 ± 13	234	34 ± 6
250	101	160 ± 30	188	86 ± 18

Additionally, the mobility is over estimated because of the fringe current when the channel is in the on-state. Because the patterned semiconductor is 50% wider than the channel as defined by the source and drain contacts (Figure 3.7a), the mobility may be overestimated by up to 50%. Even after taking these considerations into account, the mobility value for the TFT made at 250 °C remains quite high at $57 \text{ cm}^2 \cdot \text{V}^{-1} \cdot \text{s}^{-1}$, but is in line with a number of other reports on

solution-processed Al₂O₃ dielectric.³⁶ Additional mechanisms for the high channel mobility values reported here and in the literature are the subject of Chapter 4.

3.6 Conclusions

We demonstrate that photochemical self-patterning of sol-gel precursor films prior to annealing enables high-performance metal oxide TFTs on an SMP substrate by solution processing. Exposure to UVO through a shadow mask defines patterns in the precursor films. Chemical and thickness analyses reveal that UVO exposure initiates the metal oxide conversion process by decomposing the metal precursors and facilitating the formation and densification of metal-oxide networks. Subsequent thermal annealing at elevated temperatures produces high-quality oxide film patterns on SMP substrate without cracks. TFTs on SMP using Al₂O₃ gate dielectric and In₂O₃ semiconductor fabricated by this method demonstrate excellent device performance, with mobility up to 160 cm²·V⁻¹·s⁻¹, subthreshold swing as low as below 110 mV dec⁻¹, and threshold voltage near 0V using processing temperatures ≤ 250 °C. Further research on UVO patterning and conversion of solution-processed metal oxide films as it relates to electrical device performance and stability will advance large-scale processing of high-performing devices on SMP and other low-temperature substrates.

3.7 Acknowledgments

The authors thank Dr. Robert Wallace for the use of the spectroscopic ellipsometer, Michael Womble for assistance in XRD measurements, and Sean Dillon and James Tran for help in FTIR measurements. This work is supported in part by the Center for Engineering Innovation and by SPARC. W.V. acknowledges support from the DARPA Young Faculty Award and DARPA

Director's Fellowship (No. D13AP00049). J.W.P.H. acknowledges support from the Texas Instruments Distinguished Chair in Nanoelectronics.

3.8 References

- (1) Khan, Y.; Ostfeld, A. E.; Lochner, C. M.; Pierre, A.; Arias, A. C. Monitoring of Vital Signs with Flexible and Wearable Medical Devices. *Adv Mater* **2016**, *28* (22), 4373–4395.
- (2) Choi, M.-C.; Kim, Y.; Ha, C.-S. Polymers for Flexible Displays: From Material Selection to Device Applications. *Prog Polym Sci* **2008**, *33* (6), 581–630.
- (3) Zhao, Q.; Qi, J. H.; Xie, T. Recent Progress in Shape Memory Polymer: New Behavior, Enabling Materials, and Mechanistic Understanding. *Prog Polym Sci* **2015**, *49*, 79–120.
- (4) Ware, T.; Simon, D.; Hearon, K.; Liu, C.; Shah, S.; Reeder, J.; Khodaparast, N.; Kilgard, M. P.; Maitland, D. J.; Rennaker, R. L.; et al. Three-Dimensional Flexible Electronics Enabled by Shape Memory Polymer Substrates for Responsive Neural Interfaces. *Macromol Mater Eng* **2012**, *297* (12), 1193–1202.
- (5) Reeder, J.; Kaltenbrunner, M.; Ware, T.; Arreaga-Salas, D.; Avendano-Bolivar, A.; Yokota, T.; Inoue, Y.; Sekino, M.; Voit, W.; Sekitani, T.; et al. Mechanically Adaptive Organic Transistors for Implantable Electronics. *Adv Mater* **2014**, *26* (29), 4967–4973.
- (6) Gutierrez-Heredia, G.; Rodriguez-Lopez, O.; Garcia-Sandoval, A.; Voit, W. E. Highly Stable Indium-Gallium-Zinc-Oxide Thin-Film Transistors on Deformable Softening Polymer Substrates. *Adv Electron Mater* **2017**, *3* (10), 1700221.
- (7) MacDonald, W. A. Engineered Films for Display Technologies. *J Mater Chem* **2003**, *14* (1), 4–10.
- (8) Voit, W.; Ware, T.; Dasari, R. R.; Smith, P.; Danz, L.; Simon, D.; Barlow, S.; Marder, S. R.; Gall, K. High-Strain Shape-Memory Polymers. *Adv Funct Mater* **2010**, *20* (1), 162–171.
- (9) Fu, Q.; Cao, C.-B.; Zhu, H.-S. Preparation of Alumina Films from a New Sol–Gel Route. *Thin Solid Films* **1999**, *348* (1–2), 99–102.
- (10) Heo, S.; Yoon, D.; Jung, T.; Kim, H. Recent Advances in Low-Temperature Solution-Processed Oxide Backplanes. *J Information Disp* **2013**, *14* (2), 79–87.
- (11) Brinker, C.; Scherer, G. Sol–Gel Science: The Physics And Chemistry of Sol–Gel Processing. **1990**.

- (12) Liu, A.; Zhu, H.; Guo, Z.; Meng, Y.; Liu, G.; Fortunato, E.; Martins, R.; Shan, F. Solution Combustion Synthesis: Low-Temperature Processing for P-Type Cu:NiO Thin Films for Transparent Electronics. *Adv Mater* **2017**, *29* (34), 1701599.
- (13) Meng, Y.; Liu, G.; Liu, A.; Song, H.; Hou, Y.; Shin, B.; Shan, F. Low-Temperature Fabrication of High Performance Indium Oxide Thin Film Transistors. *Rsc Adv* **2015**, *5* (47), 37807–37813.
- (14) Wang, B.; Yu, X.; Guo, P.; Huang, W.; Zeng, L.; Zhou, N.; Chi, L.; Bedzyk, M. J.; Chang, R. P.; Marks, T. J.; et al. Solution-Processed All-Oxide Transparent High-Performance Transistors Fabricated by Spray-Combustion Synthesis. *Adv Electron Mater* **2016**, *2* (4), 1500427.
- (15) Tetzner, K.; Lin, Y.-H.; Regoutz, A.; Seitkhan, A.; Payne, D. J.; Anthopoulos, T. D. Sub-Second Photonic Processing of Solution-Deposited Single Layer and Heterojunction Metal Oxide Thin-Film Transistors Using a High-Power Xenon Flash Lamp. *J Mater Chem C* **2017**, *5* (45), 11724–11732.
- (16) Kim, Y.-H.; Heo, J.-S.; Kim, T.-H.; Park, S.; Yoon, M.-H.; Kim, J.; Oh, M.; Yi, G.-R.; Noh, Y.-Y.; Park, S. Flexible Metal-Oxide Devices Made by Room-Temperature Photochemical Activation of Sol–Gel Films. *Nature* **2012**, *489* (7414), 128.
- (17) Hwang, Y.; Seo, S.-J.; Jeon, J.-H.; Bae, B.-S. Ultraviolet Photo-Annealing Process for Low Temperature Processed Sol-Gel Zinc Tin Oxide Thin Film Transistors. *Electrochem Solid-state Lett* **2012**, *15* (4), H91.
- (18) Dellis, S.; Isakov, I.; Kalfagiannis, N.; Tetzner, K.; Anthopoulos, T. D.; Koutsogeorgis, D. C. Rapid Laser-Induced Photochemical Conversion of Sol–Gel Precursors to In₂O₃ Layers and Their Application in Thin-Film Transistors. *J Mater Chem C* **2017**, *5* (15), 3673–3677.
- (19) Jun, T.; Song, K.; Jeong, Y.; Woo, K.; Kim, D.; Bae, C.; Moon, J. High-Performance Low-Temperature Solution-Processable ZnO Thin Film Transistors by Microwave-Assisted Annealing. *J Mater Chem* **2010**, *21* (4), 1102–1108.
- (20) Park, S.; Kim, K.; Jo, J.; Sung, S.; Kim, K.; Lee, W.; Kim, J.; Kim, H.; Yi, G.; Kim, Y.; et al. In-Depth Studies on Rapid Photochemical Activation of Various Sol–Gel Metal Oxide Films for Flexible Transparent Electronics. *Adv Funct Mater* **2015**, *25* (19), 2807–2815.
- (21) Park, Y.; Desai, A.; Salleo, A.; Jimison, L. Solution-Processable Zirconium Oxide Gate Dielectrics for Flexible Organic Field Effect Transistors Operated at Low Voltages. *Chem Mater* **2013**, *25* (13), 2571–2579.

- (22) Ware, T.; Simon, D.; Arreaga-Salas, D. E.; Reeder, J.; Rennaker, R.; Keefer, E. W.; Voit, W. Fabrication of Responsive, Softening Neural Interfaces. *Adv Funct Mater* **2012**, *22* (16), 3470–3479.
- (23) Daunis, T. B.; Gutierrez-Heredia, G.; Rodriguez-Lopez, O.; Wang, J.; Voit, W. E.; Hsu, J. W. Solution-Deposited Al₂O₃ Dielectric towards Fully-Patterned Thin Film Transistors on Shape Memory Polymer. *Proceeding of SPIE* **2017**, 101051Z-101051Z – 8.
- (24) Lee, D. -H.; Chang, Y. -J.; Herman, G.; Chang, C. -H. A General Route to Printable High-Mobility Transparent Amorphous Oxide Semiconductors. *Adv Mater* **2007**, *19* (6), 843–847.
- (25) Rim, Y.; Chen, H.; Liu, Y.; Bae, S.-H.; Kim, H.; Yang, Y. Direct Light Pattern Integration of Low-Temperature Solution-Processed All-Oxide Flexible Electronics. *Acs Nano* **2014**, *8* (9), 9680–9686.
- (26) Jo, J.; Kim, J.; Kim, K.; Kang, J.; Kim, M.; Kim, K.; Ko, H.; Kim, Y.; Park, S. Highly Stable and Imperceptible Electronics Utilizing Photoactivated Heterogeneous Sol-Gel Metal–Oxide Dielectrics and Semiconductors. *Adv Mater* **2015**, *27* (7), 1142–1142.
- (27) Honda, F.; Hirokawa, K. X-Ray Photoelectron Spectroscopic Observation of Nitrogen-Containing Gases Adsorbed at High Pressures on Some Transition Metals. *J Electron Spectrosc* **1977**, *10* (2), 125–136.
- (28) Baltrusaitis, J.; Jayaweera, P. M.; Grassian, V. H. XPS Study of Nitrogen Dioxide Adsorption on Metal Oxide Particle Surfaces under Different Environmental Conditions. *Phys Chem Phys* **2009**, *11* (37), 8295–8305.
- (29) Hwang, J.; Lee, K.; Jeong, Y.; Lee, Y.; Pearson, C.; Petty, M. C.; Kim, H. UV-Assisted Low Temperature Oxide Dielectric Films for TFT Applications. *Adv Mater Interfaces* **2014**, *1* (8), 1400206.
- (30) Yu, X.; Smith, J.; Zhou, N.; Zeng, L.; Guo, P.; Xia, Y.; Alvarez, A.; Aghion, S.; Lin, H.; Yu, J.; et al. Spray-Combustion Synthesis: Efficient Solution Route to High-Performance Oxide Transistors. *Proc National Acad Sci* **2015**, *112* (11), 3217–3222.
- (31) Sanctis, S.; Hoffmann, R. C.; Bruns, M.; Schneider, J. J. Direct Photopatterning of Solution-Processed Amorphous Indium Zinc Oxide and Zinc Tin Oxide Semiconductors—A Chimie Douce Molecular Precursor Approach to Thin Film Electronic Oxides. *Adv Mater Interfaces* **2018**, *5* (15), 1800324.
- (32) Nayak, P. K.; Hedhili, M.; Cha, D.; Alshareef, H. High Performance In₂O₃ Thin Film Transistors Using Chemically Derived Aluminum Oxide Dielectric. *Appl Phys Lett* **2013**, *103* (3), 033518.

- (33) Xu, Y.; Li, X.; Zhu, L.; Zhang, J. Defect Modification in ZnInSnO Transistor with Solution-Processed Al₂O₃ Dielectric by Annealing. *Mat Sci Semicon Proc* **2016**, *46*, 23–28.
- (34) Xu, W.; Wang, H.; Xie, F.; Chen, J.; Cao, H.; Xu, J.-B. Facile and Environmentally Friendly Solution-Processed Aluminum Oxide Dielectric for Low-Temperature, High-Performance Oxide Thin-Film Transistors. *Acs Appl Mater Inter* **2015**, *7* (10), 5803–5810.
- (35) Zhang, Y.; Huang, G.; Duan, L.; Dong, G.; Zhang, D.; Qiu, Y. Full-Solution-Processed High Mobility Zinc-Tin-Oxide Thin-Film-Transistors. *Sci China Technological Sci* **2016**, *59* (9), 1407–1412.
- (36) Liu, A.; Zhu, H.; Sun, H.; Xu, Y.; Noh, Y. Solution Processed Metal Oxide High- κ Dielectrics for Emerging Transistors and Circuits. *Adv Mater* **2018**, *30* (33), 1706364.

CHAPTER 4
**EFFECTS OF ENVIRONMENTAL WATER ABSORPTION BY SOLUTION-
DEPOSITED AL₂O₃ GATE DIELECTRICS ON THIN FILM TRANSISTOR
PERFORMANCE AND MOBILITY**

Authors – Trey B. Daunis, James M. H. Tran, and Julia W. P. Hsu

Department of Materials Science and Engineering, RL 10

The University of Texas at Dallas

800 West Campbell Road

Richardson, Texas 75080-3021

Reprinted with permission from Daunis, T. B.; Tran, M. H.; Hsu, J. W. P. Effects of Environmental Water Absorption by Solution-Deposited Al₂O₃ Gate Dielectrics on Thin Film Transistor Performance and Mobility. *ACS Appl. Mater. Interfaces* **2018**, 10, 39435-39440. Copyright 2018 American Chemical Society.

4.1 Preface

In Chapter 3, thin film transistors (TFTs) using solution-deposited Al_2O_3 as the gate dielectric and solution-deposited In_2O_3 as the semiconductor were fabricated. These devices showed several unexpected behaviors: large frequency dispersion in the gate capacitance, large counter-clockwise hysteresis in the transfer curves, unusually high mobility, and changes in these behaviors over time. This chapter presents the results of a study of these behaviors. Detailed film and device characterization are presented using varied materials, structures, and processing conditions for the gate dielectric. The result is the identification of the absorption of atmospheric water by the dielectric as the culprit of the above phenomena.

My contribution was in fabricating and characterizing films and devices, data analysis, and manuscript preparation. James M. H. Tran assisted in film and device fabrication as well as capacitance-frequency measurements, Fourier-transform infrared (FTIR) spectroscopy, Kelvin probe measurements, and data preparation. Prof. Julia W. P. Hsu provided valuable guidance on all aspects of the project and assistance with manuscript preparation.

4.2 Abstract

In recent years many solution-processed oxide transistors have been reported with mobility rivaling or exceeding their vacuum-deposited counterparts. Here we show that water absorption from the environment by solution-processed dielectric materials explains this enhanced mobility. By monitoring the water content of Al_2O_3 , ZrO_2 , and bilayer dielectric materials, we demonstrate how water absorption by the dielectric affects electrical characteristics in solution-processed metal oxide transistors. These effects, including capacitance-frequency dispersion, counter-

clockwise hysteresis in transfer curves, and high channel mobility, are elucidated by electron transfer between the gate/channel and trap states within the band gap of the dielectric created by the water.

4.3 Introduction

With the promise of increased throughput, lower cost, and compatibility with flexible polymer substrates, solution-processed oxide thin film electronics have gained popularity but come at the expense of decreased performance, such as lower channel mobility. Thin film transistor (TFT) channel mobility of 1-100 $\text{cm}^2 \cdot \text{V}^{-1} \cdot \text{s}^{-1}$ is often reported for metal oxide semiconductors using vacuum-processed (e.g. atomic layer deposited or sputtered) high- κ metal oxide gate dielectrics.¹ Only recently have similar mobilities become commonly reported for solution-processed metal oxide TFTs.² Understanding the origin of the recently reported high mobility is critical for the continued improvement of solution-processed oxide electronics.

Table 4.1 shows a summary of high mobility ($> 30 \text{ cm}^2 \cdot \text{V}^{-1} \cdot \text{s}^{-1}$) TFTs based on n-type metal oxide semiconductors on solution-processed Al_2O_3 dielectrics. In nearly all cases, frequency dispersion is present in the capacitance vs. frequency (C-f) behavior, with capacitance increasing at lower frequency. Equation 1.1 shows how saturation channel mobility, μ , is calculated from TFT transfer curves. The capacitance values used to extract mobility in Table 4.1 vary from those measured at 1 MHz to those extrapolated to 1 Hz. Because the transfer curve used to extract mobility is measured in a quasi-steady state (low frequency), the actual capacitance of the gate during the transistor measurement may be significantly higher, when C-f dispersion is present, than that measured at a higher frequency and used in the mobility calculation.

Table 4.1: Literature survey of high-mobility ($> 30 \text{ cm}^2 \cdot \text{V}^{-1} \cdot \text{s}^{-1}$) oxide TFTs on solution-processed Al_2O_3 gate dielectrics.

Mobility ($\text{cm}^2 \cdot \text{V}^{-1} \cdot \text{s}^{-1}$)	Capacitance Frequency Used	Counter- Clockwise Hysteresis in Transfer Curve	C-f Dispersion in Al_2O_3	Al_2O_3 Annealing Temperature ($^\circ\text{C}$)	Channel Material
117	1MHz	N/A	N/A	600	ZITO ^{*3}
84.4	1kHz	No	No	350	IGZO ^{†4}
57.2	100 Hz	Small	Small	300	In_2O_3 ⁵
112	1 kHz	N/A	Yes	450	ZTO ^{*6}
30.9	100 Hz	Yes	Yes	250	In_2O_3 ⁷
36.3	1 kHz	No	No	250	In_2O_3 ⁸
127	1 MHz	N/A	Yes	350	In_2O_3 ⁹
33	10 kHz	Yes	N/A	300	ZTO ¹⁰
40	1 kHz – 1 MHz	Yes	Yes	250	In_2O_3 ¹¹
46.2	1 Hz	Yes	Yes	250	In_2O_3 ¹²
44.2	20 Hz	Yes	Yes	350	Li-ZnO ¹³
160 (86)	10 kHz (20 Hz)	Yes	Yes	250	In_2O_3 ¹⁴

*Zn-In-Sn-O, †In-Ga-Zn-O, ‡Zn-Sn-O

While using a better estimate of capacitance at steady state in the mobility equation reduces the calculated mobility (many of the highest reported mobilities were calculated using capacitance measured between 1 kHz and 1 MHz), this correction alone cannot fully explain the high mobilities reported. Also, a counter-clockwise hysteresis is observed in the transfer curve in almost all cases. In this work, we investigate the origin of the high extracted mobility values seen in metal oxide TFTs using solution-processed Al_2O_3 gate dielectrics. The link between high mobility and the presence of counter-clockwise hysteresis in the transfer curve along with a

dispersive C-f behavior is studied through fabrication of TFTs and capacitors using different metal oxide gate dielectric materials (Al_2O_3 vs. ZrO_2), dielectric structures (single material vs. bilayer gate dielectrics), and processing conditions (sol-gel vs. atomic layer deposition (ALD)). To minimize the error in the calculated mobility caused by under-estimating the steady-state capacitance, areal capacitance values at the lowest measured frequency, 100 Hz, are used in all mobility calculations.

4.4 Experimental Details

4.4.1 Film and Device Fabrication

The precursor solutions for Al_2O_3 and ZrO_2 are made by dissolving $\text{Al}(\text{NO}_3)_3 \cdot 9\text{H}_2\text{O}$ (0.4 M) or $\text{ZrO}(\text{NO}_3)_2$ (0.15M) in 2-MOE and stirring uncapped at 70 °C for 18 hours. The evaporated volume of solvent is replaced with 2-MOE and the solution is filtered through a 0.2 μm PTFE filter. Oxide films are made by placing a p^{++} Si substrate in a UV-ozone (UVO) apparatus (Bioforce Nanosciences Procleaner Plus) for 20 minutes before spin coating precursor solution at 3,000 rpm for 30 seconds. The film is dried at 70 °C for 3 minutes and then cured in UVO for 40 minutes. A second coat is deposited with the same procedure. The film is then annealed first at 150 °C for 5 minutes followed by 250 °C for 20 minutes. Annealed films are ~40 nm thick per coat for Al_2O_3 and ~15 nm per coat for ZrO_2 . Thinner coats are achieved by diluting the precursor solution with 2-MOE. Bilayer films were made by deposition and UVO exposure of each material sequentially, followed by final thermal annealing at 250 °C.

The In_2O_3 channel was deposited in a similar manner as the dielectric materials using 0.1 M $\text{In}(\text{NO}_3)_3 \cdot 3\text{H}_2\text{O}$, 0.1 M acetylacetone, and 0.1 M NH_4OH in 2-MOE stirred at room temperature

for 48 hours. UVO exposure time for these films was 10 minutes through a shadow mask followed by a 10 second rinse in a methanol / deionized water / acetic acid (15:5:1) solution to pattern the semiconductor. The annealing procedure was the same as for the dielectric films. Al source and drain contacts were evaporated through a shadow mask.

20 nm atomic layer deposited (ALD) Al_2O_3 was deposited in a Savannah 100 Atomic Layer Deposition System at 250 °C using trimethylaluminum and water as the Al and O precursors, respectively, under 20 sccm of N_2 flow at a base pressure of 0.3 torr. The pulse length for each precursor was 0.015 seconds with a 5 second interval between pulses and a growth rate of 1.07 Å/cycle.

4.4.2 Materials and Device Characterization

C-f from 100 Hz to 300 kHz (LCR measurement) was measured using an Agilent 4284A Precision LCR Meter with 0V DC bias and 50 mV AC amplitude (100 mV for measurements in Figure 4.11). Very low frequency C-f from 0.01 Hz to 10 Hz (VLF measurement) was measured using the VLF C-V technique included in the Keithley 4200-SCS Semiconductor Characterization System with 0V DC bias and 100 mV AC amplitude. Transfer curves were measured in a Keithley 4200-SCS with drain voltage at 3V.

Fourier-transform infrared (FTIR) spectra were measured on films on lightly doped n-type Si substrates (100 Ω -cm) from 4000 to 2500 cm^{-1} using a Nicolet iS50 FT-IR with a mercury cadmium telluride (MCT-A) detector and under N_2 purge. X-ray photoelectron spectroscopy (XPS) was performed on a Ulvac-PHI VersaProbe2 with a monochromated Al K α source (1486.8 eV) at an angle of 45° to the sample surface with an energy step of 0.2 eV and a pass energy of 23.5 eV. XPS data were analyzed using commercial software (MultiPak, Ulvac-PHI).

Work function measurements were performed by Kelvin probe method using a SKP 5050-SPS (KP Technology). Oxide layer thicknesses were determined by ellipsometry (J. A. Woollam, M2000DI) of films deposited on Si measured from 280 to 1690 nm at 55°, 65°, and 75° and fit using a Cauchy model.

4.5 Results and Discussion

4.5.1 Capacitance-Frequency Dispersion in the Dielectric

Figure 4.1 shows the C-f response, dissipation factor, and FTIR spectra in the water stretching region ($4000\text{-}2500\text{ cm}^{-1}$)^{15,16} for Al₂O₃ and ZrO₂ capacitors and films. The as-made Al₂O₃ films show a large frequency dispersion with capacitance increasing at low frequencies ($\epsilon_r = 5.8 - 7.7$). Correspondingly, the Al₂O₃ film shows a large broad peak ($3800\text{-}2600\text{ cm}^{-1}$) in the IR signal that corresponds to the presence of liquid water,¹⁶ as opposed to surface-bonded hydroxyls, which appear as multiple narrow peaks in the $3000 - 3500\text{ cm}^{-1}$ region.¹⁷ The C-f dispersion is consistent with the high dielectric constant (~ 80) and slow polarization response of water.¹⁸ In contrast, the C-f response for as-made ZrO₂ is relatively non-dispersive ($\epsilon_r = 12.9 - 13.5$), with a minimal IR peak in the water region. After storing the films in air (RH = 30% - 35%) for 12 days, the dispersive C-f behavior of the Al₂O₃ film increases dramatically, while the response of the ZrO₂ film remains the same. Correspondingly, FTIR shows a substantial increase in the water content of Al₂O₃ but no change in ZrO₂ after 14 days in air. These results show that the Al₂O₃ films contain more water after processing and are much more susceptible to water absorption over time than ZrO₂ films. The higher the water content in the dielectric films, the larger the C-f dispersion and the higher the dissipation factor for the C-f measurement.

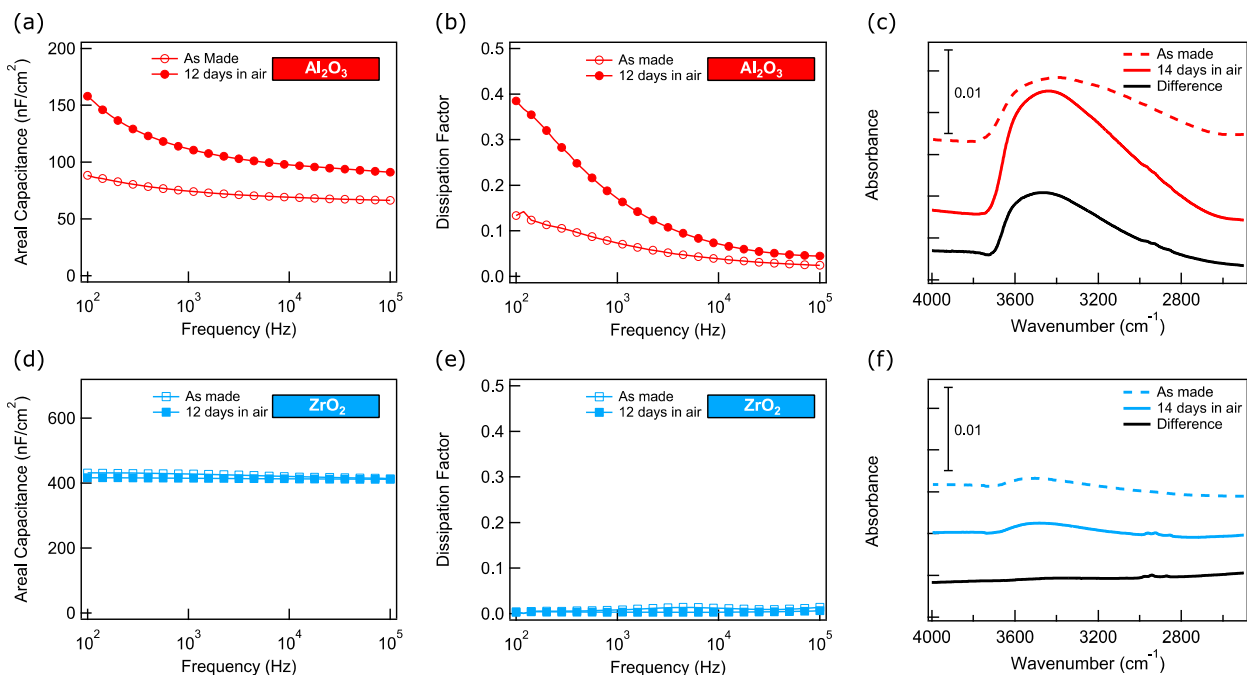


Figure 4.1: C-f response, dissipation factor, and FTIR spectra of solution-processed dielectric films before and after prolonged exposure to air. C-f: (a) Al_2O_3 , and (d) ZrO_2 . Dissipation factor: (b) Al_2O_3 and (e) ZrO_2 . Open symbols represent results on as-made films and closed symbols represent data taken after 12 days stored in air with RH = 30% - 35%. In (d) and (e), the before and after results for ZrO_2 overlap. FTIR spectra: (c) Al_2O_3 and (f) ZrO_2 . Dashed colored lines represent as-made films and solid colored lines represent films after 14 days in air, with the difference shown in black lines. Small IR signals between 2900 and 2800 cm^{-1} are due to adventitious hydrocarbon from environmental exposure.

To verify that adsorbed water is responsible for the C-f behavior, we further anneal Al_2O_3 as well as subject Al_2O_3 and ZrO_2 to soaking in deionized (DI) water (Figure 4.2). Mild annealing of the Al_2O_3 capacitors removes water and reduces the dispersive C-f behavior; however, FTIR shows re-absorption of water with air exposure. This absorption and desorption of water, as opposed to hydroxylation, is expected at low temperatures.¹⁹ Furthermore, both Al_2O_3 and ZrO_2 films respond to being soaked overnight in DI water similarly to being stored in air for 12 to 14 days, confirming that water absorption by Al_2O_3 results in the observed C-f dispersion and IR signals while ZrO_2 is unaffected by exposure to water (Figure 4.3). Hence, these results

unambiguously establish the presence of water in Al₂O₃ films. Additionally, for both Al₂O₃ and ZrO₂ films, FTIR shows complete removal of nitrate ions from precursors and XPS shows no nitrogen signal (Figure 4.4). Thus, the presence of water in Al₂O₃ is not linked to the presence of nitrate as was proposed in Ref. 13.

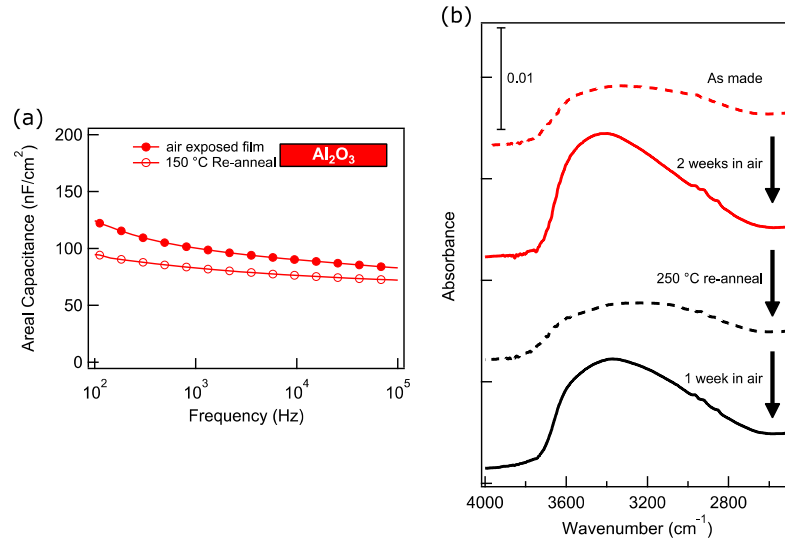


Figure 4.2: Effect of re-annealing Al₂O₃ film after exposure to air. (a) Capacitance of air exposed Al₂O₃ film before (closed circles) and immediately after (open circles) re-annealing at 150 °C for 20 minutes. (b) FTIR spectra for an Al₂O₃ film as-made (dashed red line), after 2 weeks in air (solid red line), after re-annealing at 250 °C for 20 minutes (dashed black line), and after an additional 1 week in air (solid black line).

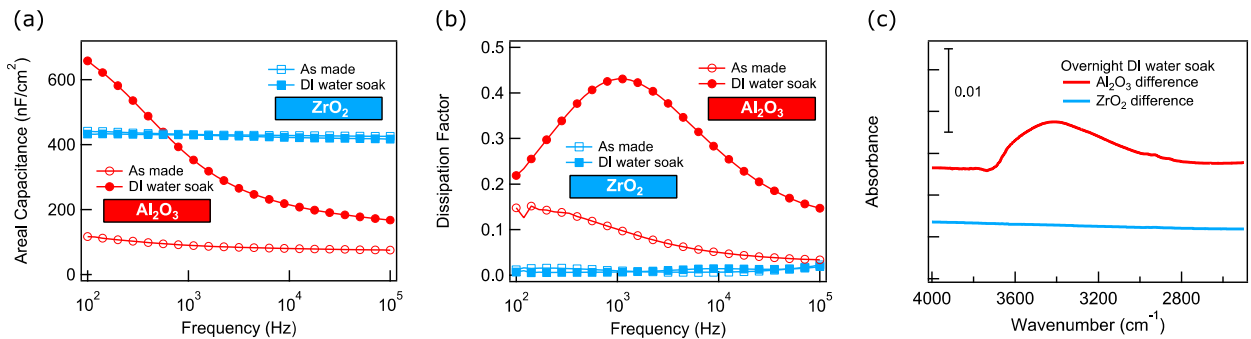


Figure 4.3: C-f response, dissipation factor, and FTIR spectra of solution-processed dielectric films before and after soaking in DI water. (a) C-f and (b) dissipation factor for Al₂O₃ (red circles) and ZrO₂ (blue squares) before (open symbols) and after (closed symbols) soaking in DI water overnight. The before and after results for ZrO₂ overlap. (c) FTIR difference spectra for Al₂O₃ (red) and ZrO₂ (blue) showing the change in FTIR absorbance after the DI water soak.

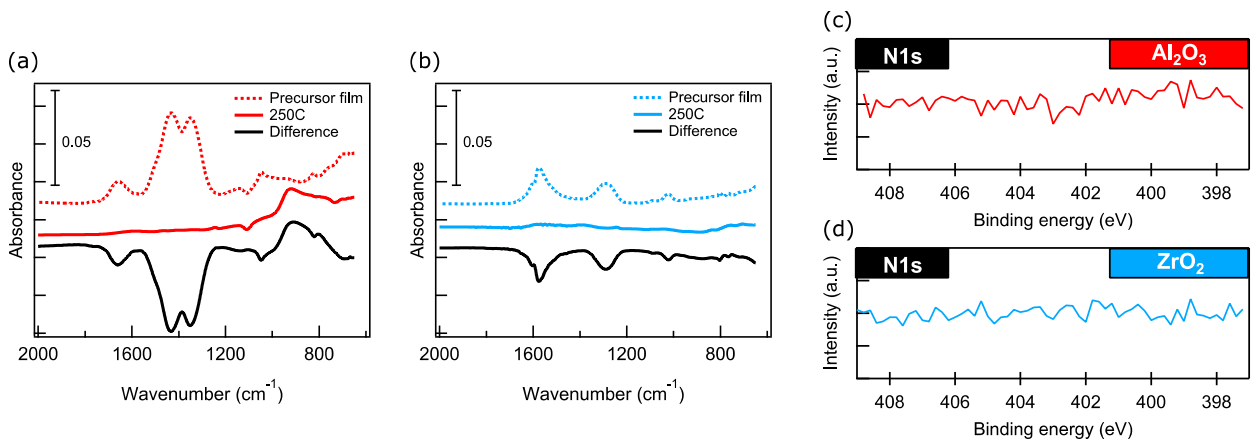


Figure 4.4: Removal of nitrates during annealing. FTIR spectra of (a) Al_2O_3 and (b) ZrO_2 dielectric films in the nitrate region from 2000 to 600 cm^{-1} for precursor films (dashed colored lines), films annealed at 250 $^\circ\text{C}$ (solid colored lines), and the difference spectrum (solid black lines). XPS spectra of nitrogen N 1s region for 250 $^\circ\text{C}$ annealed (c) Al_2O_3 and (d) ZrO_2 films.

We further examine the water absorption behavior on bilayer dielectric films consisting of Al_2O_3 on top of ZrO_2 and ZrO_2 on top of Al_2O_3 (Figure 4.5). When Al_2O_3 is on top of ZrO_2 , and hence is exposed to the environment, the bilayer film behaves similarly to the pure Al_2O_3 film, displaying a dispersive C-f response and water peak in FTIR; both increase upon soaking in DI water. When ZrO_2 is on top of Al_2O_3 , the bilayer film behaves as the ZrO_2 film, with no initial C-f dispersion as well as no change in C-f behavior or increase in water content (as shown in FTIR) upon soaking in DI water. The dissipation factor follows a similar trend. These results show that when ZrO_2 is deposited on top of Al_2O_3 prior to thermal annealing, it acts as an effective barrier layer which prevents water absorption by the underlying Al_2O_3 films.

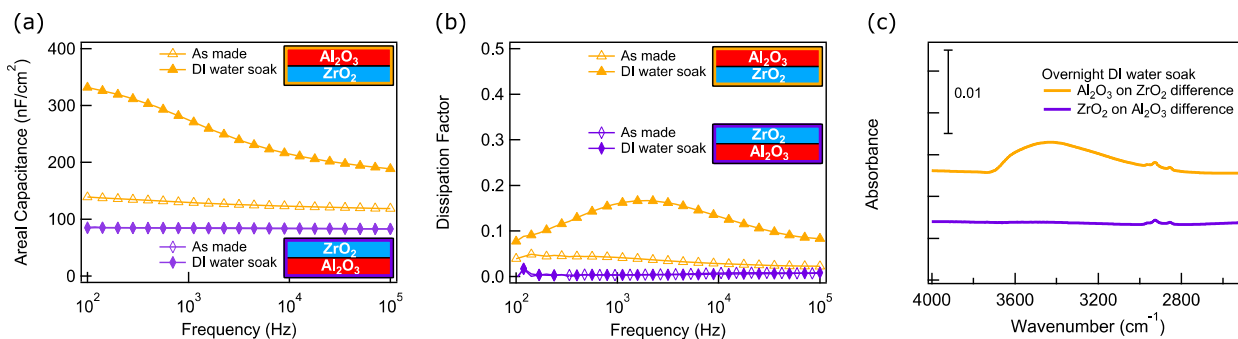


Figure 4.5: C-f response, dissipation factor, and FTIR spectra of bilayer solution-processed dielectric films before and after soaking in DI water. (a) C-f and (b) dissipation factor for Al₂O₃ on ZrO₂ (orange triangles) and ZrO₂ on Al₂O₃ (purple diamonds) before (open symbols) and after (closed symbols) soaking in DI water overnight. The before and after results for ZrO₂ on Al₂O₃ overlap. (c) FTIR difference spectra for Al₂O₃ on ZrO₂ (orange) and ZrO₂ on Al₂O₃ (purple) showing the change in FTIR absorbance after the DI water soak.

Ataka et al. showed that the broad FTIR peak in the region of 3600 – 3000 cm⁻¹ is associated with surface liquid water, with its sign and shape determined by the molecular orientation.¹⁶ The broad FTIR water absorption peak observed here for Al₂O₃ indicates that the water molecules are oriented with the oxygen atom toward the metal oxide surface. When the oxide films are studied by Kelvin probe measurements as a function of exposure time in air, we find a stable work function for ZrO₂, but a decreasing work function for Al₂O₃ over time (Figure 4.6a). This result indicates the development of a surface dipole layer on Al₂O₃ with the dipole moment pointing away from the surface, consistent with the water molecule orientation indicated by the FTIR results. Furthermore, Al₂O₃ film thickness dependence for the FTIR water peak indicates that water is present in the bulk, in addition to the surface, of the Al₂O₃ film (Figure 4.6b). If water were to be absorbed as a surface layer only, the FTIR peak intensity would be independent of film thickness.

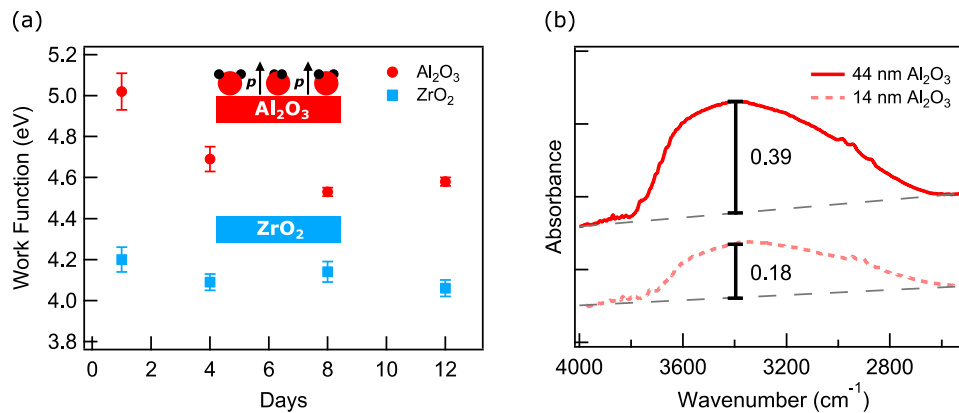


Figure 4.6: Location and orientation of adsorbed water on oxide films. (a) Kelvin probe work function measurement of Al₂O₃ (red circles) and ZrO₂ (blue squares) films stored in air over 12 days. Inset shows schematics of an Al₂O₃ film with a surface water layer and a surface dipole pointing away from the surface, and a ZrO₂ film with no water or surface dipole. (b) FTIR spectra of thick (44 nm, solid red line) and thin (14 nm, dashed light red line) Al₂O₃ films. Dashed black lines show background and solid black lines show height of water peak above background at 3395 cm⁻¹.

4.5.2 Transistor Hysteresis and High Mobility

Transistors were fabricated using each of the four dielectric films on a p⁺⁺ silicon back gate. The In₂O₃ channel was deposited in a similar manner as the dielectric materials (section 4.4.1). Transfer curves for each device are shown in Figure 4.7. The transistor on Al₂O₃ gate dielectric displays a very high mobility ($\mu = 125 \text{ cm}^2 \cdot \text{V}^{-1} \cdot \text{s}^{-1}$) and a large counter-clockwise hysteresis. In contrast, the transistor on ZrO₂ shows a much lower mobility ($\mu = 1.3 \text{ cm}^2 \cdot \text{V}^{-1} \cdot \text{s}^{-1}$) despite the higher gate capacitance (due to higher ZrO₂ dielectric constant), and a negligible clockwise hysteresis. The clockwise hysteresis is commonly attributed to electron trapping at the dielectric-semiconductor interface during operation.²⁰ When Al₂O₃ on top of ZrO₂ is used as the dielectric, the mobility ($\mu = 6.7 \text{ cm}^2 \cdot \text{V}^{-1} \cdot \text{s}^{-1}$) is lower than that on pure Al₂O₃, but higher than that on pure ZrO₂. Despite capacitors made with this dielectric showing C-f dispersion similar to that of pure Al₂O₃, the transfer curve does not show counter-clockwise hysteresis as the transistor on Al₂O₃.

This result demonstrates that the counter-clockwise hysteresis is not due to mobile ion charges or slow polarization response within the bulk of the dielectric, as previously attributed by other authors.²⁰⁻²² If such ions were the cause of the hysteresis, we would expect to see a similar behavior for pure Al₂O₃ (Figure 4.7a) and for Al₂O₃ on top of ZrO₂ (Figure 4.7c) dielectrics.²¹ Finally, when ZrO₂ is on top of Al₂O₃ the mobility ($\mu = 1.0 \text{ cm}^2 \cdot \text{V}^{-1} \cdot \text{s}^{-1}$) is similar to the device on pure ZrO₂ dielectric, and again no counter-clockwise hysteresis is evident.

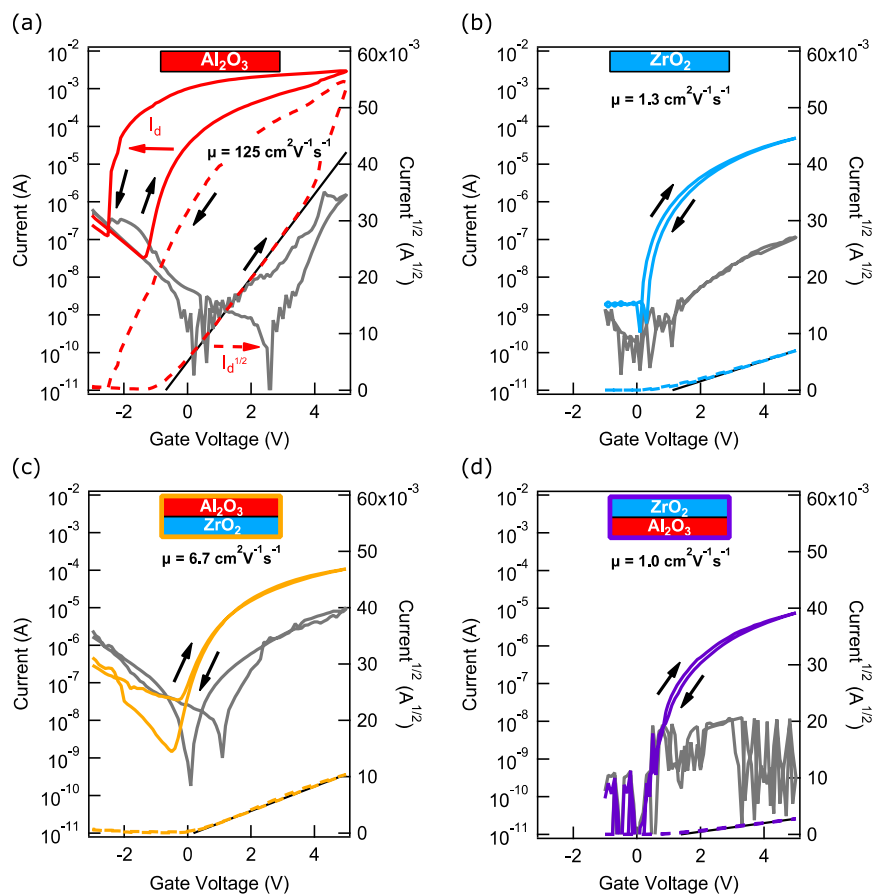


Figure 4.7: Transfer curves for In₂O₃ TFTs with (a) Al₂O₃, (b) ZrO₂, (c) bilayer Al₂O₃ on ZrO₂, and (d) bilayer ZrO₂ on Al₂O₃ as the gate dielectric. Solid colored lines show drain current (I_D , left axis), dashed colored lines show $I_D^{1/2}$ (right axis), grey lines show gate current (I_G), and solid black straight lines show fits used for mobility calculation using C measured at 100 Hz. Black arrows show the direction of the gate voltage scan.

4.5.3 Charge Transfer from Dielectric to Gate

We have shown that unusually high mobility ($\mu > 30 \text{ cm}^2 \cdot \text{V}^{-1} \cdot \text{s}^{-1}$) is present only when two conditions are met simultaneously: (1) the gate dielectric contains a large amount of water, and (2) the portion of the gate dielectric containing water is in contact with the gate. Associated with the high mobility, we also observe a large counter-clockwise hysteresis in the transfer curve. Both effects can be explained by a mechanism proposed by Zeumault and Subramanian, whereby electrons trapped within the dielectric are transferred to the gate during positive gate bias.²³ This process results in positive charges in the dielectric near the gate accompanied by an increased electric field within the dielectric, and hence induces a higher electron concentration in the channel (Figure 4.8a). The increase in charge carrier concentration in the channel is responsible for the increased channel current. Because this charge transfer is induced by positive gate bias, the mobility calculated from the saturation channel current using Equation 1.1 is overestimated. Under positive gate bias with increasing time, more electrons from trap states further into the dielectric are transferred to the gate, leaving behind more positive charges in the dielectric. Figure 4.8b shows measurements of drain current ($V_D = 3\text{V}$) on a transistor with pure Al_2O_3 gate dielectric vs. time. When the transistor is in the off-state or in the on-state with zero gate bias, there is no change in I_D with time. When the transistor is in the on-state with positive gate bias, I_D increases with time.

For charge transfer from a monoenergetic state in the bulk of the dielectric into the gate, we expect the electron emission time at a given gate bias to increase exponentially as the distance of the trap from the gate/dielectric interface increases.²⁴ Assuming these states are evenly distributed throughout the thickness of the dielectric, we expect the electric field in the dielectric,

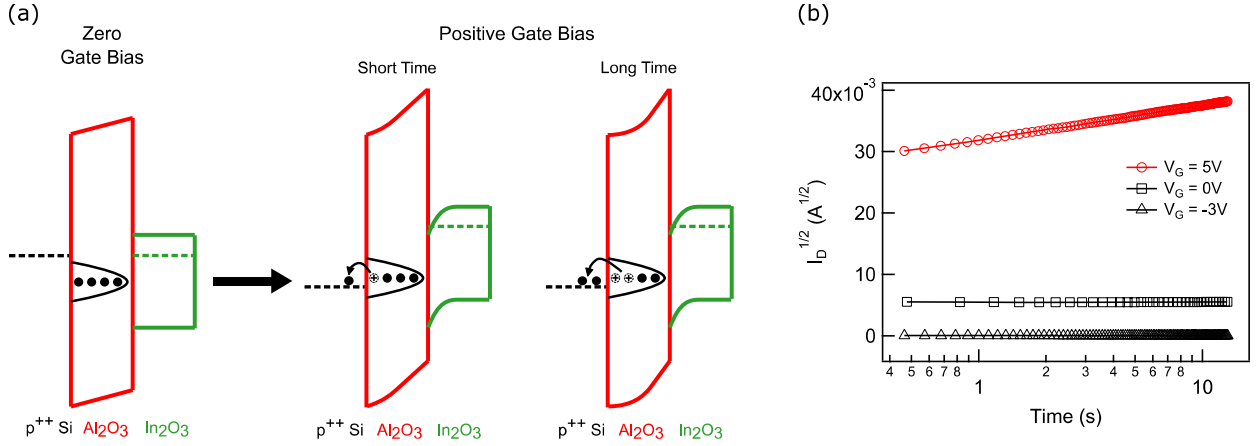


Figure 4.8: Time dependence of I_D due to charge transfer from dielectric to gate. (a) Band diagram showing electron transfer from defect states in Al₂O₃ to the gate contact under positive gate bias and with time. (b) I_D vs. time measurement with $V_D = 3V$ for an In₂O₃ transistor on Al₂O₃ in the off-state ($V_G = -3V$, black triangles), in the on-state with no positive gate bias ($V_G = 0V$, black squares) and in the on-state with positive gate bias ($V_G = 5V$, red circles), which shows $I_D^{1/2}$ increases linearly with $\log(\text{time})$.

thus also compensatory channel charges, to linearly increase with logarithmic time. The time dependence of the drain current, I_D , under positive gate bias, V_G , can thus be determined by first rearranging Equation 1.1 into the saturation drain current equation:

$$I_D = \frac{1}{2} \mu C \frac{W}{L} (V_G - V_T)^2 \quad (4.1)$$

where μ is the channel mobility, C is the areal gate capacitance, W is the channel width, L is the channel length, and V_T is the threshold voltage. Combining this equation with:

$$C = \frac{q}{V} \quad (4.2)$$

where q is the areal charge induced across the gate dielectric, we arrive at:

$$\sqrt{I_D} = \sqrt{\frac{1}{2} \mu \frac{W}{LC}} (q_V - q_0) \quad (4.3)$$

where q_V is the charge in the channel at V_G and q_0 is the charge in the channel at V_T . Since the argument in the square root in Equation 4.3 is constant, we arrive at the following:

$$\Delta\sqrt{I_D} \propto \Delta q \propto \Delta\log(t) \quad (4.4)$$

where t is time, which shows that a change in $\log(t)$ results in a proportional change in $I_D^{1/2}$ as is seen in the experimental results (Figure 4.8b, red curve).

While they proposed the existence of electron trap states in the dielectric band gap, Zeumault and Subramanian did not identify the origin of these defect states. Here we identify water as the source of these defect states in the dielectrics. We can now understand each case in Figure 4.7. When pure Al_2O_3 is used as the dielectric, the Al_2O_3 is exposed to the environment and absorbs water. This induces filled electron states in the dielectric band gap, which transfer charges to the gate under positive gate-bias resulting in an increase in channel current and negative threshold voltage shift (counter-clockwise hysteresis). ZrO_2 does not absorb water and does not contain trap states; therefore, no such effects are observed. We can also rule out water absorbed by the semiconductor as the origin of the hysteresis,²⁵ as water effects on the semiconductor would not depend on the dielectric material and the FTIR spectrum of In_2O_3 exhibits negligible changes (Figure 4.9). When ZrO_2 is inserted between Al_2O_3 and the gate, although trap states exist in the Al_2O_3 , charge transfer from the Al_2O_3 to the gate is blocked and again no enhanced mobility or large counter clockwise hysteresis are observed. Zeumault and Subramanian also suggested that the same defect states donate electrons directly into the channel, producing increased channel mobility due to a higher electron concentration in the semiconductor. This explains the higher mobility seen in the TFT with dielectric of Al_2O_3 on top of ZrO_2 compared to that in the TFT using pure ZrO_2 dielectric, despite the smaller overall gate capacitance. Comparing Figures 4.7a and 4.7c, the donor effect is not responsible for the anomalously large mobility or the large counter-clockwise hysteresis. Finally, when ZrO_2 is deposited on top of Al_2O_3 , the Al_2O_3 is not

exposed to air and does not absorb water. In this case there is also no charge transfer to the gate due to the absence of band gap states.

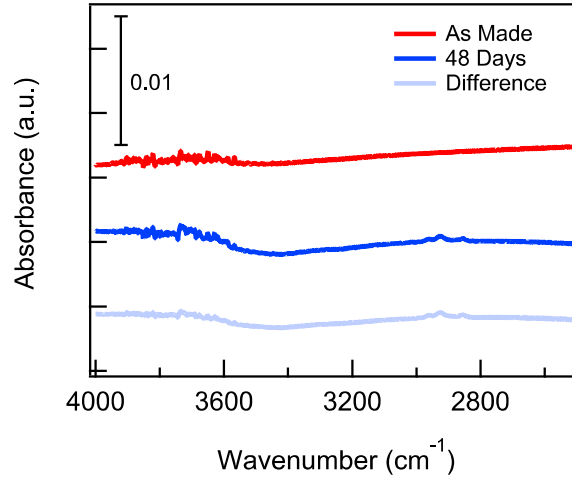


Figure 4.9: FTIR spectra of an In₂O₃ film as made (red), after 48 days in air (dark blue), and the difference (light blue).

4.5.4 Effect of Materials Processing

Previous research has shown that unusually high mobility ($>30 \text{ cm}^2 \cdot \text{V}^{-1} \cdot \text{s}^{-1}$) is greatly reduced when the gate dielectric is annealed at higher temperature (500 °C),⁹ which is consistent with water in the dielectric as the culprit. Figure 4.10a depicts the FTIR spectra of our solution-processed Al₂O₃ films annealed at 500 °C: the as-made film has less water compared to the standard (250 °C) film, but the 2-day old film still shows water absorption.

While we use solution-deposited Al₂O₃ to demonstrate the effects of water, these behaviors may be seen in different dielectric materials (such as ZrO₂)²³ or may not be present at all in solution-deposited Al₂O₃.² It is important to note that this tendency of the dielectric to absorb water is not a function of the oxide material only (Al₂O₃ here), but rather a combination of the material, the precursors, and the conversion process. However, the exact mechanism by which

these factors affect a metal oxide's ability to absorb water is beyond the scope of this research. To establish that this is a result of the processing method, rather than an intrinsic property of Al_2O_3 as the gate dielectric, we fabricated a transistor with a dielectric consisting of 60 nm solution-processed Al_2O_3 on top of 20 nm ALD deposited Al_2O_3 (all annealed or deposited at 250°C). The transfer curve of this device (Figure 4.10b) resembles that in Figure 4.7c (Al_2O_3 on ZrO_2) with mobility of $4.5\text{ cm}^2\cdot\text{V}^{-1}\cdot\text{s}^{-1}$ and no counter-clockwise hysteresis, indicating that only the solution-processed Al_2O_3 , which is susceptible to water absorption, causes the telltale electrical characteristics when in contact with the gate.

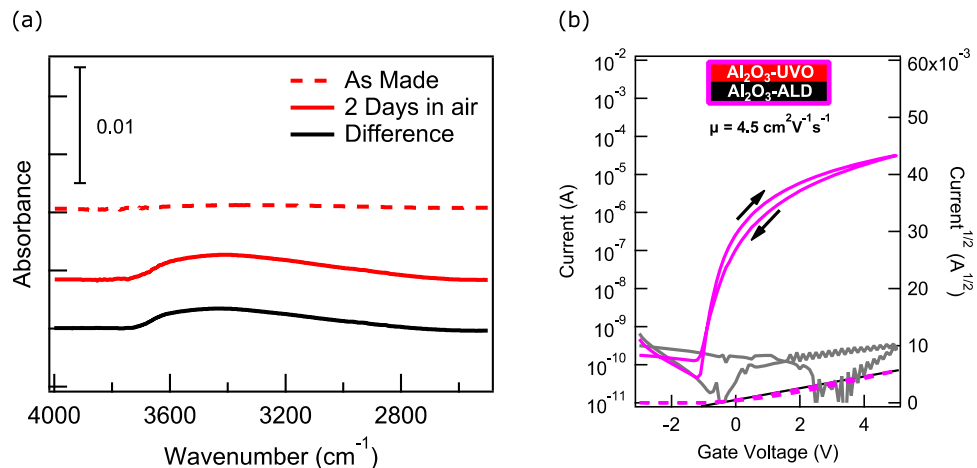


Figure 4.10: Effect of processing conditions on Al_2O_3 dielectric films. (a) FTIR spectra of an Al_2O_3 film annealed at 500°C as made (dashed red line) and after 2 days in air (solid red line). The difference spectrum is shown as a solid black line. (b) Transfer curve for In_2O_3 transistor with dielectric film composed of solution processed Al_2O_3 annealed at 250°C on top of 20 nm of atomic layer deposited Al_2O_3 (250°C). Drain current (I_D) (solid magenta line, left axis), gate current (solid grey line, left axis), $\text{sqrt}(I_D)$ (dashed magenta line, right axis), and fit used for mobility calculation (solid black line).

4.5.5 Corrections for Channel Width and Gate Dielectric Frequency Dispersion

In all transistors thus far in Chapters 2, 3, and 4, the channel width is defined by the source and drain (S / D) contacts as depicted in Figure 4.11a, resulting in fringe current outside of the

nominal channel area. Additionally, the gate capacitance values used to calculate mobility are measured between 20 Hz and 10 kHz. Sections 3.5.2 and 4.3 discussed how these factors lead to the over-estimation of the channel mobility. To measure the mobility without the fringe current effect, we fabricated In₂O₃ TFTs on Al₂O₃ and ZrO₂ gate dielectrics using the design shown in Figure 4.11b where the channel width is defined by the semiconductor boundaries. To get a closer approximation of the steady-state gate capacitance, we performed very low frequency (VLF) capacitance measurements down 0.01 Hz. Figure 4.11 shows the results of these measurements and the corresponding mobility values. The C-f measurements on these devices show the expected frequency dispersion in the Al₂O₃ and bilayer Al₂O₃ on ZrO₂ dielectrics and flat frequency response of the ZrO₂ dielectric for the LCR measurements from 300 kHz down to 100 Hz. VLF measurements from 10 Hz down to 0.01 Hz show a further large increase in capacitance for Al₂O₃ as frequency decreases, a smaller increase for Al₂O₃ on ZrO₂, and very little change in capacitance for ZrO₂ at low frequency. Using the capacitance measured at 100 Hz, as in Figure 4.7, the mobility is 35 cm²·V⁻¹·s⁻¹ when Al₂O₃ is used as the gate dielectric and 0.5 cm²·V⁻¹·s⁻¹ when ZrO₂ is used – a 72% and 62% reduction, respectively, compared to the devices with fringe current. Both devices have a similar reduction in mobility since the fringe current effect depends only on the device geometry and not the dielectric material. The calculated mobility on the ZrO₂ dielectric remains 0.5 cm²·V⁻¹·s⁻¹ when the capacitance measured at 0.01 Hz is used; however, on Al₂O₃ the mobility decreases from 35 to 11 cm²·V⁻¹·s⁻¹. This is because at low frequency, the increase in gate capacitance due to both the direct contribution by water in the dielectric and that of the charge transfer effect are more fully accounted for. The remaining difference between the mobilities on the two dielectrics is likely

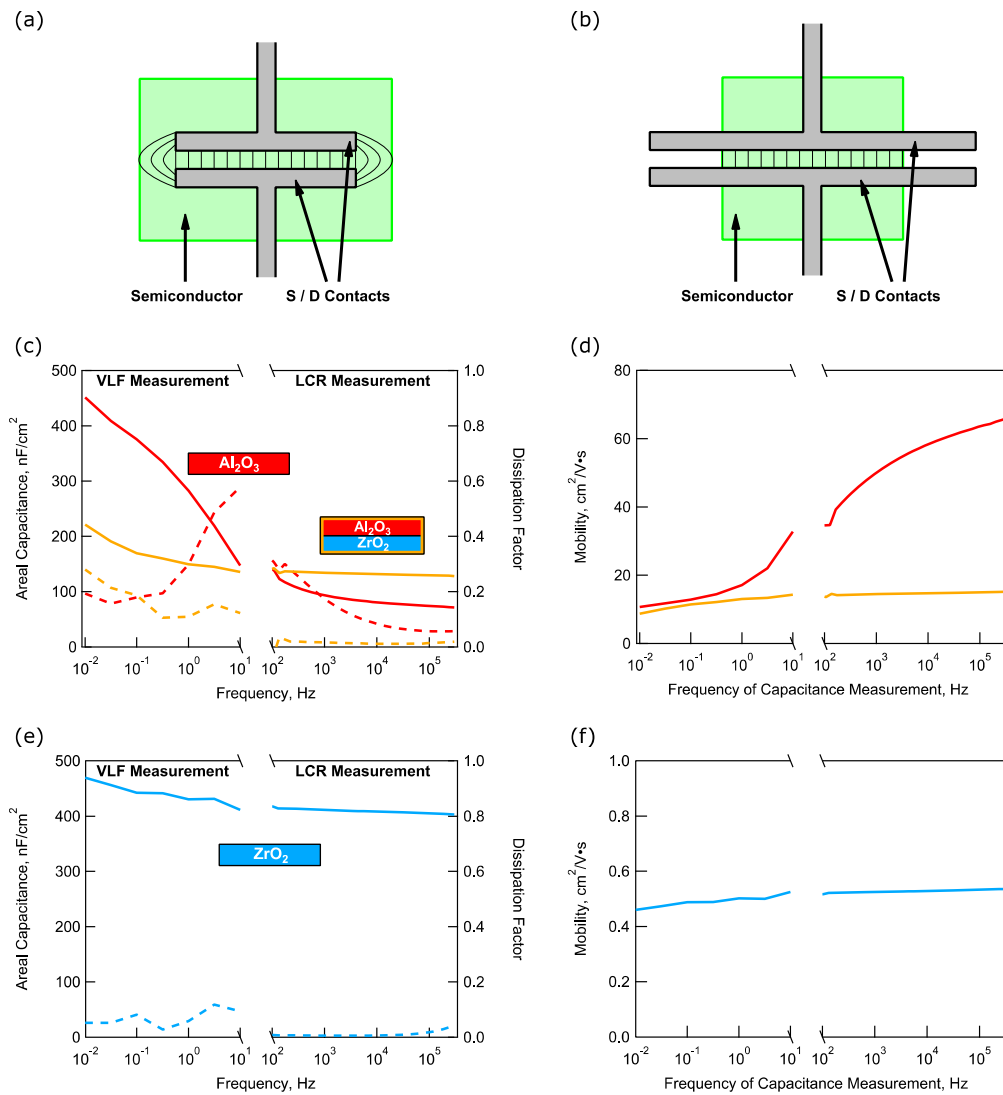


Figure 4.11: Corrections for channel width and gate dielectric frequency dispersion in mobility calculation. (a) Schematic of the S / D contact (grey) and semiconductor (green) pattern for a channel with width defined by S / D contacts. The channel current is depicted by thin black lines with fringe current outside of the defined channel depicted by curved black lines. (b) Schematic of the S / D contact and semiconductor pattern for a channel with width defined by the semiconductor and no fringe current. Areal capacitance (solid lines) and dissipation factor (dashed lines) vs. frequency for (c) Al₂O₃ (red) and bilayer Al₂O₃ on ZrO₂ (orange) and (e) ZrO₂ MIM capacitors measured by VLF (10⁻² – 10¹ Hz, left x-axis) and LCR (10² – 3x10⁵ Hz, right x-axis) techniques. Mobility of TFTs (In₂O₃ semiconductor with (d) Al₂O₃ (red) and bilayer Al₂O₃ on ZrO₂ (orange) and (f) ZrO₂ gate dielectric) with the channel defined by the semiconductor, as in (b), calculated using the areal capacitance data in (c) and (e).

due to the different semiconductor/dielectric interface for the two samples as well as the non-equilibrium nature of the channel charge density during the voltage sweep in the transfer curve measurement due to the charge transfer effect in the device with Al₂O₃ gate dielectric. This non-equilibrium effect results in non-ideal transfer curve behavior which cannot be fully represented by Equation 1.1.²⁴ The device using the bilayer Al₂O₃ on ZrO₂ dielectric has a higher mobility when calculated from the 100 Hz capacitance measurement than the device in Figure 4.7. This may be due to device to device variations. However, when the capacitance measured at 0.01 Hz is used, correcting for the frequency dispersion in the dielectric, the mobility approaches 8.8 cm²·V⁻¹·s⁻¹, a similar value to that for the device with Al₂O₃ dielectric.

Figure 4.12 shows the I_D vs. V_D output curve measurements for the device using Al₂O₃ on ZrO₂ as the gate dielectric. The linear response of I_D vs. V_D at low V_D for all gate voltages indicates good ohmic contact between the In₂O₃ channel and the Al source and drain contacts when Al₂O₃ is present at the top of the dielectric, ruling out source and drain contact effects as the source of the observed hysteresis.

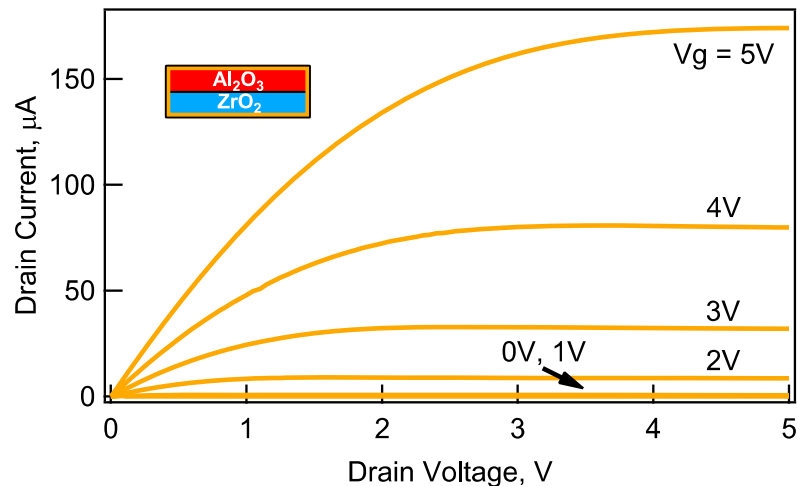


Figure 4.12: I_D vs. V_D curves for transistor with bilayer Al₂O₃ on ZrO₂ gate dielectric and In₂O₃ channel. V_G is measured from 0V to 5V with 1V step and V_D is swept from 0V to 5V.

4.6 Conclusions

Previous studies have reported the effects of humidity on transistor performance and postulated water induced deep-level trap states in metal oxide semiconductors without direct evidence of water in their oxides.^{26–28} Here we show that water absorbed from the environment, with direct evidence provided by FTIR, in the solution-processed Al₂O₃ gate dielectric leads to specific TFT performance characteristics (C-f dispersion, counter-clockwise hysteresis in transfer curve, high extracted channel mobility), allowing us to unambiguously identify water as the source of trap states in the dielectrics. Reports of similar TFT behavior in the literature are likely caused by water induced gap states in the dielectrics. Further research into understanding how the materials and precursor selection and processing conditions influence water absorption ability and thus device characteristics will be key to improving the performance of solution-processed oxide electronics.

4.7 Acknowledgments

The authors thank Dr. Robert Wallace for the use of the spectroscopic ellipsometer. This work is partially supported by the National Science Foundation (NSF DMR-1305893) and the University of Texas at Dallas. J.W.P.H. acknowledges support from the Texas Instruments Distinguished Chair in Nanoelectronics.

4.8 References

- (1) Fortunato, E.; Barquinha, P.; Martins, R. Oxide Semiconductor Thin-Film Transistors: A Review of Recent Advances. *Adv Mater* **2012**, *24* (22), 2945–2986.
- (2) Liu, A.; Zhu, H.; Sun, H.; Xu, Y.; Noh, Y. Solution Processed Metal Oxide High- κ Dielectrics for Emerging Transistors and Circuits. *Adv Mater* **2018**, *30* (33), 1706364.

- (3) Xu, Y.; Li, X.; Zhu, L.; Zhang, J. Defect Modification in ZnInSnO Transistor with Solution-Processed Al₂O₃ Dielectric by Annealing. *Mat Sci Semicon Proc* **2016**, *46*, 23–28.
- (4) Rim, Y.; Chen, H.; Liu, Y.; Bae, S.-H.; Kim, H.; Yang, Y. Direct Light Pattern Integration of Low-Temperature Solution-Processed All-Oxide Flexible Electronics. *Acs Nano* **2014**, *8* (9), 9680–9686.
- (5) Xu, W.; Wang, H.; Xie, F.; Chen, J.; Cao, H.; Xu, J.-B. Facile and Environmentally Friendly Solution-Processed Aluminum Oxide Dielectric for Low-Temperature, High-Performance Oxide Thin-Film Transistors. *Acs Appl Mater Inter* **2015**, *7* (10), 5803–5810.
- (6) Zhang, Y.; Huang, G.; Duan, L.; Dong, G.; Zhang, D.; Qiu, Y. Full-Solution-Processed High Mobility Zinc-Tin-Oxide Thin-Film-Transistors. *Sci China Technological Sci* **2016**, *59* (9), 1407–1412.
- (7) Xu, W.; Long, M.; Zhang, T.; Liang, L.; Cao, H.; Zhu, D.; Xu, J.-B. Fully Solution-Processed Metal Oxide Thin-Film Transistors via a Low-Temperature Aqueous Route. *Ceram Int* **2017**, *43* (8), 6130–6137.
- (8) Rim, Y.; Chen, H.; Song, T.-B.; Bae, S.-H.; Yang, Y. Hexaaqua Metal Complexes for Low-Temperature Formation of Fully Metal Oxide Thin-Film Transistors. *Chem Mater* **2015**, *27* (16), 5808–5812.
- (9) Nayak, P. K.; Hedhili, M.; Cha, D.; Alshareef, H. High Performance In₂O₃ Thin Film Transistors Using Chemically Derived Aluminum Oxide Dielectric. *Appl Phys Lett* **2013**, *103* (3), 033518.
- (10) Avis, C.; Jang, J. High-Performance Solution Processed Oxide TFT with Aluminum Oxide Gate Dielectric Fabricated by a Sol–Gel Method. *J Mater Chem* **2011**, *21* (29), 10649–10652.
- (11) Kim, M.-G.; Kanatzidis, M. G.; Facchetti, A.; Marks, T. J. Low-Temperature Fabrication of High-Performance Metal Oxide Thin-Film Electronics via Combustion Processing. *Nat Mater* **2011**, *10* (5), 382–388.
- (12) Park, H.; Nam, Y.; Jin, J.; Bae, B.-S. Space Charge-Induced Unusually-High Mobility of a Solution-Processed Indium Oxide Thin Film Transistor with an Ethylene Glycol Incorporated Aluminum Oxide Gate Dielectric. *Rsc Adv* **2015**, *5* (124), 102362–102366.
- (13) Park, J.; Kim, K.; Yoo, Y.; Park, S.; Lim, K.-H.; Lee, K.; Baik, H.; Kim, Y. Water Adsorption Effects of Nitrate Ion Coordinated Al₂O₃ Dielectric for High Performance Metal-Oxide Thin-Film Transistor. *J Mater Chem C* **2013**, *1* (43), 7166–7174.

- (14) Daunis, T. B.; Barrera, D.; Gutierrez-Heredia, G.; Rodriguez-Lopez, O.; Wang, J.; Voit, W. E.; Hsu, J. Solution-Processed Oxide Thin Film Transistors on Shape Memory Polymer Enabled by Photochemical Self-Patterning. *J Mater Res* **2018**, *33* (17), 2454–2462.
- (15) Al-Abadleh, H. A.; Grassian, V. FT-IR Study of Water Adsorption on Aluminum Oxide Surfaces. *Langmuir* **2003**, *19* (2), 341–347.
- (16) Ataka, K.; Yotsuyanagi, T.; Osawa, M. Potential-Dependent Reorientation of Water Molecules at an Electrode/Electrolyte Interface Studied by Surface-Enhanced Infrared Absorption Spectroscopy. *J Phys Chem* **1996**, *100* (25), 10664–10672.
- (17) Kiss, A. B.; Keresztury, G.; Farkas, L. Raman and i.r. Spectra and Structure of Boehmite (γ -AlOOH). Evidence for the Recently Discarded D172h Space Group. *Spectrochimica Acta Part Mol Spectrosc* **1980**, *36* (7), 653–658.
- (18) Rusiniak, L. Dielectric Properties and Structure of Water at Room Temperature. New Experimental Data in 5 Hz–13 Mhz Frequency Range. *Phys Chem Earth Part Solid Earth Geodesy* **2000**, *25* (2), 201–207.
- (19) Baumgarten, E.; Wagner, R.; Lentjes-Wagner, C. Quantitative Determination of Hydroxyl Groups on Alumina by IR Spectroscopy. *Anal Bioanal Chem* **1989**, *334* (3), 246–251.
- (20) Yang, W.; Song, K.; Jung, Y.; Jeong, S.; Moon, J. Solution-Deposited Zr-Doped AlO_x Gate Dielectrics Enabling High-Performance Flexible Transparent Thin Film Transistors. *J Mater Chem C* **2013**, *1* (27), 4275–4282.
- (21) Jo, J.-W.; Kim, K.-H.; Kim, J.; Ban, S.-G.; Kim, Y.-H.; Park, S. High-Mobility and Hysteresis-Free Flexible Oxide Thin-Film Transistors and Circuits by Using Bilayer Sol-Gel Gate Dielectrics. *Acs Appl Mater Inter* **2017**, *10* (3), 2679–2687.
- (22) Ye, Z.; Yuan, Y.; Xu, H.; Liu, Y.; Luo, J.; Wong, M. Mechanism and Origin of Hysteresis in Oxide Thin-Film Transistor and Its Application on 3-D Nonvolatile Memory. *Ieee T Electron Dev* **2017**, *64* (2), 438–446.
- (23) Zeumault, A.; Subramanian, V. Mobility Enhancement in Solution-Processed Transparent Conductive Oxide TFTs Due to Electron Donation from Traps in High-k Gate Dielectrics. *Adv Funct Mater* **2016**, *26* (6), 955–963.
- (24) Wager, J. F. Transfer-curve Assessment of Oxide Thin-film Transistors. *J Soc Inf Display* **2010**, *18* (10), 749–752.
- (25) Fakhri, M.; Johann, H.; Görrn, P.; Riedl, T. Water as Origin of Hysteresis in Zinc Tin Oxide Thin-Film Transistors. *Acs Appl Mater Inter* **2012**, *4* (9), 4453–4456.

(26) Lee, K.-H.; Jung, J.; Son, K.; Park, J.; Kim, T.; Choi, R.; Jeong, J.; Kwon, J.-Y.; Koo, B.; Lee, S. The Effect of Moisture on the Photon-Enhanced Negative Bias Thermal Instability in Ga–In–Zn–O Thin Film Transistors. *Appl Phys Lett* **2009**, *95* (23), 232106.

(27) Lopes, M.; Gomes, H.; Medeiros, M.; Barquinha, P.; Pereira, L.; Fortunato, E.; Martins, R.; Ferreira, I. Gate-Bias Stress in Amorphous Oxide Semiconductors Thin-Film Transistors. *Appl Phys Lett* **2009**, *95* (6), 063502.

(28) Park, J.-S.; Jeong, J.; Chung, H.-J.; Mo, Y.-G.; Kim, H. Electronic Transport Properties of Amorphous Indium-Gallium-Zinc Oxide Semiconductor upon Exposure to Water. *Appl Phys Lett* **2008**, *92* (7), 072104.

CHAPTER 5

PHOTONIC CURING OF SOLUTION-DEPOSITED ZrO₂ DIELECTRIC ON

POLYETHYLENE NAPHTHALATE:

HIGH-THROUGHPUT PROCESSING OF OXIDE ELECTRONICS

Authors – Trey B. Daunis,^a Kurt A. Schroder,^b and Julia W. P. Hsu^a

^aDepartment of Materials Science and Engineering, RL 10

The University of Texas at Dallas

800 West Campbell Road

Richardson, Texas 75080-3021

^bNovaCentrix

400 Parker Drive, Suite 1110

Austin, Texas 78728

5.1 Preface

This chapter presents the results of my final research project. The previous chapters show how high-performance metal oxide thin film electronics can be fabricated by solution methods on flexible substrates. However, the process used in those chapters requires a thermal annealing step which limits the potential for high-throughput and low-cost manufacturing of oxide electronics. In this chapter, we adapt photonic curing – the use intense pulses of broad-spectrum light to cure thin films, typically used for sintering printed metal nanoparticle inks into conductive traces – to cure metal oxide thin films on flexible substrates. The challenge is to find a photonic curing condition which can convert oxide precursors into high-quality metal oxide films without damaging the fragile plastic substrate. We demonstrate that this can be done while incorporating simultaneous patterning of the oxide film and at speeds that can match common roll-to-roll printing and coating methods.

My contribution was performing the experiments, analyzing the results, and preparing the manuscript. Dr. Kurt A. Schroder provided guidance on photonic curing and reviewed and edited the manuscript. Prof. Julia W. P. Hsu. supervised the research, contributed to analysis of the results, and assisted with manuscript preparation and review.

5.2 Abstract

High throughput manufacturing of oxide electronics will enable new applications ranging from large-area displays to flexible medical devices and low-cost solar panels. However, high quality oxide films from solution-based precursors typically require 20 minutes or more of thermal annealing at high temperature (> 250 °C) for each layer, severely limiting both the

throughput and substrate choice. Here, we report high speed photonic curing of ZrO₂ dielectric thin films on flexible plastic substrates. The curing and patterning processes can be achieved simultaneously by using shadow mask patterning or adjusting conditions to convert oxide only on top of underlying metal contacts, i.e. self-aligned patterning. Metal-insulator-metal capacitors using two layers of ZrO₂ films photonicallly cured in just 100 seconds per layer show non-dispersive capacitance-frequency behavior from 10² to 10⁶ Hz, high areal capacitance of 200 nF/cm² and low dissipation factor of 0.03 at 10⁵ Hz, leakage current density of ~ 10⁻⁷ A/cm² at an applied field of 2 MV/cm, and a breakdown field of nearly 8 MV/cm. Using an upgraded tool, similar dielectric properties are achieved in as short as 100 milliseconds using a single pulse of light, revealing a pathway to oxide film processing beyond 30 m/min.

5.3 Introduction

Thin film electronics are currently used extensively in large-area applications including flat panel displays¹ and photovoltaics.² Their compatibility with flexible plastic substrates further allows for many emerging applications such as wearable or implantable sensors and biomedical devices^{3,4} and non-planar form-factor systems in curved displays or sensor arrays. Beyond cases where mechanical flexibility is necessary for the device application, flexible substrates enable high throughput roll-to-roll manufacturing processes which bring the advantage of low capital cost and the economy of scale.⁵ For example, roll-to-roll manufacturing has enabled the proliferation of low-cost radio frequency identification tags over the last two decades⁶ and its implementation is a major goal in the production of organic electronics⁷ and perovskite solar cells (PSC).^{8,9} When sheet-to-sheet PSC throughput is increased from 0.5 m²/min to 2.5 m²/min, manufacturing costs decrease by ~35%.¹⁰ A web speed of 30 m/min would allow for production

of 3 GW/yr of solar panels from a single roll-to-roll system (www.enmatcorp.com). Solution-based printing (ink-jet, screen, gravure, flexo) and coating (blade, slot-die, spray) methods have lower costs and higher throughput than vacuum-based methods, and can already exceed 10 m/min web speed.^{7,11} However, both solution- and vacuum-deposited oxide films require post-deposition annealing to achieve optimal electrical performance.^{12,13} As the maximum rate is determined by the slowest processing step, the elimination of long thermal annealing treatments is critical.

The two major classes of electronic materials used for thin film devices are organic and oxide materials. In addition to their superior stability and optical transparency compared to organic materials, oxides take on a wide range of possible materials' properties and include conductors, semiconductors, and dielectrics with superior conductivity, mobility, and dielectric constant, respectively. To date, however, organic materials have held the advantage because they can be solution processed with low thermal budgets. Recently, efforts to reduce the annealing temperature of sol-gel based oxides (traditionally > 400 °C)¹⁴ have focused on solution-combustion synthesis and UV light annealing.¹⁵ In the solution-combustion method, fuel and oxidizer included in the chemical precursors provide some of the energy required for the formation of metal oxide bonds, reducing the amount of thermal energy required to convert the precursors to oxides.^{13,16} Conversion of combustion films still requires heating the substrate and film to a relatively high temperature of 250 – 300 °C¹⁷⁻¹⁹ for at least 20 minutes plus additional time for heating and cooling. This is repeated for each layer of oxide deposited; typically, multiple layers for each material (conductor, semiconductor, or dielectric) are required. This type of equilibrium heating is problematic due to the coefficient of thermal expansion mismatch

between the metal oxide film (~ 5 ppm/ $^{\circ}\text{C}$) and the polymer substrate ($15 - 70$ ppm/ $^{\circ}\text{C}$),²⁰ resulting in cracking of the oxide, especially for polymers with a low glass transition temperature.²¹ Thus, solution-combustion synthesis alone is inadequate for making oxide electronics on low-temperature polymer substrates, such as polyethylene terephthalate (PET, 150 $^{\circ}\text{C}$) and polyethylene naphthalate (PEN, 220 $^{\circ}\text{C}$).²² UV assisted annealing, on the other hand, uses energy from UV light to reduce the thermal energy needed for oxide formation.²³⁻³² This photochemical processing takes advantage of the absorption of UV light by oxide precursors, facilitating precursor decomposition and formation of metal-oxide bonds.^{24,26,30,33} Mild equilibrium heating, provided by the UV lamp or an external source, to only 150 $^{\circ}\text{C}$ is enough to form high quality oxide semiconductors³² and dielectrics.²⁵ However, processing times up to 90 minutes are necessary. In a roll-to-roll process, both solution-combustion and UV-assisted annealing would translate to either exceedingly slow web speeds or exceedingly large ovens. Rapid thermal annealing using a high intensity infra-red light source can greatly reduce annealing time by using a high heating rate, but it still heats both oxide films and plastic substrates together to a high temperature and can result in thermal stress in the oxide film and/or substrate damage. To achieve selective film heating, laser annealing³⁴ and photonic curing,³⁵ which do not require additional heating and can operate under atmospheric conditions, have emerged as alternatives to thermal annealing.

Using 20 μs to 20 ms light pulses from a broad spectrum (200 - 1500 nm) xenon flash lamp, photonic curing can heat a thin film to several hundred degrees over a short time while maintaining the substrate below its degradation temperature.^{36,37} This preferential heating of the film over the substrate is the key advantage of photonic curing in performing high-temperature

processing on low-temperature substrates. As with pulsed laser annealing, the extremely high power of the light pulse used in photonic curing, as much as 50 kW/cm², means that high temperatures can be reached at the surface of a sample where most of the light absorption occurs while the bulk of the substrate remains cool. This is due to the substrate's high (relative to the thin film) thermal mass and the short duration of the photonic curing pulse, and hence low total energy (<100 J/cm²) delivered to the sample. While laser annealing is limited by its processing area, and thus speed, photonic curing can have a uniform processing area of 100s of cm² per pulse. Photonic curing is a proven manufacturing technique for high-speed sintering of printed metal nanoparticle inks into conductive traces on flexible substrates.³⁸ To date, only a few reports exist on photonic curing of oxide dielectrics³⁹ and semiconductors^{40–45} on rigid substrates. On flexible substrates, photonic curing of IGZO thin film transistors has been demonstrated in combination with high temperature thermal annealing on polyimide,⁴⁶ and In₂O₃ films on PEN with a thick polyimide intermediate layer have been evaluated through materials characterization but without device evaluation.⁴⁷ Perovskite solar cells fabricated on photonic curing of TiO₂ transport layers on flexible PET substrates have been demonstrated, but show lower performance compared to those on TiO₂ annealed at high temperature on rigid substrates.^{48,49} Here we demonstrate, for the first time, high quality photonic curing of oxide dielectric thin films directly on low-temperature PEN substrates. Flexible capacitors using this dielectric demonstrate high areal capacitance (> 200 nF/cm²), low dissipation factor (0.03 at 10⁵ Hz), negligible capacitance-frequency dispersion, low leakage current density (~ 10⁻⁷ A/cm² at 2 MV/cm applied field), and high breakdown field (8 MV/cm) – properties which are typically

only achieved with lengthy (~ 60 min) UV curing and/or high temperature (250 °C) thermal annealing.⁵⁰

5.4 Experimental Details

5.4.1 Film Deposition

ZrO₂ precursor solution is made by dissolving 0.15 or 0.4 M ZrO(NO₃)₂ in 2-methoxyethanol (2-MOE) and stirring uncapped overnight at 80 °C until approximately half of the solution has evaporated. The lost volume is made up with fresh 2-MOE and the solution is filtered through 0.2 µm PTFE filters prior to deposition.

PEN substrates (Teijin Teonex[®] Q65HA, 100 µm thickness, untreated side is used) are cleaned in isopropyl alcohol for 15 minutes in an ultrasonic bath, rinsed with de-ionized (DI) water, and dried. Bottom contacts (100 nm Al) are deposited by thermal evaporation through a shadow mask or patterned and etched by traditional photolithography. The substrates are cut to 25 mm by 25 mm pieces and UV-ozone (UVO) treated (Bioforce Nanosciences Procleaner Plus) for 20 minutes prior to spin coating. During spin coating, substrates are held in place by a porous vacuum chuck (Laurel Technologies). ZrO₂ precursor solution is spin coated at 3,000 rpm for 30 seconds and the films are dried on a hotplate at 80 °C for 3 minutes to remove excess 2-MOE.

5.4.2 Photonic Curing

Photonic curing is performed using a NovaCentrix PulseForge[®] Invent equipped with 1 lamp driver (500 V max), a 3 A power supply, and a 20 mm diameter by 150 mm length xenon flash lamp (beam size 150 mm by 75 mm) except where otherwise noted. Samples are placed on the

sample chuck which is set to 7 mm below the lamp. A 0.005” thick invar shadow mask is placed on the sample (if used) and the mask and sample are held in place by steel slats with magnets. Photonic curing is performed in air. In the case of b-PC, no further processing is done after photonic curing. In sm-PC and sa-PC, photonic cured samples are dipped into a developing solution of methanol, water, and acetic acid in a 15:5:1 ratio for 5 seconds and rinsed in DI water. These samples are then photonic cured a second time using the same conditions as for b-PC/sm-PC films.

5.4.3 SimPulse® Simulation

Radiant exposure values are simulated using SimPulse® photonic curing simulation software. Film and substrate temperature profiles are simulated in SimPulse® using devices modeled as a material stack: (from bottom up) 100 μm PEN, 100 nm Al (if bottom contact is present for simulation), and 20 nm ZrO₂. For ZrO₂ on top of the bottom Al contact, the volumetric, e.g. using Beer-Lambert law, absorption calculation method is used. For ZrO₂ directly on PEN, the total absorption was determined to be 16% through bolometry measurements of bare PEN substrates and PEN with ZrO₂ films, and the surface absorption calculation was used with this value.

5.4.4 Capacitor Fabrication and Measurements

Capacitors with areas of 4×10^{-4} and 8×10^{-4} cm², as defined by the top contact, are completed by deposition of 100 nm Al by thermal evaporation through a shadow mask. Capacitance-frequency was measured using an Agilent 4284A Precision LCR Meter from 10² Hz to 10⁶ Hz with 0V DC bias and 50 mV AC amplitude.

5.5 Results and Discussion

5.5.1 Photonic Curing and Patterning of ZrO₂ Films on PEN

Figure 5.1a shows the process for the deposition and photonic curing of ZrO₂ films on PEN substrates with patterned aluminum contacts. The precursor solution is spin-coated onto the substrate and then dried. The sample is then placed under the flash lamp and, through exposure to the high intensity light pulses, the precursor film is converted to an oxide film. This method produces a condensed oxide film wherever the precursor film is present on the substrate and is referred to as blanket photonic curing (b-PC, top row in Figure 5.1a). While oxide films on plastic substrates tend to crack during thermal annealing,²¹ the optical micrograph on the right shows crack-free blanket oxide films made by b-PC. This processing condition also applies to producing patterned oxide films when the precursor is first printed via an additive-deposition technique. We can also form patterned films in the photonic curing process. In shadow mask photonic curing (sm-PC, middle row in Figure 5.1a), a shadow mask is placed on top of a blanket precursor film prior to photonic curing and the unexposed regions of the precursor film are rinsed off in a developing solution after curing, leaving behind a patterned oxide film. In this photoresist-free patterning process, the precursor film acts as a self-patterning oxide precursor.^{31,51} Finally, in self-aligned photonic curing (sa-PC, bottom row in Figure 5.1a), a pattern is defined by the bottom Al contact layer. In the areas where the film is directly on top of the contact layer, the precursor is sufficiently converted to become insoluble in the developing solution. However, because sa-PC uses a less intense light pulse than b-PC or sm-PC, the precursor film directly on top of the PEN does not convert and is removed by the developing solution. In this scheme, we achieve mask-less self-aligned patterning of the oxide film

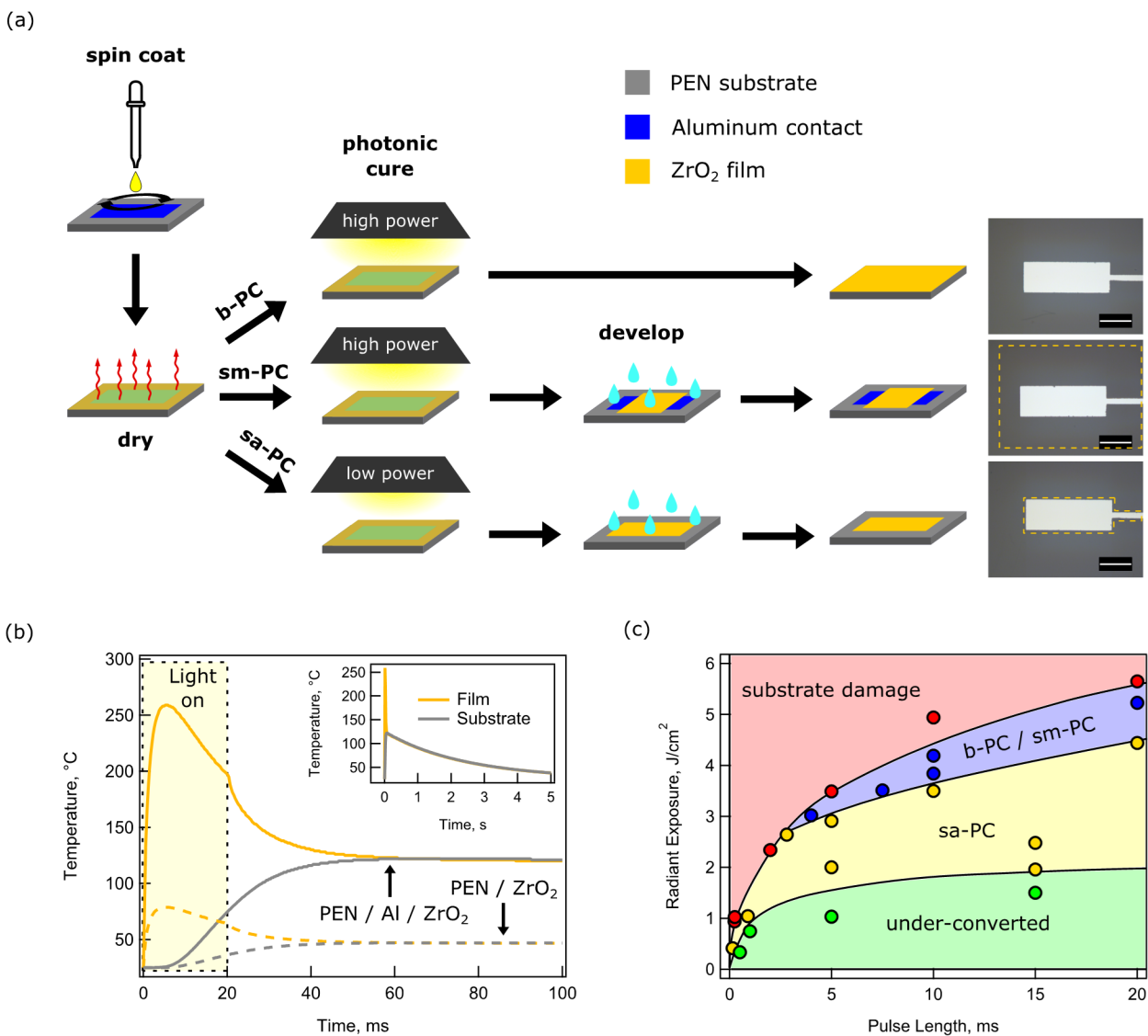


Figure 5.1: Photonic curing process with three patterning modes. (a) Schematic of three photonic curing processes for forming ZrO_2 on PEN: blanket photonic curing (b-PC, top), shadow mask photonic curing (sm-PC, middle), and self-aligned photonic curing (sa-PC, bottom). The rightmost column shows optical images of each PC ZrO_2 film on PEN with patterned Al bottom contacts. The borders of the patterned ZrO_2 films are marked with orange dashed lines. Scale bars represent $500 \mu\text{m}$. (b) Simulated film (orange) and substrate (grey) temperatures vs. time for a 20 ms light pulse on a ZrO_2 film deposited on top of Al contacts (PEN / Al / ZrO_2 , solid lines) and directly on PEN (PEN / ZrO_2 , dashed lines). Inset shows the temperature response of the sample on Al contacts over an extended (5 seconds) time frame. (c) Summary of photonic curing outcomes as a function of radiant exposure and pulse length. Conditions resulting in under-converted films (green), sa-PC (yellow), b-PC / sm-PC (blue), and substrate damage (red) are marked with circles for measured conditions and shaded regions are extrapolated.

film. Because conventional photolithography can be applied to pattern the bottom Al contacts, sa-PC can achieve smaller feature size than sm-PC. The rightmost column in Figure 5.1a shows optical images of each PC ZrO₂ film on a PEN substrate with a patterned Al bottom contact.

To understand the physical mechanism that enables the self-aligned patterning, simulated temperature profiles for ZrO₂ directly on PEN (PEN / ZrO₂) and for ZrO₂ on PEN with patterned bottom Al contacts (PEN / Al / ZrO₂) are shown in Figure 5.1b. For PEN / Al / ZrO₂ (solid lines), the temperature of the ZrO₂ film (yellow line) initially rises dramatically when the light is on (shaded in yellow) while the temperature of the PEN substrate (grey) remains low. The film and substrate reach thermal equilibrium with each other at around 60 ms, and with the surroundings at around 5 seconds (inset), after the onset of the light pulse. The shape of the temperature curve for the film during the light pulse is due to the diminishing power output of the lamp throughout the duration of the pulse, resulting in peak temperature occurring during the first half of the pulse. The large temperature difference between the low CTE film (260 °C) and high CTE polymer substrate (26 °C) during the light pulse when the peak film temperature is reached (5 ms) is critical for the formation of crack-free oxide films, as shown in the optical micrographs in Figure 5.1a. Additionally, the low peak temperature reached by the polymer substrate (122 °C) following the light pulse is important for avoiding damage to low-temperature substrate materials. For PEN / ZrO₂ (dashed lines), both the film and substrate temperatures remain much lower than for PEN / Al / ZrO₂. The difference in temperature is due to the lower light absorption of the transparent ZrO₂ precursor and PEN compared to that of Al. For the sa-PC process, this low maximum temperature reached in the precursor film on PEN is consistent with the lack of oxide conversion, which leads to the selective conversion (patterning) aligned to the

bottom Al contacts. However, in the b-PC and sm-PC processes, using light pulses with a higher average power, the ZrO₂ precursor film directly on PEN becomes resistant to the developing solution despite the simulated film temperature never exceeding 80 °C, much too low for oxide formation. This suggests additional non-thermal processes occurring in photonic curing, consistent with previous reports of photochemical reaction induced by UV radiation on metal nitrate precursors in thin films.^{24,26,31}

There are two independent variables that determine the intensity, or average power, of the light pulse – radiant exposure and pulse length. Radiant exposure is the total radiant energy delivered to the sample by a single light pulse per unit area (J/cm²) and pulse length is the duration of a single light pulse (ms). For a pulse of fixed length, an increase in radiant exposure results in an increase in power, whereas for a pulse of fixed radiant exposure, an increase in pulse length results in a decrease in power. Figure 5.1c summarizes the results of photonic curing of ZrO₂ films on PEN as a function of the pulse length and simulated radiant exposure. While we use simulated radiant exposure in this plot, Figure 5.2 shows a close agreement between simulated and measured values for photonic curing conditions used in this study. The pulse conditions which result in failure of the film or substrate are shown in red. Two failure modes can occur: (1) wrinkling of the film and top surface of substrate,⁵² and (2) cracking of the film. For a given radiant exposure, damage occurs if the pulse length is too short. This is due to the higher power delivered by the shorter pulse, resulting in higher temperatures at the top surface of the sample and thermal expansion of the top surface of the PEN. Longer pulses allow for heat transfer to the substrate during the light pulse, which limits the temperature reached at the sample surface such that damage does not occur. Similarly, for a constant pulse length, an increase in the

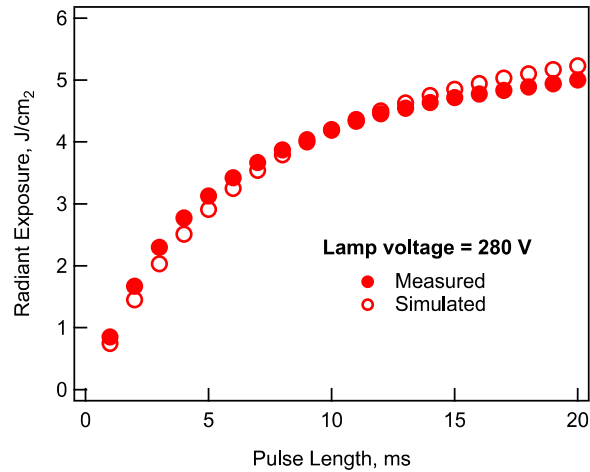


Figure 5.2: Energy output of photonic curing system. Simulated (SimPulse[®], open circles) and measured (using a calibrated bolometer, closed circles) radiant exposure vs. pulse length per pulse for a constant lamp driver voltage of 280 V.

radiant exposure eventually results in damage to the substrate due to increased power delivery and higher surface temperatures of the sample. Whether a pulse condition causes sample damage can be assessed after a single pulse. This is because the experimental repetition rate used was 0.2 Hz, a much longer time-scale (5 seconds) than the pulse length (< 20 ms); thus, the sample returns to thermal equilibrium with its surroundings between pulses (Figure 5.1b, inset), meaning that each repeated pulse is a thermally independent event. By increasing the pulse length or decreasing the radiant exposure to avoid damage and move out of the red region of Figure 5.1c, we move into the processing window for ZrO₂ shown in blue and yellow. In the blue region, the film is converted independent of whether it is on top of PEN or Al, making this region usable for both b-PC and sm-PC processes. With a longer pulse length or lower radiant exposure, only the ZrO₂ precursor on top of Al is converted, enabling sa-PC in the yellow region. Within the blue and yellow processing regions, repetition of pulses can increase the extent of conversion of the oxide film without inducing damage. Any further increase in pulse length or reduction in radiant

exposure puts the process into the green area and results in under-converted films that cannot withstand the developing solution.

5.5.2 Dielectric Properties of PC-ZrO₂ on PEN

Photonicallly cured ZrO₂ films on PEN were evaluated as metal-insulator-metal (MIM) capacitor dielectrics. Figure 5.3a shows the effect of the number of pulses on the areal capacitance vs. frequency behavior of the capacitors for films photonicallly cured using 20 ms pulses, 5.23 J/cm² radiant exposure per pulse, and a pulse rate of 0.2 Hz. Figure 5.3b shows a summary of the low frequency (10³ Hz, hashed bars) and high frequency (10⁶ Hz, solid bars) areal capacitance for the same devices. The precursor film shows a large frequency dispersion, with the capacitance at 10³ Hz twice that at 10⁶ Hz, due to the residual organic solvent and nitrates from the precursor solution. After a single pulse the dispersion is greatly reduced, and the areal capacitance decreases at both high and low frequency as the residual solvent and nitrates are removed and metal-oxygen bond formation begins. During the first 5 pulses the dispersion continues to decrease as metal-oxygen bonding continues and the initial metal-hydroxide bonds are converted to metal-oxygen-metal bonds. After 10 pulses the capacitance increases at all frequencies indicating the densification of the film, and the dispersion in the capacitance is gone indicating removal of metal-hydroxide moieties. After 20 pulses the film has densified with a dramatic increase in capacitance. Figure 5.4 shows that the same trend emerges when the number of pulses is fixed at 20 and the pulse length and energy are varied from 0.5 ms to 20 ms and 0.33 J/cm² to 5.23 J/cm², respectively – first the frequency dispersion is reduced followed by an increase in capacitance. In either case (varying number of pulses or varying pulse length), as the frequency dispersion in the capacitance decreases and areal capacitance increases,

the dissipation factor also decreases to a minimum of 0.01 at 10^5 Hz for 20 pulses with 20 ms pulse length (Figures 5.3c and 5.4c). All three processing procedures produce ZrO_2 films with similar magnitudes and frequency dependence in capacitance and dissipation factor (Figure 5.5).

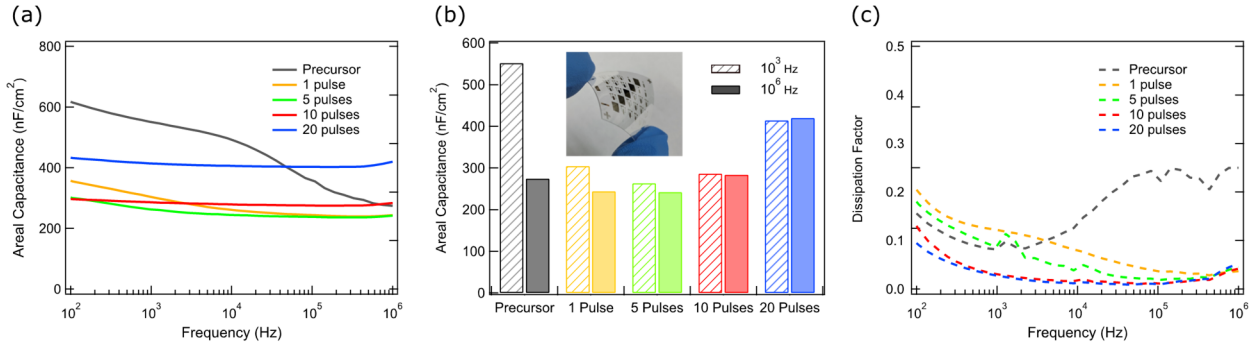


Figure 5.3: Dielectric properties of photonicallly cured ZrO_2 films as a function of the number of pulses. (a) Areal capacitance vs. frequency of MIM capacitors made from the dried ZrO_2 precursor and from photonicallly cured films (5.23 J/cm^2 per pulse, 20 ms pulse length, 0.2 Hz repetition rate) using 1 to 20 pulses. (b) Bar graph showing the low frequency (10^3 Hz, hashed bars) and high frequency (10^6 Hz, solid bars) areal capacitance for each condition in (a) with a photo of a completed device as the inset. (c) Dissipation factor vs. frequency for each of the capacitance measurements in (a).

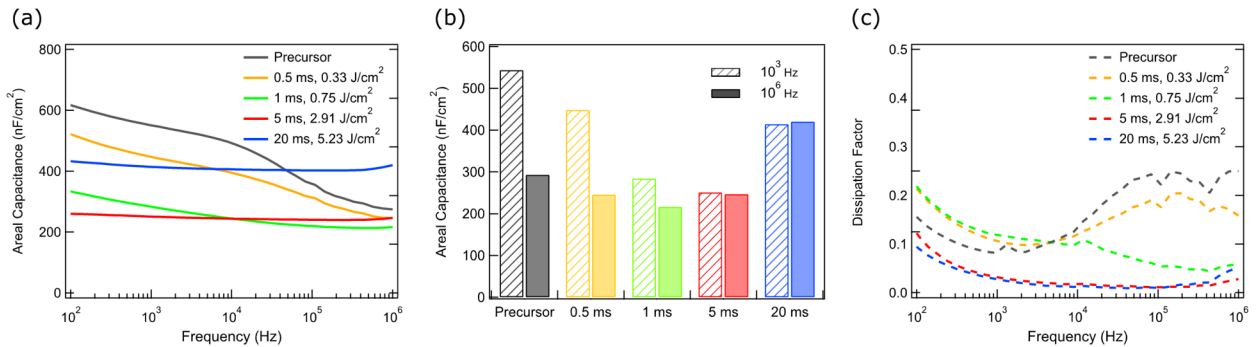


Figure 5.4: Dielectric properties of photonicallly cured ZrO_2 films as a function of pulse length. (a) Areal capacitance vs. frequency of MIM capacitors made from the dried ZrO_2 precursor and from photonicallly cured films with pulse length varied from 0.5 ms to 20 ms and radiant exposure from 0.33 J/cm^2 to 5.23 J/cm^2 (0.2 Hz repetition rate, 20 pulses). (b) Bar graph showing the low frequency (10^3 Hz, hashed bars) and high frequency (10^6 Hz, solid bars) areal capacitance for each condition in (a). (c) Dissipation factor vs. frequency for each of the capacitance measurements in (a).

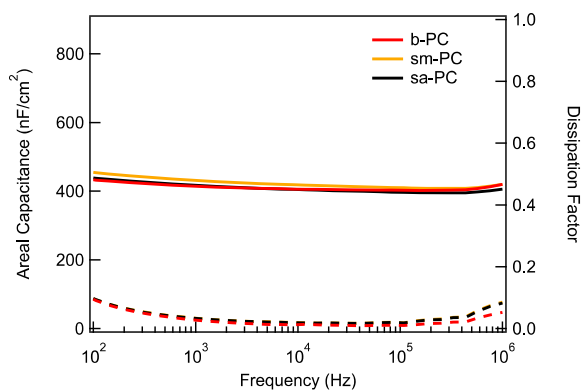


Figure 5.5: Areal capacitance and dissipation factor for the three different processing modes. Areal capacitance (left axis) and dissipation factor (right axis) for b-PC (red), sm-PC (orange), and sa-PC (black) ZrO₂ films on PEN.

Using 20 pulses of 20 ms pulse length (5.23 J/cm² per pulse), a single layer of sm-PC ZrO₂ made from a 0.15 M precursor solution concentration produces a smooth 19 nm thick film with good adhesion to the Al bottom contact (Figure 5.6a, left), high areal capacitance, and low dissipation factor (Figure 5.6b, blue). However, the leakage current density exceeds 10⁻⁷ A/cm² at an applied field of 1 MV/cm and dielectric breakdown occurs at less than 4 MV/cm (Figure 5.6c, blue). These results are comparable to other metal oxide dielectrics annealed at very low temperature (~150 °C) without UV assistance.⁵⁰ To improve the current density and breakdown field, a thicker dielectric is necessary. However, increasing the precursor film thickness by using a more concentrated precursor solution (0.4 M) results in wrinkling at the sample surface and adhesive failure³⁶ between the oxide and the Al contact (Figure 5.6a, middle). These phenomena may be explained by increased stress at the surface of the substrate caused by the thicker film during photonic curing due to the modest expansion of the PEN substrate. By performing the sm-PC process twice using 0.15 M precursor solution to form two thin layers, a thicker dielectric film with a wrinkle-free surface and good adhesion to the bottom contact can be formed (Figure 5.6a, right).

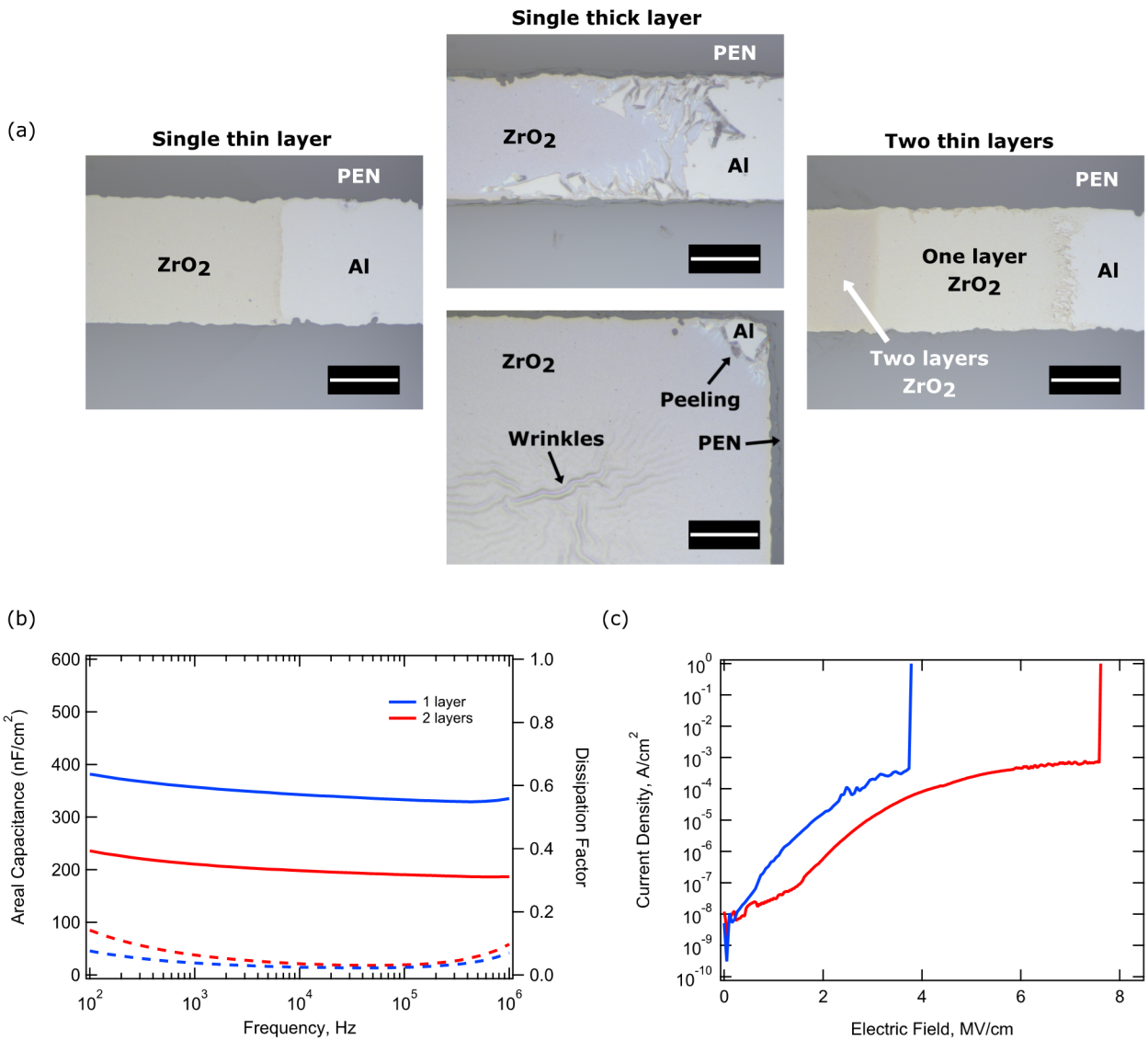


Figure 5.6: Different thickness of ZrO₂ dielectric films. (a) Optical images of a single thin layer of sm-PC ZrO₂ on a patterned bottom Al contact on PEN showing a smooth film and good adhesion to Al (left), a single thick sm-PC ZrO₂ layer showing poor adhesion between the oxide and substrate (middle), and two thin sm-PC ZrO₂ layers with good adhesion and a smooth surface (right). The two areas in the right image are due to misalignment of masks in the two-step process. Scale bars represent 50 μm. (b) Areal capacitance (left axis, solid lines) and dissipation factor (right axis, dashed lines) for a single-layer (blue) and two-layer (red) ZrO₂ capacitor. (c) Leakage current density vs. applied electric field for the single layer (blue) and two-layer (red) ZrO₂ capacitors.

The thicknesses of the two layers (19 nm for one coat and 35 nm for two coats) are measured by atomic force microscopy (Figure 5.7). Figure 5.6b (red curves) shows that the areal capacitance of the two-layer dielectric is ~ 200 nF/cm², corresponding to a dielectric constant of ~ 7.5 , and the dissipation factor is ~ 0.03 at 10^5 Hz. The leakage current density is below 10^{-6} A/cm² at 2 MV/cm and the breakdown field is nearly 8 MV/cm (Figure 5.6c, red). These values are comparable to many oxide dielectrics annealed for long times (20 to 90 minutes per layer) at high temperatures (~ 250 °C) or with UV radiation,⁴⁹ but are achieved here with only 100 seconds of processing time per layer.

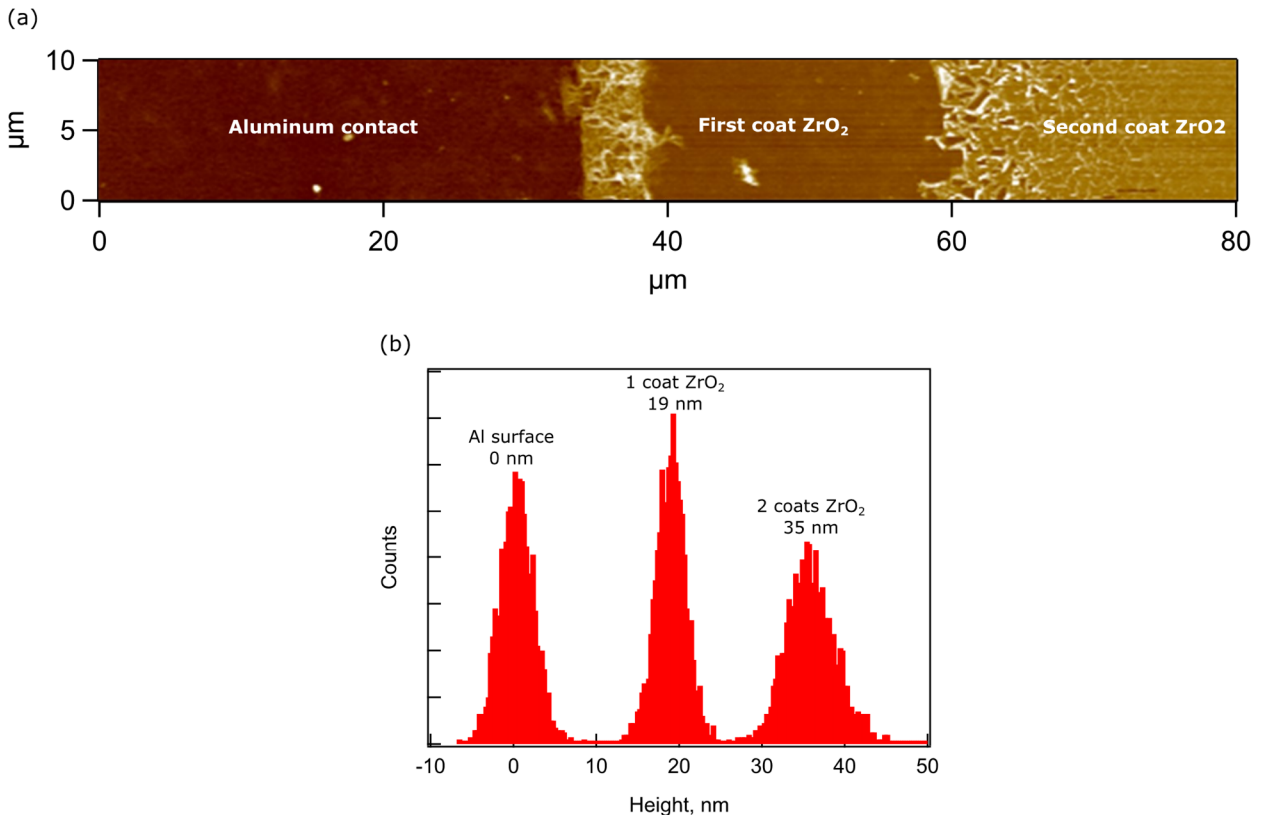


Figure 5.7: Atomic force microscopy (AFM) thickness determination of two-layer b-PC ZrO₂ film. (a) AFM image of Al contact (left), one ZrO₂ layer (middle), and two ZrO₂ layers (right) on PEN. (b) Histogram of heights in (a) with the lowest peak (Al contact) normalized to height = 0 nm, the second peak (one layer of ZrO₂) at 19 nm, and the third peak (two layers of ZrO₂) at 35 nm.

5.6 Conclusions

5.6.1 Path to High-Throughput Processing of Oxide Electronics

Typical oxide annealing times are incompatible with high-throughput processing. As an example, a 20-minute thermal annealing step at a web speed of 30 m/min requires a web path length of 600 m inside an oven. The system used for the results presented above (PulseForge® Invent with one lamp driver (500 V), a 3 A power supply, and a 20 mm diameter by 150 mm length lamp) can process samples using 20 ms pulses delivering 5.23 J/cm² at a maximum rate of 0.36 Hz. 20 pulses are found to achieve full conversion of ZrO₂ films. Combined with a uniform down-web processing length in an industrial configuration of 150 mm for a single lamp, these conditions translate to a maximum web speed of 0.16 m/min. Upscaling the photonic curing process to > 30 m/min requires three things: (1) a reduction of the number of pulses necessary for conversion, (2) an increase in the down-web processing length, and (3) an increase in the pulse rate. To reduce the number of pulses for oxide conversion, the maximum energy per pulse can be increased by adding additional energy storage capacity to the PulseForge® system. This is achieved by increasing the number of lamp drivers. Experiments were performed on an upgraded R&D system with 2 additional lamp drivers (3 drivers total). This configuration allows for a more sustained power output in a single pulse, enabling a pulse with lower peak intensity but longer duration that delivers more energy to the sample without increasing the maximum film temperature. Using this system, we achieved oxide conversion in a single 100 ms pulse with radiant exposure of 14.1 J/cm² (Figure 5.8). Using one pulse instead of 20 increases the web speed by 20-fold to 3.2 m/min. To increase the down-web processing length, a longer lamp can be used. SimPulse® simulations show that the same pulse output can be achieved using a

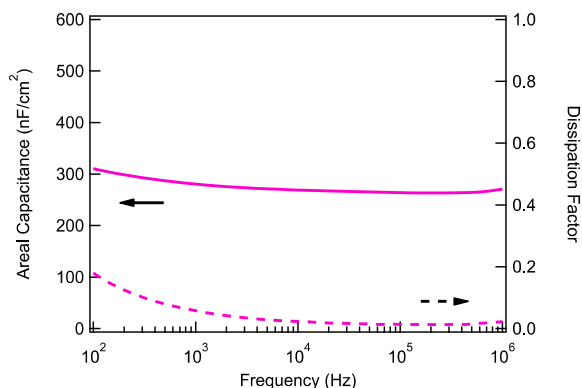


Figure 5.8: Areal capacitance and dissipation for ZrO₂ dielectric cured using a single photonic curing pulse on an upgraded tool. Areal capacitance (left axis) and dissipation factor (right axis) for ZrO₂ exposed to a single 100 ms photonic curing pulse.

300 mm long by 24 mm diameter lamp. By doubling the processing area, the web speed is doubled to 6.4 m/min. To increase the pulse rate, a higher current power supply can be used.

Industrial versions of the PulseForge tool used in this study currently exist with a power supply current of 45 A. The simulated maximum pulse rate based on the 45 A power supply and the above pulse condition is 2.9 Hz, meaning that 52 m/min of oxide conversion can be realized.

This demonstration of high-quality solution-deposited oxide films on a flexible plastic substrate opens up new prospects for high-throughput, low-cost manufacturing.

5.7 Acknowledgments

This work is funded in part by the U.S. Department of Energy Solar Energy Technologies Office, under Award Number DE-EE0008544. J.W.P.H. acknowledges support from the Texas Instruments Distinguished Chair in Nanoelectronics. The authors thank Teijin Film Solutions Limited and Inabata America Corporation for providing samples of Teonex[®] Q65HA PEN films.

5.8 References

- (1) Choi, M.; Kim, Y.; Ha, C. Polymers for Flexible Displays: From Material Selection to Device Applications. **2008**, *33*, 581–630.
- (2) Fthenakis, V. Sustainability of Photovoltaics: The Case for Thin-Film Solar Cells. *Renew Sustain Energy Rev* **2009**, *13* (9), 2746–2750.
- (3) Hwang, G.; Byun, M.; Jeong, C.; Lee, K. Flexible Piezoelectric Thin-Film Energy Harvesters and Nanosensors for Biomedical Applications. *Adv Healthc Mater* **2015**, *4* (5), 646–658.
- (4) Pang, C.; Lee, C.; Suh, K. Recent Advances in Flexible Sensors for Wearable and Implantable Devices. *J Appl Polym Sci* **2013**, *130* (3), 1429–1441.
- (5) Wong, W. S.; Chabinyo, M. L.; Ng, T.-N.; Salleo, A. Flexible Electronics, Materials and Applications. **2009**, 143–181.
- (6) Palavesam, N.; Marin, S.; Hemmetzberger, D.; Landesberger, C.; Bock, K.; Kutter, C. Roll-to-Roll Processing of Film Substrates for Hybrid Integrated Flexible Electronics. *Flexible Print Electron* **2018**, *3* (1), 014002.
- (7) Søndergaard, R. R.; Hösel, M.; Krebs, F. C. Roll-to-Roll Fabrication of Large Area Functional Organic Materials. *J Polym Sci Part B Polym Phys* **2013**, *51* (1), 16–34.
- (8) Li, Z.; Klein, T. R.; Kim, D.; Yang, M.; Berry, J. J.; van Hest, M. F.; Zhu, K. Scalable Fabrication of Perovskite Solar Cells. *Nat Rev Mater* **2018**, *3* (4), 18017.
- (9) Hwang, K.; Jung, Y.; Heo, Y.; Scholes, F. H.; Watkins, S. E.; Subbiah, J.; Jones, D. J.; Kim, D.; Vak, D. Toward Large Scale Roll-to-Roll Production of Fully Printed Perovskite Solar Cells. *Adv Mater* **2015**, *27* (7), 1241–1247.
- (10) Song, Z.; McElvany, C. L.; Phillips, A. B.; Celik, I.; Krantz, P. W.; Wathage, S. C.; Liyanage, G. K.; Apul, D.; Heben, M. J. A Technoeconomic Analysis of Perovskite Solar Module Manufacturing with Low-Cost Materials and Techniques. *Energ Environ Sci* **2017**, *10* (6), 1297–1305.
- (11) Abbel, R.; Galagan, Y.; Groen, P. Roll-to-Roll Fabrication of Solution Processed Electronics. *Adv Eng Mater* **2018**, *20* (8), 1701190.
- (12) Duta, M.; Anastasescu, M.; Calderon-Moreno, J.; Predoana, L.; Preda, S.; Nicolescu, M.; Stroescu, H.; Bratan, V.; Dascalu, I.; Aperathitis, E.; et al. Sol–Gel versus Sputtering Indium Tin Oxide Films as Transparent Conducting Oxide Materials. *J Mater Sci Mater Electron* **2016**, *27* (5), 4913–4922.

- (13) Kim, M.-G.; Kanatzidis, M. G.; Facchetti, A.; Marks, T. J. Low-Temperature Fabrication of High-Performance Metal Oxide Thin-Film Electronics via Combustion Processing. *Nat Mater* **2011**, *10* (5), 382.
- (14) Fu, Q.; Cao, C.-B.; Zhu, H.-S. Preparation of Alumina Films from a New Sol–Gel Route. *Thin Solid Films* **1999**, *348* (1–2), 99–102.
- (15) Bretos, I.; Jiménez, R.; Ricote, J.; Calzada, L. M. Low-Temperature Crystallization of Solution-Derived Metal Oxide Thin Films Assisted by Chemical Processes. *Chem Soc Rev* **2017**, *47* (2), 291–308.
- (16) Branquinho, R.; Salgueiro, D.; Santos, L.; Barquinha, P.; Pereira, L.; Martins, R.; Fortunato, E. Aqueous Combustion Synthesis of Aluminum Oxide Thin Films and Application as Gate Dielectric in GZTO Solution-Based TFTs. *Acs Appl Mater Inter* **2014**, *6* (22), 19592–19599.
- (17) Wang, B.; Leonardi, M. J.; Huang, W.; Chen, Y.; Zeng, L.; Eckstein, B. J.; Marks, T. J.; Facchetti, A. Marked Cofuel Tuning of Combustion Synthesis Pathways for Metal Oxide Semiconductor Films. *Adv Electron Mater* **2019**, 1900540.
- (18) Wang, B.; Zeng, L.; Huang, W.; Melkonyan, F. S.; Sheets, W. C.; Chi, L.; Bedzyk, M. J.; Marks, T. J.; Facchetti, A. Carbohydrate-Assisted Combustion Synthesis To Realize High-Performance Oxide Transistors. *J Am Chem Soc* **2016**, *138* (22), 7067–7074.
- (19) Wang, B.; Yu, X.; Guo, P.; Huang, W.; Zeng, L.; Zhou, N.; Chi, L.; Bedzyk, M. J.; Chang, R. P.; Marks, T. J.; et al. Solution-Processed All-Oxide Transparent High-Performance Transistors Fabricated by Spray-Combustion Synthesis. *Adv Electron Mater* **2016**, *2* (4), 1500427.
- (20) MacDonald, W. A. Engineered Films for Display Technologies. *J Mater Chem* **2003**, *14* (1), 4–10.
- (21) Daunis, T. B.; Gutierrez-Heredia, G.; Rodriguez-Lopez, O.; Wang, J.; Voit, W. E.; Hsu, J. W. Solution-Deposited Al₂O₃ Dielectric towards Fully-Patterned Thin Film Transistors on Shape Memory Polymer. **2017**, 101051Z-101051Z – 8.
- (22) MacDonald, W.; Looney, M.; MacKerron, D.; Eveson, R.; Adam, R.; Hashimoto, K.; Rakos, K. Latest Advances in Substrates for Flexible Electronics. *J Soc Inf Display* **2007**, *15* (12), 1075–1083.
- (23) Lin, Y.; Faber, H.; Zhao, K.; Wang, Q.; Amassian, A.; McLachlan, M.; Anthopoulos, T. D. High-Performance ZnO Transistors Processed Via an Aqueous Carbon-Free Metal Oxide Precursor Route at Temperatures Between 80–180 °C. *Adv Mater* **2013**, *25* (31), 4340–4346.

- (24) Rim, Y.; Lim, H.; Kim, H. Low-Temperature Metal-Oxide Thin-Film Transistors Formed by Directly Photopatternable and Combustible Solution Synthesis. *Acs Appl Mater Inter* **2013**, *5* (9), 3565–3571.
- (25) Park, Y.; Desai, A.; Salleo, A.; Jimison, L. Solution-Processable Zirconium Oxide Gate Dielectrics for Flexible Organic Field Effect Transistors Operated at Low Voltages. *Chem Mater* **2013**, *25* (13), 2571–2579.
- (26) Hwang, J.; Lee, K.; Jeong, Y.; Lee, Y.; Pearson, C.; Petty, M. C.; Kim, H. UV-Assisted Low Temperature Oxide Dielectric Films for TFT Applications. *Adv Mater Interfaces* **2014**, *1* (8), 1400206.
- (27) John, R.; Chien, N.; Shukla, S.; Tiwari, N.; Shi, C.; Ing, N.; Mathews, N. Low-Temperature Chemical Transformations for High-Performance Solution-Processed Oxide Transistors. *Chem Mater* **2016**, *28* (22).
- (28) Carlos, E.; Branquinho, R.; Kiazadeh, A.; Barquinha, P.; Martins, R.; Fortunato, E. UV Mediated Photochemical Treatment for Low Temperature Oxide Based TFTs. *Acs Appl Mater Inter* **2016**, *8* (45), 31100.
- (29) Leppäniemi, J.; Eiroma, K.; Majumdar, H.; Alastalo, A. Far-UV Annealed Inkjet-Printed In 2 O 3 Semiconductor Layers for Thin-Film Transistors on a Flexible Polyethylene Naphthalate Substrate. *Acs Appl Mater Inter* **2017**, *9* (10), 8774–8782.
- (30) Sanctis, S.; Hoffmann, R. C.; Bruns, M.; Schneider, J. J. Direct Photopatterning of Solution-Processed Amorphous Indium Zinc Oxide and Zinc Tin Oxide Semiconductors—A Chimie Douce Molecular Precursor Approach to Thin Film Electronic Oxides. *Adv Mater Interfaces* **2018**, *5* (15), 1800324.
- (31) Daunis, T. B.; Barrera, D.; Gutierrez-Heredia, G.; Rodriguez-Lopez, O.; Wang, J.; Voit, W. E.; Hsu, J. Solution-Processed Oxide Thin Film Transistors on Shape Memory Polymer Enabled by Photochemical Self-Patterning. *J Mater Res* **2018**, *33* (17), 2454–2462.
- (32) Kim, Y.-H.; Heo, J.-S.; Kim, T.-H.; Park, S.; Yoon, M.-H.; Kim, J.; Oh, M.; Yi, G.-R.; Noh, Y.-Y.; Park, S. Flexible Metal-Oxide Devices Made by Room-Temperature Photochemical Activation of Sol–Gel Films. *Nature* **2012**, *489* (7414), 128.
- (33) Park, S.; Kim, K.; Jo, J.; Sung, S.; Kim, K.; Lee, W.; Kim, J.; Kim, H.; Yi, G.; Kim, Y.; et al. In-Depth Studies on Rapid Photochemical Activation of Various Sol–Gel Metal Oxide Films for Flexible Transparent Electronics. *Adv Funct Mater* **2015**, *25* (19), 2807–2815.
- (34) Dellis, S.; Isakov, I.; Kalfagiannis, N.; Tetzner, K.; Anthopoulos, T. D.; Koutsogeorgis, D. C. Rapid Laser-Induced Photochemical Conversion of Sol–Gel Precursors to In 2 O 3 Layers and Their Application in Thin-Film Transistors. *J Mater Chem C* **2017**, *5* (15), 3673–3677.

- (35) Schroder, K.; Rawson, I. M.; Pope, D. S.; Farnsworth, S. Photonic Curing Explanation and Application to Printing Copper Traces on Low Temperature Substrates. *Int Symposium Microelectron* **2011**, *2011* (1), 001040–001046.
- (36) Schroder, K. A. Mechanisms of Photonic CuringTM: Processing High Temperature Films on Low Temperature Substrates. *Technical Proceedings of the 2011 NSTI Nanotechnology Conference and Expo, NSTI-Nanotech 2011* **2011**, *2*, 220–223.
- (37) Schroder, K.; McCool, S.; Furlan, W. Broadcast Photonic Curing of Metallic Nanoparticle Films. **2006**, *3*, 198–201.
- (38) Farnsworth, S.; Schroder, K.; Wenz, B.; Pope, D.; Rawson, I. The Photonic Curing Process for Printed Electronics with Applications to Printed RFID Tags and Thin Film Transistors. *International Conference on Digital Printing Technologies* **2012**, 440–443.
- (39) Tetzner, K.; Schroder, K. A.; Bock, K. Photonic Curing of Sol–Gel Derived HfO₂ Dielectrics for Organic Field-Effect Transistors. *Ceram Int* **2014**, *40* (10), 15753–15761.
- (40) Lee, W.; Lee, S.; Lim, J.; Cho, J. Printed In-Ga-Zn-O Drop-Based Thin-Film Transistors Sintered Using Intensely Pulsed White Light. *Rsc Adv* **2015**, *5* (96), 78655–78659.
- (41) Yoo, T.-H.; Kwon, S.-J.; Kim, H.-S.; Hong, J.-M.; Lim, J.; Song, Y.-W. Sub-Second Photo-Annealing of Solution-Processed Metal Oxide Thin-Film Transistors via Irradiation of Intensely Pulsed White Light. *Rsc Adv* **2014**, *4* (37), 19375–19379.
- (42) Park, S.; Kim, D.; Shin, H.; Lee, D.; Zhang, X.; Park, J.; Choi, J. Advanced Photo-Annealing of Indium Zinc Oxide Films for Thin-Film Transistors Using Pulse UV Light. *J Information Disp* **2016**, *17* (1), 1–7.
- (43) Tetzner, K.; Lin, Y.-H.; Regoutz, A.; Seitkhan, A.; Payne, D. J.; Anthopoulos, T. D. Sub-Second Photonic Processing of Solution-Deposited Single Layer and Heterojunction Metal Oxide Thin-Film Transistors Using a High-Power Xenon Flash Lamp. *J Mater Chem C* **2017**, *5* (45), 11724–11732.
- (44) Garlapati, S.; Marques, G.; Gebauer, J.; Dehm, S.; Bruns, M.; Winterer, M.; Tahoori, M.; Aghassi-Hagmann, J.; Hahn, H.; Dasgupta, S. High Performance Printed Oxide Field-Effect Transistors Processed Using Photonic Curing. *Nanotechnology* **2018**, *29* (23), 235205.
- (45) Jo, J.-W.; Kim, K.-T.; Park, H.-H.; Park, S.; Heo, J.; Kim, I.; Lee, M.-J. High-Speed and Low-Temperature Atmospheric Photo-Annealing of Large-Area Solution-Processed IGZO Thin-Film Transistors by Using Programmable Pulsed Operation of Xenon Flash Lamp. *J Korean Phys Soc* **2019**, *74* (11), 1052–1058.

- (46) Benwadih, M.; Coppard, R.; Bonrad, K.; Klyszcz, A.; Vuillaume, D. High Mobility Flexible Amorphous IGZO Thin-Film Transistors with a Low Thermal Budget Ultra-Violet Pulsed Light Process. *ACS Appl Mater Inter* **2016**, *8* (50), 34513–34519.
- (47) Twyman, N. M.; Tetzner, K.; Anthopoulos, T. D.; Payne, D. J.; Regoutz, A. Rapid Photonic Curing of Solution-Processed In₂O₃ Layers on Flexible Substrates. *Appl Surf Sci* **2019**, *479* (Appl. Surf. Sci. 349 2015), 974–979.
- (48) Das, S.; Gu, G.; Joshi, P. C.; Yang, B.; Aytug, T.; Rouleau, C. M.; Geohegan, D. B.; Xiao, K. Low Thermal Budget, Photonic-Cured Compact TiO₂ Layers for High-Efficiency Perovskite Solar Cells. *J Mater Chem A* **2016**, *4* (24), 9685–9690.
- (49) Das, S.; Yang, B.; Gu, G.; Joshi, P. C.; Ivanov, I. N.; Rouleau, C. M.; Aytug, T.; Geohegan, D. B.; Xiao, K. High-Performance Flexible Perovskite Solar Cells by Using a Combination of Ultrasonic Spray-Coating and Low Thermal Budget Photonic Curing. *ACS Photonics* **2015**, *2* (6), 680–686.
- (50) Liu, A.; Zhu, H.; Sun, H.; Xu, Y.; Noh, Y. Solution Processed Metal Oxide High- κ Dielectrics for Emerging Transistors and Circuits. *Adv Mater* **2018**, *30* (33), 1706364.
- (51) Rim, Y.; Chen, H.; Liu, Y.; Bae, S.-H.; Kim, H.; Yang, Y. Direct Light Pattern Integration of Low-Temperature Solution-Processed All-Oxide Flexible Electronics. *ACS Nano* **2014**, *8* (9), 9680–9686.
- (52) Bush, K. A.; Rolston, N.; Gold-Parker, A.; Manzoor, S.; Hausele, J.; Yu, Z. J.; Raiford, J. A.; Cheacharoen, R.; Holman, Z. C.; Toney, M. F.; et al. Controlling Thin-Film Stress and Wrinkling during Perovskite Film Formation. *ACS Energy Lett* **2018**, *3* (6), 1225–1232.

CHAPTER 6

CONCLUSIONS AND FUTURE WORK

6.1 Conclusions

This dissertation demonstrates the use of light for curing solution deposited metal oxide films on plastic substrates. We developed the use of UV-ozone curing through a shadow mask as a method to pattern precursor films on shape memory polymer substrates. Patterning the films prior to thermal annealing allows for the formation of crack-free solution-deposited oxide films on this unique substrate. Thin film transistors were fabricated using Al_2O_3 (dielectric) and In_2O_3 (semiconductor) films deposited by this method. This technique is a new alternative to the high-cost and time-consuming methods of vacuum-deposition and traditional photolithography. Next, we presented a detailed study of the origin of the large hysteresis and unexpectedly high apparent mobility of these transistors. We showed how water absorbed by the gate dielectric from the atmosphere is responsible for these behaviors and related both the choice of the dielectric material and processing method to their presence. We identified the mechanism by which this absorbed water causes the large hysteresis and high apparent mobility – polarization of water molecules in the dielectric and charge transfer from the gate contact to the dielectric during device operation. We demonstrated how these behaviors can be eliminated by capping the susceptible dielectric with a dielectric having better water barrier properties. Finally, we demonstrated photonic curing as a high-speed processing method capable of curing solution-deposited ZrO_2 films on plastic substrates in as little as 100 milliseconds. The capacitors fabricated by this method are the first devices to be demonstrated using photonic curing of solution-deposited oxide dielectrics on plastic substrates. The results of this dissertation lay the

groundwork for high-throughput and low-cost fabrication of oxide electronics by solution deposition in a roll-to-roll process.

6.2 Future Work: Photonic Curing of Conducting Oxide Films

The demonstration of photonicallly cured ZrO_2 capacitors in Chapter 5 shows that photonic curing is a viable method for high speed conversion of solution-deposited oxide dielectrics on plastic substrates. However, to fully realize the roll-to-roll processing of solution-deposited oxide electronics, oxide materials with a variety of electronic properties must be used. Preliminary studies of the photonic curing of solution-deposited indium-zinc-oxide (as a conducting oxide) and In_2O_3 (as a semiconducting oxide) on plastic substrates have not yet been able to achieve conducting or semiconducting films. Because the n-type carriers in oxide conductors and semiconductors originate from oxygen vacancies in the material, future work should focus on methods to induce these vacancies in solution-deposited films by photonic curing, while still forming the necessary metal – oxygen bonding for a dense and fully converted oxide film. These properties can be achieved by long, high temperature annealing (Chapters 3 and 4 for semiconductors), and preliminary work has also resulted in semiconducting In_2O_3 by photonic curing on a silicon substrate using very high average power delivery which significantly heats the substrate. Therefore, methods to increase the film temperature during photonic curing, without significantly increasing heating to the substrate, should be examined. Possibilities include the inclusion of highly absorptive material, such as dyes, in or on top of the oxide precursor. Ideally, these materials should be removed during the photonic curing process, by physical ablation or chemical decomposition. This makes carbon-based materials a likely candidate. Additionally, additives which can act as reducing agents upon heating, for which

carbon-based materials are also a likely candidate, may be included in the film itself. Chapter 2 discusses how large concentrations of acetylacetone in Al_2O_3 precursors degrade the quality of the films produced by UV-ozone curing plus thermal annealing. This may be due to increased porosity of the film due to escaping decomposition products during annealing. However, low concentrations of organic molecules in conducting or semiconducting precursors may be beneficial by creating a reducing environment under the high temperatures reached by the film during photonic curing.

BIOGRAPHICAL SKETCH

Trey Daunis was born in Duncan, Oklahoma and graduated from McKinney High School in McKinney, Texas. He earned his Bachelor of Science in Chemical Engineering from Texas Tech University in 2013. He then earned his Master of Science in Materials Science and Engineering from The University of Texas at Dallas in December 2015. In the summer of 2015, he joined the research group of Prof. Julia Hsu and began his PhD research activity. His research is focused on the solution processing of metal oxide thin film electronics with an emphasis on developing techniques that are compatible with high-throughput and low-cost processing on plastic substrates. During his PhD research, he has published seven papers in peer-reviewed journals (3 as first author) with an additional first-author manuscript in submission, and he has given three conference presentations (two as a speaker).

CURRICULUM VITAE

Education

University of Texas at Dallas	Richardson, Texas
Ph.D. Candidate Materials Science and Engineering	December 2019
M.S. Materials Science and Engineering	May 2015
Texas Tech University	Lubbock, Texas
B.S. Chemical Engineering	May 2013
Minors: Bioengineering, Chemistry	

Research Experience

Hsu Lab, UT Dallas	June 2015 – Current
Graduate Research Assistant	
Laboratory for Surface and Nanostructure Modification, UT Dallas	July 2013 – August 2013
Research Assistant	
Gill Laboratory, Texas Tech University	June 2012 – May 2013
Undergraduate Research Assistant	

Other Experience

Physics Department, UT Dallas	August 2015 – May 2016
Teaching Assistant	

Publications

Journal Articles

1. J. Wang, E. Motaharif, L.N.S. Murthy, M. Higgins, D. Barrera, T. B. Daunis, Y. Zheng, A.V. Malko, F. Ely, M. Quevedo-Lopez, M. Lee, J.W.P. Hsu, Revealing lattice and photocarrier dynamics of high-quality MAPbBr₃ single crystals by far infrared reflection and surface photovoltage spectroscopy. *J. Appl. Phys.* **2019**, *125* (2), 025706
2. T.B. Daunis, J.M.H. Tran, J.W.P. Hsu, Effects of Environmental Water Absorption by Solution-Deposited Al₂O₃ Gate Dielectrics on Thin Film Transistor Performance and Mobility. *ACS Appl. Mater. Interfaces* **2018**, *10* (46), 39435–39440
3. T.B. Daunis, D. Barrera, G. Gutierrez-Heredia, O. Rodriguez-Lopez, J. Wang, W.E. Voit, J.W.P. Hsu, Solution-Processed Oxide Thin Film Transistors on Shape Memory Polymer Enabled by Photochemical Self-patterning. *J. Mater. Res.* **2018**, *33* (17), 2454-2463
4. J. Wang, T.B. Daunis, L. Cheng, B. Zhang, J. Kim, J.W.P. Hsu, Combustion Synthesis of p-Type Transparent Conducting CuCrO_{2+x} and Cu:CrO_x Thin Films at 180° C. *ACS Appl. Mater. Interfaces* **2018**, *10* (4), 3732-3738

5. W.A. Dunlap-Shohl, T.B. Daunis, X. Wang, J. Wang, B. Zhang, D. Barrera, Y. Yan, J.W.P. Hsu, D.B. Mitzi, Room-Temperature Fabrication of a Delafossite CuCrO₂ Hole Transport Layer for Perovskite Solar Cells, *J. Mater. Chem. A*, **2018**, *6*, 469-477
6. D. Barrera, A. Jawaid, T.B. Daunis, L. Cheng, Q. Wang, Y.-J. Lee, M.J. Kim, J. Kim, R.A. Vaia, J.W.P. Hsu, Inverted OPVs with MoS₂ Hole Transport Layer Deposited by Spray Coating, *Materials Today Energy* **2017**, *5*, 107-111
7. T.B. Daunis, G. Gutierrez-Heredia, O. Rodriguez-Lopez, J. Wang, W. E. Voit, J. W. P. Hsu, Solution-deposited Al₂O₃ Dielectric Towards Fully-patterned Thin Film Transistors on Shape Memory Polymer, *Proc. SPIE* **2017**, *10105*, 101051Z
8. L. Xu, J. Wang, M. A. Villa, T. B. Daunis, Y.-J. Lee, A. V. Malko, J. W. P. Hsu, Quantitative Analyses of Competing Photocurrent Generation Mechanisms in Fullerene-Based Organic Photovoltaics, *J. Phys. Chem. C* **2016**, *120* (30), 16470-16477

Presentations and Posters

1. T.B. Daunis, J.M.H. Tran, J.W.P. Hsu, Rapid Processing of Metal Oxide Thin-Film Transistors Enabled by Photonic Curing, 2018 Fall Materials Research Society Meeting, November 2018, Boston, MA, oral presentation, **Speaker**
2. J.W.P. Hsu, J. Wang, E. Motaharifar, L.N.S. Murthy, M. Higgins, D. Barrera, T.B. Daunis, Y. Zheng, A. Malko, F. Ely, M. Quevedo-Lopez, M. Lee, Contactless Measurements of Lattice and Photogenerated Charged Carrier Dynamics in Organic-Inorganic Hybrid Perovskite Single Crystals, 2018 Fall Materials Research Society Meeting, November 2018, Boston, MA, oral presentation
3. W. Dunlap-Shohl, T.B. Daunis, X. Wang, J. Wang, B. Zhang, D. Barrera, Y. Yang, J.W.P. Hsu, D. Mitzi, Room-Temperature Deposition of a Delafossite CuCrO₂ Hole Transport Layer for Perovskite Solar Cells, 2018 Spring Materials Research Society Meeting, April 2018, Phoenix, AZ, oral presentation
4. T. B. Daunis, G. Gutierrez-Heredia, O. Rodriguez Lopez, J. Wang, W. Voit, J. W. P. Hsu, Low-Temperature Solution-Processed Oxide Thin-Film Transistors on Flexible Shape Memory Polymer Substrate, 2017 Fall Materials Research Society Meeting, November 2017, Boston, MA, oral presentation, **Speaker**
5. J. Wang, T.B. Daunis, L. Cheng, B. Zhang, J. Kim, J.W.P. Hsu, Combustion Synthesis of CuCrO₂ and Cu:CrOx Films at 180°C, 2017 Fall Materials Research Society Meeting, November 2017, Boston, MA, poster
6. L.N.S. Murthy, L. Xu, T.B. Daunis, J.W.P. Hsu, F.Y. Cao, Y.J. Cheng, Photogenerated Charge Transfer Between Conducting Polymer and Oxide, Joint Fall 2017 Meeting of the Texas Section of the APS, October 2017, Richardson, TX, oral presentation
7. T.B. Daunis, G. Gutierrez-Heredia, O. Rodriguez-Lopez, J. Wang, W.E. Voit, J.W.P. Hsu, Solution-Deposited Al₂O₃ Dielectric Towards Fully-Patterned Thin Film Transistors on Shape Memory Polymer, SPIE OPTO, February 2017, San Francisco, CA, poster, **Presenter**
8. D. Barrera, Q. Wang, Y.-J. Lee, A. Jawaid, L. Cheng, T.B. Daunis, J. Kim, R.A. Vaia, M. Kim, J.W.P. Hsu, Solution Processed TMDs and Their Integration into Organic Photovoltaics, 2016 Fall Materials Research Society Meeting, November 2016, Boston, MA, oral presentation